

ČESKÉ VYSOKÉ
UČENÍ TECHNICKÉ
V PRAZE

FAKULTA JADERNÁ
A FYZIKÁLNĚ
INŽENÝRSKÁ



DIPLOMOVÁ
PRÁCE

2024

FILIP
KOŇAŘÍK

ČESKÉ VYSOKÉ UČENÍ TECHNICKÉ V PRAZE

FAKULTA JADERNÁ A FYZIKÁLNĚ INŽENÝRSKÁ

Vývoj skriptu pro
kalibraci jednotlivých
optických modulů
v segmentovaném kalorimetru
experimentu SuperNEMO

Diplomová práce

Autor práce: Bc. Filip Koňářík

Vedoucí práce: Mgr. Miroslav Macko, Ph.D.

Konzultant: Ing. Dominika Mašlářová

Školní rok: 2023/2024

I. OSOBNÍ A STUDIJNÍ ÚDAJE

Příjmení: **Koňářk** Jméno: **Filip** Osobní číslo: **494695**
Fakulta/ústav: **Fakulta jaderná a fyzikálně inženýrská**
Zadávací katedra/ústav: **Katedra fyzikální elektroniky**
Studijní program: **Fyzikální elektronika**
Specializace: **Počítačová fyzika**

II. ÚDAJE K DIPLOMOVÉ PRÁCI

Název diplomové práce:

Vývoj skriptu pro kalibraci jednotlivých optických modulů v segmentovaném kalorimetru experimentu SuperNEMO

Název diplomové práce anglicky:

Development of a script for calibration of individual optical modules in the segmented calorimeter of the SuperNEMO experiment

Pokyny pro vypracování:

SuperNEMO demonstrátor je v pozdní fázi výstavby a v roce 2024 začne generovat fyzikální data (nyní jsou dostupné pouze data z fáze zprovoznování). Náboj naměřený jednotlivými segmenty (optickými moduly) kalorimetru poskytuje informaci o energii elektronu a signál z dráhového detektoru slouží k rekonstrukci trajektorie částice.

Kalibrace je klíčovou úlohou ve vývoji každého detektoru částic. Vaší úlohou bude dodat funkční skript pro kalibraci jednotlivých optických modulů detektoru SuperNEMO.

Pokyny pro zpracování:

- 1) Shrňte své dřívější zkušenosti získané ze simulací a z analýzy dat z fáze zprovoznování. Jaké závěry plynou z předchozího vývoje kalibračního algoritmu?
- 2) Tým z University of Bordeaux vyvinul korekce efektů uvnitř plastických scintilátorů, např. Birksův efekt [1, 2] (ve francouzštině). Seznamte se s koncepty a s kódem (dostupným pro členy kolaborace), který korekce implementuje.
- 3) Cestou k optickému modulu elektrony z bizmutových zdrojů procházejí skrze plyn v dráhovém detektoru, kde ztratí část své kinetické energie. V předchozí práci jste ukázal, že tyto ztráty je možné korigovat za pomoci fenomenologického modelu o pěti parametrech. Ukázal jste, že tento model funguje, ale počet parametrů není optimální. Tyto parametry navíc nemají jasnou fyzikální interpretaci. Navrhněte fyzikální model energetických ztrát založený na Bethe-Blochově rovnici. Odvoďte všechny potřebné rovnice, které popisují energetické ztráty jakožto funkci konečné energie elektronu (E_f) a dráhy, kterou elektron urazil v plynu (d). Pro odhad dráhy (d) úzce spolupracujte s kolegou T. Křížákem, který vyvíjí algoritmus pro rekonstrukci trajektorií v detektoru SuperNEMO [3].
- 4) Diskutujte, zda lze navrhovaný fyzikální model po použití vhodných aproximací analyticky (nebo alespoň poloanalyticky) aplikovat na problém fitování spekter. Diskutujte výhody a nevýhody tohoto přístupu. Bylo by možné navrhnout alternativní řešení založené na numerickém přístupu?
- 5) Dodejte funkční algoritmus pro kalibraci jednotlivých optických modulů detektoru SuperNEMO. Algoritmus by na vstupu měl přijímat nezpracovaná data z optických modulů. Měl by být schopný nafitovat jednotlivá spektra vyjádřená v jednotkách náboje a převést je na energetická spektra (t.j. kalibrační proces). Algoritmus by měl uvažovat jak korekce navržené týmem z University of Bordeaux, tak Vámi navržené korekce energetických ztrát. Výstupem skriptu by měly být kalibrační parametry pro každý optický modul.
- 6) Diskutujte výsledky a celkový výkon skriptu. Spočítejte energetické rozlišení jednotlivých optických modulů.
- 7) Prezentujte výsledky v rámci mezinárodní kolaborace SuperNEMO.

Seznam doporučené literatury:

1. A. Huber. Recherche de la nature du neutrino avec le détecteur SuperNEMO: simulations optiques pour l'optimisation du calorimètre et performances attendues pour le 82Se, Ph.D. thesis, Université de Bordeaux, 2017. (<https://www.theses.fr/2017BORD0682>).
2. A. Pin. Recherche de la nature du neutrino via la décroissance double bêta sans émission de neutrinos : Caractérisation et optimisation du calorimètre SuperNEMO et impact sur la recherche de la décroissance du 82Se: Développement du premier prototype LiquidO, Ph.D. thesis, Université de Bordeaux, 2020. (<https://www.theses.fr/2020BORD0277>).
3. T. Křížák. Development of an algorithm for linear particle track reconstruction in SuperNEMO detector, Bachelor thesis, CTU in Prague, 2023. (<https://dspace.cvut.cz/handle/10467/111453>).

Jméno a pracoviště vedoucí(ho) diplomové práce:

Mgr. Miroslav Macko, Ph.D. ÚTEF

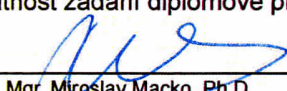
Jméno a pracoviště druhé(ho) vedoucí(ho) nebo konzultanta(ky) diplomové práce:

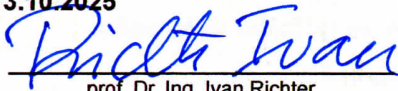
Ing. Dominika Mašlářová katedra fyzikální elektroniky FJFI

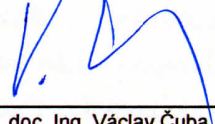
Datum zadání diplomové práce: **13.10.2023**

Termín odevzdání diplomové práce: **10.05.2024**

Platnost zadání diplomové práce: **13.10.2025**


Mgr. Miroslav Macko, Ph.D.
podpis vedoucí(ho) práce

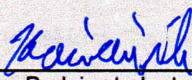

prof. Dr. Ing. Ivan Richter
podpis vedoucí(ho) ústavu/katedry


doc. Ing. Václav Čuba, Ph.D.
podpis děkana(ky)

III. PŘEVZETÍ ZADÁNÍ

Diplomant bere na vědomí, že je povinen vypracovat diplomovou práci samostatně, bez cizí pomoci, s výjimkou poskytnutých konzultací.
Seznam použité literatury, jiných pramenů a jmen konzultantů je třeba uvést v diplomové práci.

16.11.2023
Datum převzetí zadání

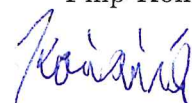

Podpis studenta

Prohlášení

Prohlašuji, že jsem předloženou práci vypracoval samostatně a že jsem uvedl veškerou použitou literaturu.

V Praze dne 10. 5. 2024

Filip Koňářík

Handwritten signature of Filip Koňářík in blue ink.

Poděkování

I would like to express my gratitude to the SuperNEMO Collaboration for accepting me as its member and allowing me to work on such an exciting project. I would especially like to thank Emmanuel Chauveau, Cheryl Patrick, Christine Marquet, Yves Lemièrre, Mathieu Bongrand, Laurent Simard and Xalbat Aguerre for their valuable input to my work.

Rád bych také poděkoval Dominice Mašlárové za její komentáře a pomoc při splnění všech náležitostí. Mé největší poděkování patří Miroslavu Mackovi, který mi předal nespočet cenných znalostí a dovedností, a jehož rady mě i v nejistých chvílích vedly ke správným výsledkům. Nakonec bych chtěl poděkovat svým rodičům za jejich bezmeznou důvěru a podporu, díky které tato práce mohla vzniknout.

Název práce:

Vývoj skriptu pro kalibraci jednotlivých optických modulů v segmentovaném kalorimetru experimentu SuperNEMO

Autor: Bc. Filip Koňářík

Studijní program: Fyzikální elektronika

Specializace: Počítačová fyzika

Druh práce: Diplomová práce

Vedoucí práce: Mgr. Miroslav Macko, Ph.D.

Konzultant: Ing. Dominika Mašlářová

Abstrakt: Práce se věnuje energetické kalibraci detektoru SuperNEMO. SuperNEMO je experiment zaměřený na hledání dvojného bezneutrinového beta rozpadu - hypotetického procesu, jehož objev by byl významný krok na poli neutrinové fyziky a částicové fyziky vůbec. K měření energií využívá SuperNEMO segmentovaný kalorimetr, který se skládá z tzv. optických modulů (OM). Kalibrace OM bude prováděná pomocí elektronů emitovaných systémem 42 kalibračních zdrojů obsahujících ^{207}Bi . Měřené energetické spektrum těchto elektronů je ovlivňováno řadou efektů. Práce navrhuje dvě skupiny korekcí těchto efektů: optické korekce a korekce energetických ztrát. Dále také popisuje kompletní algoritmus navržený k aplikaci energetických korekcí na kalibrační data a extrakci kalibračních parametrů jednotlivých OM. Algoritmus je nakonec použit k získání prvního spolehlivého odhadu energetických rozlišení OM. Ty se pohybují v rozsahu od 10 do 14% pro většinu modulů. Jako vedlejší produkt je extrahován tlak plynu uvnitř detektoru, jehož výsledkem je 0,82 bar, což se blíží skutečnému tlaku 0,88 bar, a lze to chápat jako ověření korekcí energetických ztrát.

Klíčová slova: dvojný beta rozpad, SuperNEMO, neutrino, energetická kalibrace

Thesis title:

Development of a script for calibration of individual optical modules in the segmented calorimeter of the SuperNEMO experiment

Author: Bc. Filip Koňářík

Study program: Physical Electronics

Specialization: Computational Physics

Thesis type: Master thesis

Supervisor: Mgr. Miroslav Macko, Ph.D.

Consultant: Ing. Dominika Mašlárová

Abstract: The thesis is dedicated to energy calibration of the SuperNEMO detector. SuperNEMO is an experiment focused on search for the neutrinoless double beta decay — a hypothetical process, the discovery of which would mean a huge step in the field of neutrino physics and particle physics as a whole. For energy measurement, SuperNEMO uses a segmented calorimeter composed of so-called optical modules (OMs). Calibration of the OMs will be performed using electrons emitted by a set of 42 ^{207}Bi calibration sources. The measured energy spectrum of these electrons is affected by several effects. The presented work proposes two groups of corrections for these effects: optical corrections and energy loss corrections. It also describes a complete algorithm designed to apply the energy corrections on the calibration data and extract calibration parameters of each individual OM. Finally, the algorithm is used to extract first reliable estimate of OM energy resolutions. These range between 10 and 14% for most modules. As a byproduct gas pressure inside the detector is extracted, resulting in 0.82 bar, close to the actual pressure of 0.88 bar which can be understood as a validation of the energy loss corrections.

Keywords: double beta decay, SuperNEMO, neutrino, energy calibration

Contents

Introduction	11
1 The history of neutrino physics and neutrinoless double beta decay	14
1.1 Discovery of the neutrino	14
1.2 Neutrino properties	15
1.2.1 Neutrino flavours	16
1.2.2 Neutrino oscillations	16
1.2.3 Neutrino mass	18
1.3 Double beta decay	19
1.3.1 Two-neutrino double beta decay ($2\nu\beta\beta$)	19
1.3.2 Neutrinoless double beta decay ($0\nu\beta\beta$)	21
1.3.2.1 Principle of detection	22
1.4 Experiments	22
1.4.1 Homogeneous detectors	23
1.4.1.1 Germanium detectors	23
1.4.1.2 Bolometers	24
1.4.1.3 Xenon time projection chambers	24
1.4.2 Tracko-calorimeters	24
2 The SuperNEMO Experiment	26
2.1 Source foil	26
2.2 Tracker	26
2.3 Calorimeter	28
2.3.1 Optical module geometry identifier	29
2.4 Background	30
2.4.1 Internal background	30
2.4.2 External background	30
2.5 Shielding	31
2.6 Energy calibration system	31
2.6.1 Principle of energy calibration	33
3 SuperNEMO data formats and calibration data processing	35
3.1 Simulated data	35
3.2 Real data	36
3.2.1 Tracker signal	36
3.2.2 Calorimeter signal	37
3.2.3 SuperNEMO data formats	41
3.2.3.1 Commissioning binary data (CBD)	41
3.2.3.2 Raw hit data (RHD) and Raw trigger data (RTD)	41

3.2.3.3	Raw event data (RED)	41
3.2.3.4	Unified digitized data (UDD)	41
3.2.3.5	Future formats	42
3.3	Calibration data	42
3.3.1	Event	42
3.3.2	Event selection	42
3.3.2.1	Track reconstruction	44
3.3.2.2	Cut conditions	44
3.3.3	Calibration spectra	48
3.3.3.1	Gain correction	49
3.3.3.2	Calibration parameter calculation	51
4	Energy corrections	53
4.1	Optical corrections	53
4.1.1	Birks' law and Cherenkov radiation	53
4.1.2	Geometrical non-uniformity	54
4.2	Energy loss corrections	55
4.2.1	Phenomenological model	56
4.2.2	Physics based model	57
4.2.2.1	Bethe-Bloch formula	58
4.2.2.2	Calculating energy losses of electrons	58
4.3	Application of energy corrections	60
4.3.1	Validation of the energy loss corrections using simulation	62
5	Development of the calibration algorithm	65
5.1	Calibration algorithm	66
5.1.1	Minimisation of the loss function	66
5.1.1.1	Properties of the loss function	67
5.1.1.2	Grid search	68
5.1.1.3	Downhill simplex method	68
5.1.2	Dependence of the calibration parameters on the tracking gas pressure	70
6	Estimation of SuperNEMO energy resolution	73
6.1	Simulation	74
6.2	Real data	74
	Conclusions	80
	Bibliography	82

Introduction

The Standard Model (the SM) of particle physics is currently the most successful theory of elementary particles and their interactions. It has managed to successfully predict the existence of many particles as well as unify the theory of Strong, Weak and Electromagnetic interactions. Despite that, it is already clear that the theory is only valid for a limited energy scale, as there are several known problems which it cannot explain. For example, gravity has not yet been included into the theory of fundamental interactions. Another problem is the existence of dark matter, which has been observed through its gravitational interaction with astronomical objects, but has not been described on a fundamental level. Finally, the Standard Model cannot describe the imbalance of amount of matter and antimatter in early stages of the universe. This so-called baryon asymmetry is in contradiction with conservation of lepton number assumed by the Standard Model. These unsolved phenomena and theories attempting to explain them are commonly referred to as physics beyond the Standard Model (BSM).

A possible field, in which an advancement beyond the scope of the Standard Model could be made, is the field of neutrino physics. Neutrino is an elementary particle very rarely interacting with matter. It exists in three masses and three flavours: electron, muon and tau neutrino. The key discovery, which revealed neutrinos as a possible clue to BSM, was the discovery of neutrino oscillations. It revealed that neutrinos change their flavour while travelling through space. The implication of this discovery is that neutrinos have non-zero mass. This is in contradiction with massless neutrinos often assumed in the Standard Model calculations. Absolute values of the three neutrino masses have yet not been determined, as neutrino oscillation experiments are only sensitive to their differences.

A possible way to measure neutrino masses is through measurement of $0\nu\beta\beta$ -decay half-life. The problem of such measurement is that the existence of $0\nu\beta\beta$ -decay is only hypothetical and has yet not been experimentally confirmed. So far, experiments have only been able to set a lower limit on its half-life, which is in the order of 10^{26} years (measured for example by GERDA for ^{76}Ge). For different isotopes, the limit can differ. This would make the $0\nu\beta\beta$ -decay the rarest phenomenon observed by humans. $0\nu\beta\beta$ -decay is characteristic by emission of two electrons. This simultaneous emission of two electrons can be experimentally observed. The key element of a $0\nu\beta\beta$ -decay experiment is differentiating $0\nu\beta\beta$ -decay from a more common $2\nu\beta\beta$ -decay, also emitting two electrons. This background created by the $2\nu\beta\beta$ -decay cannot be removed, but a distinction between the two decays can be done through energy spectra of the electrons. For the $2\nu\beta\beta$ -decay, the spectrum is continuous, while for the $0\nu\beta\beta$ -decay, the spectrum is only composed of a single energy.

One of the experiments attempting to observe the $0\nu\beta\beta$ -decay is the SuperNEMO experiment. SuperNEMO uses a unique tracko-calor design, allowing it to not only

measure energies of the electrons but also reconstruct their trajectories. This additional information allows for strong background suppression as well as measurement of different properties of the decay, such as angular distribution of the electrons. The SuperNEMO detector is composed of 3 main parts. In the middle there is a source foil containing 6.11 kg of ^{82}Se acting as a source of $0\nu\beta\beta$ -decay. The source foil is sandwiched between two sections of the tracker. Tracker is a wire chamber composed of 2034 cells operating in Geiger mode, which is used to detect particle trajectories. Finally, the detector is surrounded by the calorimeter used to measure electron energies. The calorimeter is composed of smaller optical modules (OMs). These are scintillation detectors composing of a block of plastic scintillator and a photomultiplier tube (PMT). For an experiment attempting to detect a phenomenon this rare, strong background suppression is very important. Because of that, the whole experiment is placed inside the LSM underground laboratory, which ensures reduction of cosmic rays. Significant attention has also been given to selection of radiopure materials for construction of the detector, as well as to construction of a system of shielding, which suppresses external background.

As the main goal of the experiment is energy measurement, a precise energy calibration of OMs needs to be done. For this purpose, a calibration system has been constructed. This calibration system uses 42 ^{207}Bi sources. These sources can be placed on precise positions in the middle of the detector. During a calibration measurement, the sources emit electrons with discrete energy spectrum. These pass through the tracker and are detected by OMs. Based on the spectrum measured by OMs, calibration parameters for each individual OM can be extracted. There are several effects which can influence the calibration. First, before reaching an OM, electrons have to pass through gas in the tracker as well as through a layer of Mylar and nylon. This results in energy losses which influence the measured spectrum. Thanks to the knowledge about electron trajectories, it is possible to calculate the amount of lost energy and correct this effect. Another factor which needs to be taken into account is a group of effects taking place during interaction of the electron with an OM. These effects add non-linearity to the OM response, as well as dependence of the response on the point in which energy of the electron was deposited. These effects can be corrected using so-called optical corrections. Finally, these corrections have to be implemented into a software which would be able to automatically process calibration data, apply the corrections and extract calibration parameters for each OM.

The first chapter provides a short introduction into the neutrino physics. It briefly covers the history which led to the discovery of neutrino oscillations and to the hunt for the $0\nu\beta\beta$ -decay. Then it summarizes different experimental approaches to $0\nu\beta\beta$ -decay detection and some results achieved by experiments in recent years.

The second chapter describes the SuperNEMO detector in more detail. It describes individual parts of the detector and the reasoning behind their design.

The third chapter of the thesis is where the practical part begins. It first describes different pieces of software and data formats to manipulate both simulated and real data. It also introduces a set of data cuts which was used on the calibration data throughout the whole work. At the end of the chapter, the structure of calibration data is described.

The fourth chapter is devoted to two groups of energy corrections: optical corrections and energy loss corrections. The primary attention is directed towards the latter group, as the development of a suitable energy loss model is one of the main

goals of this work. It first discusses flaws of an energy loss model proposed in previous work and then introduces an improved model based on the Bethe-Bloch formula.

The fifth chapter combines methods from chapters 3 and 4 into a single algorithm, which is able to apply cuts on the calibration data, apply energy correction and extract calibration parameters for each OM. It is explained that the calculation of calibration parameters leads to a problem of numerical minimization. This problem is then solved using the Downhill simplex method.

Finally, **The sixth chapter** uses the presented methods to calculate energy resolutions of OMs.

Chapter 1

The history of neutrino physics and neutrinoless double beta decay

1.1 Discovery of the neutrino

In the 1920s, the existence of protons and electrons has already been known. Atoms were considered to comprise these elementary particles in their bound states [1]. In the proton-electron model, beta decay is a process in which an electron is emitted, and the proton number is raised by one

$$(A, Z) \rightarrow (A, Z + 1) + e^-, \quad (1.1)$$

where (A, Z) is a nucleus with nucleon number A and proton number Z and e^- is an electron. Based on the energy conservation, the kinetic energy of the electron should be equal to the energy released in the decay

$$T_e = (M_{A,Z} - M_{A,Z+1} - m_e) c^2, \quad (1.2)$$

where $M_{A,Z}$ and $M_{A,Z+1}$ are masses of the nucleus before and after the decay respectively, m_e is the rest mass of the electron and c is the speed of light. The experiments have shown, however, that the energy spectrum of the electrons is continuous and that their energies are lower than T_e calculated by (1.2). This was surprising, as it seemingly contradicts the law of energy conservation.

The solution to this problem has been proposed in 1930 by Wolfgang Pauli [2]. He explained the continuous spectrum by assuming the existence of a new, neutral particle which was emitted in beta decay together with an electron. This particle carries away the missing energy and went undetected. He named the particle neutron, but later it was renamed to neutrino by Enrico Fermi.

Proving the existence of neutrino was not an easy task, as it very rarely interacts with matter. Despite that, the existence was proved in 1956 by the experiment of Clyde Cowan and Frederick Reines [3]. The experiment was based on inverse beta decay during which an antineutrino is absorbed by a proton, which results in the creation of a neutron and a positron

$$\bar{\nu}_e + p \rightarrow e^+ + n. \quad (1.3)$$

The positron then annihilates with a nearby electron creating two 511 keV gamma photons. A few hundred microseconds after that, the neutron is captured. This results

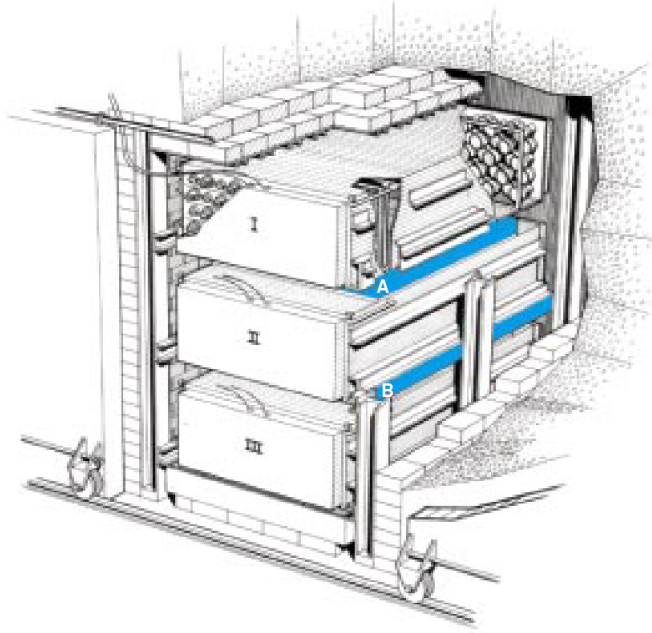


Figure 1.1: A scheme of the final Cowan-Reines experiment design. Two water tanks (blue) are surrounded by tanks containing liquid scintillator and 110 photomultiplier tubes. The image was adapted from Ref. [4].

in second emission. Based on time coincidence of these two signals, we detect inverse beta decay.

The Cowan-Reines experiment used 2 water tanks, in which the inverse beta decay took place. The water tanks were surrounded by large tanks with liquid scintillator. This setup was surrounded by photomultipliers which detected emitted gamma photons. A scheme of the detector can be seen in the figure 1.1. The whole detector was placed near a nuclear reactor serving as a strong source of neutrinos. The experiment was able to detect (2.88 ± 0.22) neutrinos per hour, confirming its existence.

1.2 Neutrino properties

A neutrino is an elementary particle well-known for its very rare interaction with matter. It is a lepton with zero charge which mostly interacts via Weak interaction. Due to this, it is very hard to detect. Currently, we distinguish three flavours of neutrinos — electron (e), muon (μ) and tau (τ) neutrino, as well as three masses m_1 , m_2 and m_3 . Neutrinos are produced by a number of different sources. These can be divided into artificial and natural. The most significant artificial source is nuclear reactors. These can provide high flux of neutrinos, which is often utilized by neutrino experiments. Examples of natural sources are geological radionuclides, interactions of cosmic rays with atmosphere, nuclear reactions in stars or explosions of supernovae. Neutrinos originating from these cosmic sources come to importance in astronomy as they travel through space almost unaffected. This allows astronomers to use them as an additional source of information about cosmic events.

1.2.1 Neutrino flavours

Even before the experimental discovery of neutrino in 1956, it was hypothesised that the muon neutrino could exist. Its existence was finally proved in an experiment conducted by Leon M. Lederman, Melvin Schwartz and Jack Steinberger at the Brookhaven National Laboratory in 1962 [5]. The experiment used accelerated pions, which decay into a muon and a neutrino

$$\pi^\pm \rightarrow \mu^\pm + (\nu/\bar{\nu}). \quad (1.4)$$

The muons were stopped by a 13.5 m thick wall while the neutrinos passed through the wall and continued to a detector where they were observed. In the detector, following reactions were expected to take place

$$\nu + n \rightarrow p + e^-, \quad (1.5)$$

$$\bar{\nu} + p \rightarrow n + e^+, \quad (1.6)$$

$$\nu + n \rightarrow p + \mu^-, \quad (1.7)$$

$$\bar{\nu} + p \rightarrow n + \mu^+. \quad (1.8)$$

If there was only one type (flavour) of neutrino, the reactions resulting in emission of electrons and muons should be equally abundant. However, the number of muons observed was significantly higher than electrons. This meant that the resulting charged lepton “remembered” which charged particle caused the creation of original neutrino impacting the detector (muon). This led to the conclusion, that there is a second flavour of neutrino — the μ -neutrino.

After the discovery of τ -lepton in 1975 a third neutrino flavour was hypothesised [6]. It was observed in 2000 by the DONUT experiment from Fermilab [7].

1.2.2 Neutrino oscillations

The Sun produces energy through fusion of light nuclei. Most of the energy is produced in the so-called proton-proton cycle, in which protons are fused into helium nuclei. Electron neutrinos are also emitted in these nuclear reactions. Part of the solar neutrino flux passes through Earth. In the 1960s, Raymond Davis and John Bahcall measured the flux of solar neutrinos in an experiment known as the Homestake experiment. They used 400 000 litres of C_2Cl_4 to capture neutrinos through the following reaction

$$\nu_e + {}^{37}Cl \rightarrow {}^{37}Ar + e^-. \quad (1.9)$$

Through subsequent measurement of argon abundance, it was possible to calculate the neutrino flux. The expected theoretical flux was 9.3 ± 1.3 SNU while the flux measured by the Homestake experiment was only 2.56 ± 0.32 SNU (One solar neutrino unit = one interaction per 10^{36} target atoms per second) [8]. At first, it was assumed that there is an error in solar models, but even their modification could not explain the discrepancy.

In 1958, Bruno Pontecorvo proposed a solution for the problem [9]. He hypothesised that neutrinos can spontaneously change their flavour as they travel through space. This phenomenon is called neutrino oscillations. Thanks to neutrino oscillations, part of the solar electron neutrinos could change their flavour along the way to earth. Neutrinos

of different flavours than electron would not be detected by experiments conducted at that time, as they were only sensitive to electron neutrinos.

Neutrino flavours and masses have their corresponding eigenstates. Let us denote $|\nu_1\rangle$, $|\nu_2\rangle$ and $|\nu_3\rangle$ the mass eigenstates and $|\nu_e\rangle$, $|\nu_\mu\rangle$ and $|\nu_\tau\rangle$ the flavour eigenstates. Thanks to the superposition principle, the relationships between the eigenstates can be written as

$$|\nu_\alpha\rangle = \sum_j U_{\alpha j}^* |\nu_j\rangle, \quad (1.10)$$

$$|\nu_j\rangle = \sum_\alpha U_{\alpha j} |\nu_\alpha\rangle, \quad (1.11)$$

where $|\nu_\alpha\rangle$ are the flavour eigenstates, $|\nu_j\rangle$ are the mass eigenstates and $U_{\alpha j}$ are elements of the so-called Pontecorvo – Maki – Nakagawa – Sakata (PMNS) matrix. Using the matrix notation, we can also rewrite the relationships as

$$\begin{pmatrix} |\nu_e\rangle \\ |\nu_\mu\rangle \\ |\nu_\tau\rangle \end{pmatrix} = \begin{pmatrix} U_{e1} & U_{e2} & U_{e3} \\ U_{\mu1} & U_{\mu2} & U_{\mu3} \\ U_{\tau1} & U_{\tau2} & U_{\tau3} \end{pmatrix} \begin{pmatrix} |\nu_1\rangle \\ |\nu_2\rangle \\ |\nu_3\rangle \end{pmatrix}. \quad (1.12)$$

The matrix is unitary to conserve norm of the wave functions. The propagation of mass eigenstates can be described by plane wave solutions as

$$|\nu_j(t)\rangle = e^{-i(E_j t - \vec{p}_j \vec{x})} |\nu_j(0)\rangle, \quad (1.13)$$

where E_j is the energy of the j -th mass eigenstate, t is the time from the start of the propagation, \vec{x} is the position of the particle and \vec{p}_j is its momentum. Quantities are expressed in natural units ($c = 1, \hbar = 1$). For $|\vec{p}_j| = p_j \gg m_j$, we can write

$$E_j = \sqrt{p_j^2 + m_j^2} \simeq p_j + \frac{m_j^2}{2p_j} \approx E + \frac{m_j^2}{2E}, \quad (1.14)$$

where E is the energy of the particle to be detected. This approximation holds thanks to ultrarelativistic nature of neutrinos. Thanks to high velocities of neutrinos, we have $t \approx L$. Combining (1.13) and (1.14), we get

$$|\nu_j(t)\rangle = e^{-i\frac{m_j^2 L}{2E}} |\nu_j(0)\rangle. \quad (1.15)$$

The probability that a neutrino originally of flavour α will later be observed as having flavour β is

$$P_{\alpha \rightarrow \beta} = |\langle \nu_\beta | \nu_\alpha(L) \rangle|^2. \quad (1.16)$$

Substituting from equations (1.10) and (1.15) into (1.16) we get

$$P_{\alpha \rightarrow \beta} = \left| \sum_j U_{\alpha j}^* U_{\beta j} e^{-i\frac{m_j^2 L}{2E}} \right|^2. \quad (1.17)$$

The PMNS matrix is unitary, and it can, thus, be seen as a rotation in 3D space. We can factorize the matrix into a product of three matrices, each representing a rotation around one coordinate axis

$$U = \begin{pmatrix} U_{e1} & U_{e2} & U_{e3} \\ U_{\mu1} & U_{\mu2} & U_{\mu3} \\ U_{\tau1} & U_{\tau2} & U_{\tau3} \end{pmatrix} = \begin{pmatrix} 1 & 0 & 0 \\ 0 & c_{23} & s_{23} \\ 0 & -s_{23} & c_{23} \end{pmatrix} \begin{pmatrix} c_{13} & 0 & s_{13}e^{-i\delta} \\ 0 & 1 & 0 \\ -s_{13}e^{i\delta} & 0 & c_{13} \end{pmatrix} \\ \begin{pmatrix} c_{12} & s_{12} & 0 \\ -s_{12} & c_{12} & 0 \\ 0 & 0 & 1 \end{pmatrix} \begin{pmatrix} e^{i\alpha_1/2} & 0 & 0 \\ 0 & e^{i\alpha_2/2} & 0 \\ 0 & 0 & 1 \end{pmatrix},$$

where $c_{ij} = \cos\theta_{ij}$, $s_{ij} = \sin\theta_{ij}$ introducing so-called mixing angles θ_{ij} . Then it is sufficient to calculate (1.17) only for these simpler matrices. This allows us to restrict ourselves to a case with only two neutrino flavours

$$\begin{pmatrix} |\nu_\alpha\rangle \\ |\nu_\beta\rangle \end{pmatrix} = \begin{pmatrix} \cos(\theta) & \sin(\theta) \\ -\sin(\theta) & \cos(\theta) \end{pmatrix} \begin{pmatrix} |\nu_1\rangle \\ |\nu_2\rangle \end{pmatrix}, \quad (1.18)$$

Now we can substitute the matrix elements into (1.17) to get

$$P(\nu_\alpha \rightarrow \nu_\beta) = \sin^2(2\theta) \sin^2\left(\frac{\Delta m_{ij}^2 L}{4E}\right), \quad (1.19)$$

where E is the neutrino's energy, L is the distance it has travelled and $\Delta m_{ij}^2 = m_i^2 - m_j^2$ is the difference of squared eigenmasses of i -th and j -th state. For the probability to be non-zero, at least one of the Δm_{ij}^2 values have to be non-zero. This condition is met only if at least one of the neutrino masses is non-zero. The existence of neutrino oscillations thus implies non-zero neutrino mass.

The first experiment to observe neutrino oscillations was SuperKamiokande in 1998 [10]. It measured the flux of atmospheric muon neutrinos. It received neutrinos emitted in the atmosphere above the detector as well as neutrinos, which were emitted on the other side of Earth and had to pass through the Earth to reach the detector. The amount of muon neutrinos arriving from the other side of Earth was lower than the amount arriving to the detector from above. This difference was the result of muon neutrinos oscillating into different flavour while passing through Earth. The existence of neutrino oscillation was also confirmed three years later by Sudbury Neutrino Observatory (SNO) [11]. The experiment was focused on solar neutrinos, but contrary to the preceding experiments, SNO was able to detect all three neutrino flavours. This experiment has shown that the solar models were correct and the discrepancy in solar neutrino flux was caused by neutrino oscillations.

1.2.3 Neutrino mass

Even though, we know that the neutrino mass is not zero, its absolute value is yet to be measured. Currently, we are only able to measure differences Δm_{ij}^2 through neutrino oscillation physics. More specifically, experiments measure the so-called solar mass splitting ($\Delta m_{21}^2 \simeq 7.6 \times 10^{-5} \text{ eV}^2$) and the atmospheric mass splitting ($|\Delta m_{31}^2| \simeq 2.5 \times 10^{-3} \text{ eV}^2$) [12]. From matter effects in the Sun, it is known that $\Delta m_{21}^2 > 0$. Δm_{31}^2 is measured via neutrino oscillations in vacuum, which only depend on its absolute value. Because of that, the sign of Δm_{31}^2 is unknown.

This ambiguity in the sign of Δm_{31}^2 leaves us with two possible orderings of neutrino masses. These orderings can be seen in the figure 1.2. As electron is the lightest particle

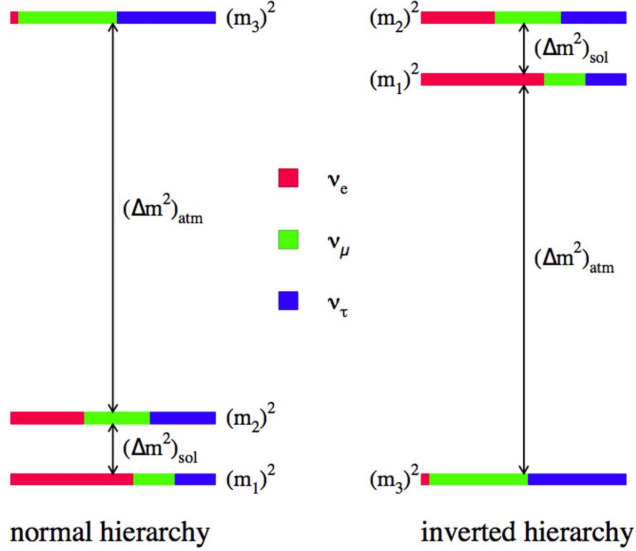


Figure 1.2: Two possible orderings of neutrino masses are currently considered — normal ordering and inverted ordering. In the picture, we can see their comparison. Coloured bars represent mass eigenstates as superpositions of flavour eigenstates. $(\Delta m^2)_{sol}$ is the solar mass splitting and $(\Delta m^2)_{atm}$ is the atmospheric mass splitting. The figure was adapted from Ref. [13].

out of electron, muon, tauon triplet, it is intuitively expected that the mass eigenstate with the highest abundance of electron flavour would be the lightest one. This is called “normal ordering”. The second option is so-called “inverted ordering” where the eigenstate with the lowest electron flavour abundance is the lightest one.

There are three main approaches of neutrino mass measurement. The first one is based on single beta decay. It is sensitive to the effective neutrino mass

$$m_\beta = \sqrt{\sum_{i=1}^3 U_{ei}^2 m_i^2}. \quad (1.20)$$

The effective mass is determined from precise measurement of the end of the beta spectrum. The current limit has been set by the KARTIN experiment: $m_\beta < 0.8$ eV [14]. The second approach is based on cosmological models. Neutrinos play an important role in formation of cosmological structures. Thanks to that, it is possible to estimate the sum of mass eigenvalues $\sum m_i$ based on astronomical observations. Its current limit is at $\sum m_i < 0.12$ eV and has been set by the Planck collaboration [15]. The last approach of mass measurement is based on neutrinoless double beta decay and will be described in the following section.

1.3 Double beta decay

1.3.1 Two-neutrino double beta decay ($2\nu\beta\beta$)

Two-neutrino double beta decay is a type of radioactive decay predicted by Maria Goeppert-Mayer in 1935. In $2\nu\beta\beta$ two neutrons in the atomic nucleus are transformed

into two protons followed by emission of two electrons and two antineutrinos [16]:

$$(A, Z) \rightarrow (A, Z + 2) + 2e^- + 2\bar{\nu}_e. \quad (1.21)$$

For the decay to occur, its Q -value (defined as a difference between nucleus mass after and before the decay) has to be positive. The mass of the nucleus can be written as

$$m(Z, N) = Zm_p + Nm_n - \frac{E_B(Z, N)}{c^2}, \quad (1.22)$$

where $m(Z, N)$ is the mass of the nucleus with Z protons and N neutrons, m_p and m_n are rest masses of proton and neutron and $E_B(Z, N)$ is binding energy of the nucleus. The sum $Zm_p + Nm_n$ represents the total rest mass of unbound nucleons. In the nucleus, additional energy $E_B(Z, N)$ is required to keep it bound. According to the formula $E = mc^2$, this energy decreases the nucleus mass. We can express the binding energy using semi-empirical Weizsäcker equation

$$E_B = a_V A - a_S A^{2/3} - a_C \frac{Z(Z-1)}{A^{1/3}} - a_A \frac{(N-Z)^2}{A} + \delta(N, Z), \quad (1.23)$$

where A is the mass number and a_V , a_S , a_C , a_A and $\delta(N, Z)$ are measured constants belonging to so-called volume term, surface term, Coulomb term, asymmetry term and pairing term, respectively.

- The volume term $a_V A$ is based on the strong nuclear force. The strong nuclear force has very short range, so the nucleons interact mostly only with their neighbours. The number of interacting nucleon pairs grows approximately with A . The volume of the nucleus also grows with A , which explains the name of the term.
- The surface term $a_S A^{2/3}$ is a correction of the volume term. It accounts for the nucleons on the surface of the nucleus, which have fewer neighbours than nucleons deep within the nucleus.
- The Coulomb term $a_C Z(Z-1)/A^{1/3}$ comes from the electrostatic repulsion between the protons. If we approximate the nucleus as a uniformly charged sphere, it can be shown that the electrostatic potential energy is proportional to $Z(Z-1)/A^{1/3}$.
- The asymmetry term $a_A (N-Z)^2/A$ comes from the Pauli exclusion principle. The principle states that no two identical fermions can occupy exactly the same quantum state in an atom. We can imagine that protons and neutrons have two respective sets of quantum states which they occupy. The more nucleons of one type in the nucleus, the higher energy levels they occupy. Because of this, the total energy of states occupied by protons and neutrons is lower for the nuclei with balanced number of protons and neutrons than for the unbalanced ones.
- The pairing term $\delta(N, Z)$ comes from the spin coupling of the nucleons.

The pairing term can take on three different values

$$\delta(N, Z) = \begin{cases} \frac{a_p}{\sqrt{A}} & Z, N \text{ even } (A \text{ even}), \\ 0 & A \text{ odd}, \\ -\frac{a_p}{\sqrt{A}} & Z, N \text{ odd } (A \text{ even}). \end{cases} \quad (1.24)$$

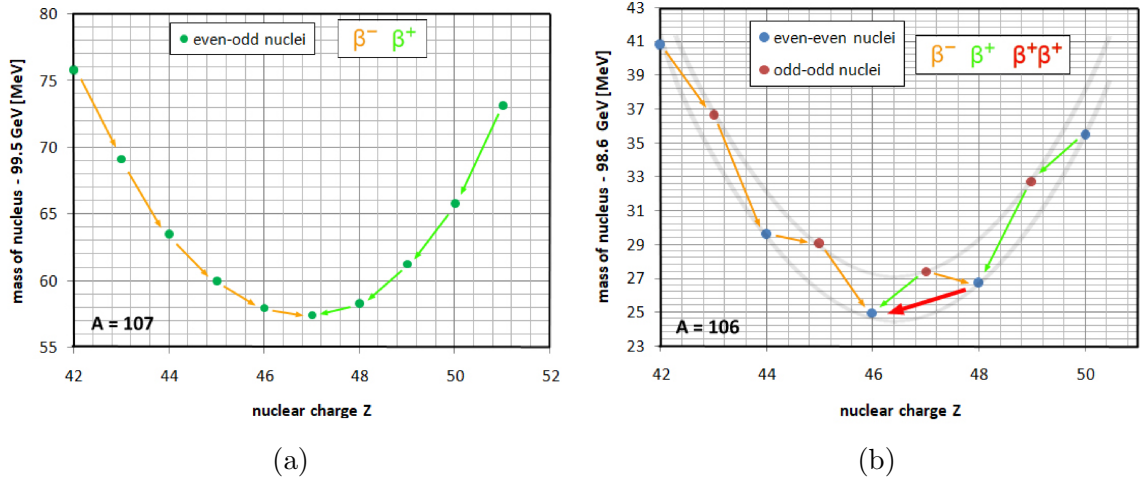


Figure 1.3: a) Dependency of mass of nuclei with a mass number $A = 107$ on proton number Z . Green points represent individual isotopes, green and yellow arrows represent decays β^- and β^+ . b) Same graph but for nuclei with $A = 106$. This time, isotopes find themselves on two parabolas. Red arrow represents double beta decay. The figure was adapted from Ref. [17].

Let us consider a nucleus with odd number of nucleons (e.g. $A = 107$). In this case $\delta(N, Z)$ will be equal to zero and the equation (1.23) then gives a quadratic relationship between the binding energy and the proton number. This can be seen in the figure 1.3a. We can see that A stays the same for all isotopes, as beta decay only changes Z . The nucleus tends to undergo beta decay to reach the most stable isotope, which is $Z = 47$ in this case. A more interesting situation arises when considering a nucleus with even number of nucleons (e.g. $A = 106$). In this case, $\delta(N, Z)$ can either be a_p/\sqrt{A} or $-a_p/\sqrt{A}$. Thanks to that, we get two parabolas, which can be seen in the figure 1.3b. The nucleus is decaying towards the most stable isotope. A spontaneous single beta decay transition to nucleus with $Z = 47$ is not possible because $Z = 47$ has a higher binding energy. The only way to reach a more stable isotope is then directly to $Z = 47$ through double beta decay (red arrow in the figure 1.3b). Such isotopes where standard beta decay is forbidden are ideal to observe double beta decay, since standard beta decay would otherwise produce very strong background.

1.3.2 Neutrinoless double beta decay ($0\nu\beta\beta$)

Neutrinoless double beta decay is a mode of double beta decay without the emission of neutrinos:

$$(A, Z) \rightarrow (A, Z + 2) + 2e^-. \quad (1.25)$$

It has been predicted by Wendell H. Furry in 1939 [18] but so far it has not been observed. Its existence would be possible if neutrino was a Majorana particle (its own antiparticle). This decay is not allowed in the SM as it violates lepton number conservation, thus creating particles without equivalent amount of antiparticles. The existence of the $0\nu\beta\beta$ -decay would mean a breakthrough in particle physics, since it would imply Majorana nature of neutrinos. It could potentially lead us to physics beyond the SM and, finally, it would also help us to determine the mass of neutrino

because its half-life is in direct relationship with neutrino mass:

$$\frac{1}{T_{1/2}^{0\nu}} = |m_{\beta\beta}|^2 G^{0\nu}(Q_{\beta\beta}, Z) |M^{0\nu}|^2, \quad (1.26)$$

where $T_{1/2}^{0\nu}$ is half-life of $0\nu\beta\beta$ -decay, $G^{0\nu}(Q_{\beta\beta}, Z)$ is the phase-space factor, $|M^{0\nu}|$ is the matrix element of $0\nu\beta\beta$ -decay and $m_{\beta\beta}$ is the effective neutrino mass defined as

$$m_{\beta\beta} = \sum_{i=1}^3 U_{ei}^2 m_i, \quad (1.27)$$

where U_{ei} are elements of PMNS matrix (eq. 1.12) and m_i are mass eigenvalues. To determine the value of $m_{\beta\beta}$ we also need to know $G^{0\nu}(Q_{\beta\beta}, Z)$ and $|M^{0\nu}|$ besides $0\nu\beta\beta$ -decay half-life itself. While $G^{0\nu}(Q_{\beta\beta}, Z)$ only depends on the $Q_{\beta\beta}$ -value and the proton number Z and can be calculated very precisely, $|M^{0\nu}|$ is a result of complicated nuclear models and brings more uncertainty into the equation. This, however, does not change the fact that $0\nu\beta\beta$ -decay could potentially be used as a tool for neutrino mass estimation.

1.3.2.1 Principle of detection

The most significant background of the $0\nu\beta\beta$ -decay is the $2\nu\beta\beta$ -decay. This is the main reason why we need to find a distinction between the two. In both cases we observe two electrons, the difference is, however, in their energy spectrum. In the case of $2\nu\beta\beta$ -decay, the two neutrinos carry away a fraction of the total released energy. The sum of the kinetic energies of electrons is equal to the difference between the $Q_{\beta\beta}$ -value of the decay and the kinetic energy carried by neutrinos. This results in a continuous spectrum (left spectrum in the figure 1.4). In comparison, during $0\nu\beta\beta$ -decay there is no emission of neutrinos, so the energy of electrons is always equal to the $Q_{\beta\beta}$ -value. Which results in a sharp peak (right peak in the figure 1.4). Based on this fact, $0\nu\beta\beta$ experiments measure total energy deposited in the detector. If we were able to recognize the peak at the end of the spectrum, we could confirm the existence of $0\nu\beta\beta$ -decay.

1.4 Experiments

There are a number of experiments focusing on the $0\nu\beta\beta$ -decay. One of the important factors of $0\nu\beta\beta$ experiment is the energy measurement resolution. It is important to achieve high energy resolution, otherwise the $0\nu\beta\beta$ peak would be smeared and hard to distinguish from the rest of the spectrum. The second important factor is the background suppression. Assuming that the $0\nu\beta\beta$ -decay exists, it is clear that the process is very rare, and it is thus important to ensure that the $0\nu\beta\beta$ is not lost in the background spectrum. Background suppression can be achieved by combination of different precautions. On the level of detector design, it is important to ensure radiopurity of its components and proper shielding against ambient radiation. It is also important to choose a suitable source isotope, as for some $Q_{\beta\beta}$ values the background in the region of interest is lower. Finally, additional background suppression can be done on the level of data analysis through data cuts.

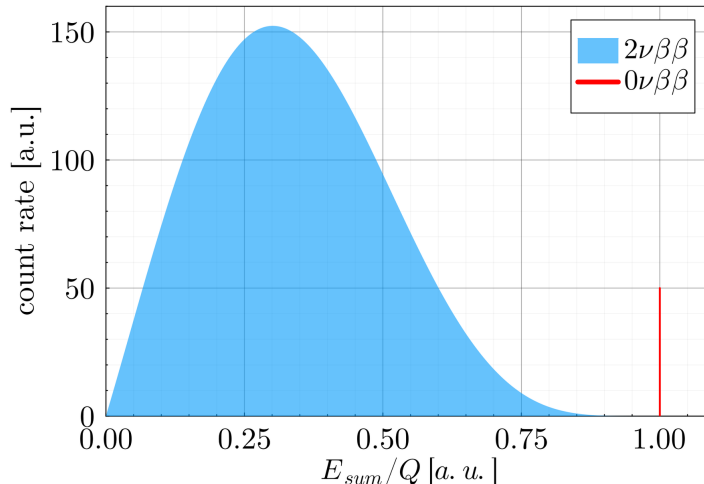


Figure 1.4: Comparison of theoretical $2\nu\beta\beta$ -decay electron spectrum (left) and $0\nu\beta\beta$ -decay electron spectrum (right). Observation of the sharp peak at the end of the spectrum would mean the existence of $0\nu\beta\beta$ -decay.

1.4.1 Homogeneous detectors

Most $0\nu\beta\beta$ experiments use so-called homogeneous design, where the part of the detector which provides energy measurement also contains an isotope which serves as the source of $0\nu\beta\beta$ -decay. These experiments can be further divided based on the method of energy measurement. A summary of these experiments can be found for example in [19].

1.4.1.1 Germanium detectors

Germanium detectors use the ^{76}Ge isotope as a $0\nu\beta\beta$ source. For detection, they typically use germanium semiconductor diodes made of enriched ^{76}Ge . The advantages of germanium detectors are very good energy resolution and high detection efficiency. In recent years, germanium detectors were mainly represented by two experiments: GERDA [20] and MAJORANA [21]. GERDA used a set of high-purity germanium devices suspended in a liquid argon cryostat, which provided both cooling and active shielding of the detector. With this setup, GERDA has achieved a background of 5.2×10^{-4} counts/(keV · kg · year) and an energy resolution of 3 keV at $Q_{\beta\beta} = 2039$ keV. It has set the lower limit of $0\nu\beta\beta$ half-life of ^{76}Ge at 1.8×10^{26} yr [22]. MAJORANA achieved even better energy resolution with a set of germanium detectors placed inside a high purity copper shield. Its lower limit of $0\nu\beta\beta$ half-life (^{76}Ge) is at 8.3×10^{25} yr [23].

Currently, the LEGEND collaboration is aiming to reach a limit of $0\nu\beta\beta$ half-life above 10^{28} years [24]. The first phase of the experiment called LEGEND-200 is currently in development. It uses 200 kg of germanium detectors. LEGEND-200 should improve background suppression by a factor of 2.5 with respect to GERDA and reach a $0\nu\beta\beta$ -decay half-life limit of about 10^{27} years. The second phase, LEGEND-1000, which should reach the limit of 10^{28} years, aims at even lower background of 10^{-5} counts/(keV · kg · year) (20 times better than LEGEND-200).

1.4.1.2 Bolometers

The second group of homogeneous detectors uses bolometers composed of enriched $0\nu\beta\beta$ source isotope. These bolometers operate at very low temperatures. Energy deposited in the bolometer results in an increase of temperature. Based on this change in temperature, energy of electrons can be measured. Since the 1990s, bolometers have been used to study six different nuclides (^{48}Ca , ^{82}Se , ^{100}Mo , ^{116}Cd , ^{124}Sn and ^{130}Te). A currently running experiment using the bolometric approach is CUORE [25]. It searches for $0\nu\beta\beta$ -decay in ^{130}Te using TeO_2 crystals for bolometers. It consists of 988 bolometers with a mass of about 750 g each. The energy resolution achieved by CUORE is 7.7 keV at 3034 keV. So far, the experiment has set a lower limit of $0\nu\beta\beta$ -decay half-life of 8.3×10^{25} yr (^{130}Te) with background of 1.49×10^{-2} counts/(keV · kg · year). The background is mostly caused by α particles generated by surface contamination.

Additional background suppression could be achieved by scintillating bolometers. Such a detector would use a scintillator containing the isotope of interest and a bolometer placed close to it, which would detect the emitted scintillation light. Coincidence of scintillation light and heat in the bolometer allows one to distinguish α particles from electrons or gamma photons. The CUPID experiment aims to use this technology to improve results of CUORE [26]. Another experiment using scintillating bolometers, which is currently in development, is AMoRE [27].

1.4.1.3 Xenon time projection chambers

Xenon experiments use the ^{136}Xe isotope as a $0\nu\beta\beta$ source. The enrichment process of natural xenon is relatively simple and xenon also has good scintillation properties, making it suitable for experiments. A recent xenon experiment is EXO. The EXO-200 detector uses a cylindrical time projection chamber filled with 110 kg of liquid xenon [28]. Energy deposition in the detector produces both scintillation light and ionization. The deposited energy is then reconstructed from these two signals. EXO-200 set a lower limit on the $0\nu\beta\beta$ -decay half-life of 3.5×10^{25} yr (^{136}Xe) with background of 2×10^{-3} counts/(keV · kg · year). A proposed successor of the EXO experiment is nEXO [29]. It will consist of a single time projection chamber containing 5000 kg of xenon. nEXO aims for a background of 7×10^{-5} counts/(keV · kg · year). This should be achieved by only selecting events from the innermost 2000 kg of xenon, taking advantage of the short attenuation length of gamma rays. The expected $0\nu\beta\beta$ -decay half-life limit set by nEXO is 1.35×10^{28} yr (^{136}Xe).

1.4.2 Tracko-calorimeters

In tracko-calorimeters, the source isotope is not included in the calorimeter measuring energies, but they are separated. A tracking detector is placed between the source and the calorimeter (figure 1.5). The tracker provides information about trajectories of particles passing through its volume. This trajectory measurement opens new possibilities of data analysis. First, it provides further background suppression as it reveals which particles did not come from the source. Secondly, in combination with a magnetic field, it can be used to distinguish between positively and negatively charged particles based on trajectory curvature. Finally, it can also be used to study different properties of the double beta decay, such as angular distribution of electrons or single electron energy spectra. The disadvantage of tracko-calorimeters is that it

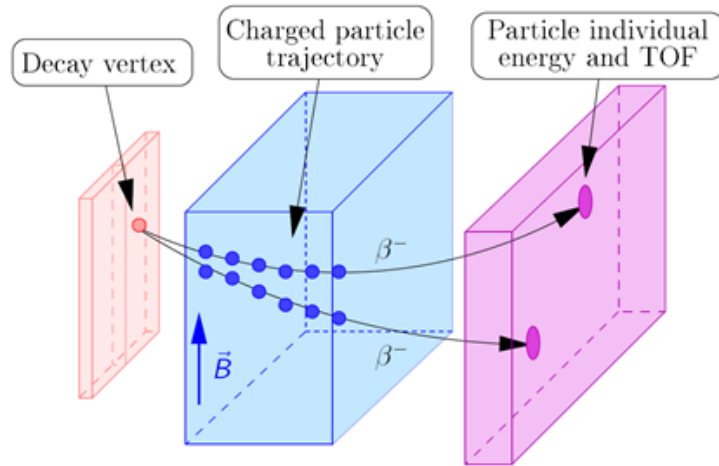


Figure 1.5: A scheme of the tracko-calorimeter detector design. The source is separated from the calorimeter by the tracker, which measures trajectories of passing particles. The figure was adapted from Ref. [32].

is not feasible to use very high mass of the source isotope (low density experiment). This comes from the fact that electrons from the $0\nu\beta\beta$ decay have to leave the source. Use of a source of large volume would mean that most of the electrons would be absorbed in the source itself. Examples of tracko-calorimeter experiments are NEMO-3 [30] or SuperNEMO which is the main topic of this thesis [31].

Chapter 2

The SuperNEMO Experiment

The SuperNEMO experiment is placed inside the LSM underground laboratory, located in the middle of a traffic tunnel going through the border between France and Italy (figure 2.1). Rock above the laboratory serves as a very effective shielding against cosmic rays, creating an ideal environment for low background experiments. Currently, the first SuperNEMO module called SuperNEMO demonstrator is in its commissioning phase.

The SuperNEMO demonstrator realizes the tracko-calor design using planar geometry 2.2. The source is in a form of a planar foil placed in the middle of the detector. The tracker is on the sides of the source foil. The calorimeter is segmented into smaller optical modules (OMs). These are placed around the tracker and the source foil. The three main components are surrounded by a coil which can be used to create approximately homogeneous magnetic field inside the detector. Finally, the whole detector is surrounded by shielding which suppresses ambient radiation.

2.1 Source foil

The source foil contains 6.11 kg of ^{82}Se isotope, serving as a source of $0\nu\beta\beta$ -decay [34]. The thickness of the foil is only 0.3 mm. It is important to use a thin layer of the isotope to ensure that electrons will not lose too much energy in the source itself or even get absorbed. Several isotopes have been considered to be used as a source from which ^{82}Se has been chosen since it meets multiple important criteria. The first important thing is the $Q_{\beta\beta}$ -value of an isotope. A higher $Q_{\beta\beta}$ is generally better as it allows for better suppression of background produced by ^{208}Tl and ^{214}Bi (see 2.4). $Q_{\beta\beta}$ -value of ^{82}Se is 2.996 MeV, which allows for sufficient background suppression. Another source of background is the $2\nu\beta\beta$ -decay (see the figure 1.4). It is, thus, important to choose an isotope with high $2\nu\beta\beta$ -decay half-life. The value for ^{82}Se is $T_{1/2} = 8.7 \cdot 10^{19}$ years. Finally, we also need to choose an isotope which we are able to shape to the form of a thin foil.

2.2 Tracker

Tracker allows us to see trajectories of charged particles. It is a wire chamber with 113×9 drift cells on each side of the detector. A schematic view of a tracker cell can be seen in the figure 2.3a. Each cell consists of a central high-voltage wire (anode)

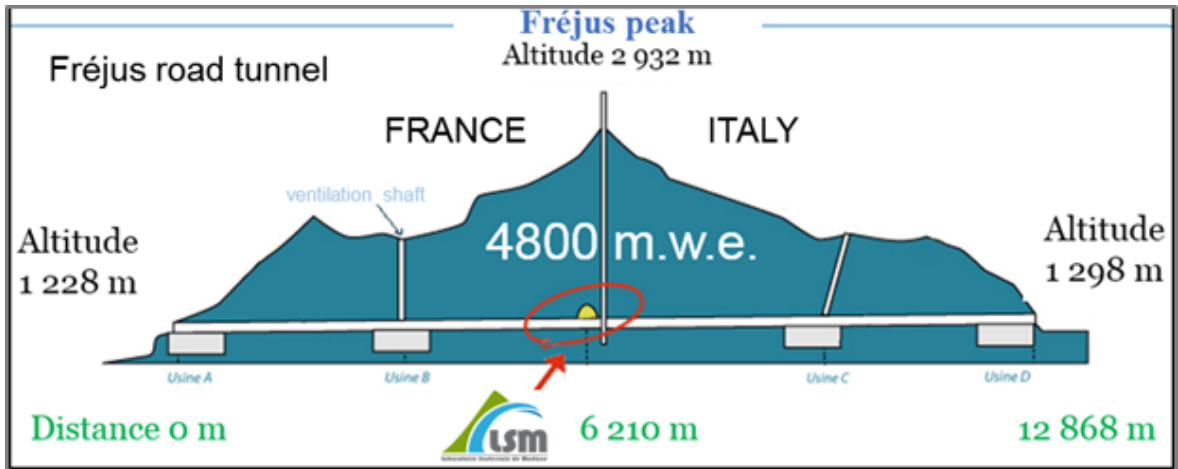


Figure 2.1: Scheme of the Fréjus traffic tunnel between France and Italy. LSM underground laboratory containing the SuperNEMO experiment lies approximately in the middle. The figure was adapted from Ref. [33].

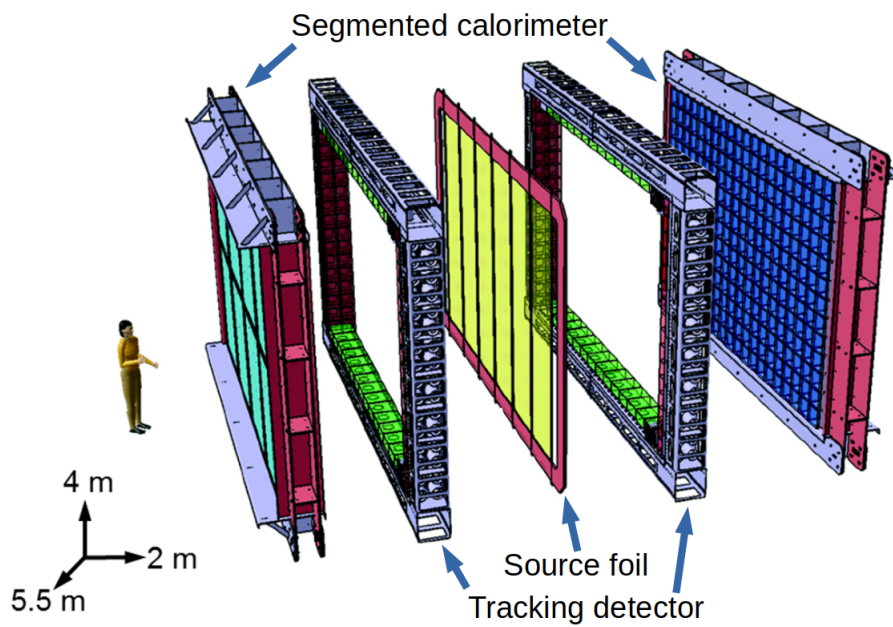


Figure 2.2: A picture of the SuperNEMO demonstrator design. There is the source foil in the middle, the tracker on its sides and the calorimeter around the detector. The figure was adapted from Ref. [32].

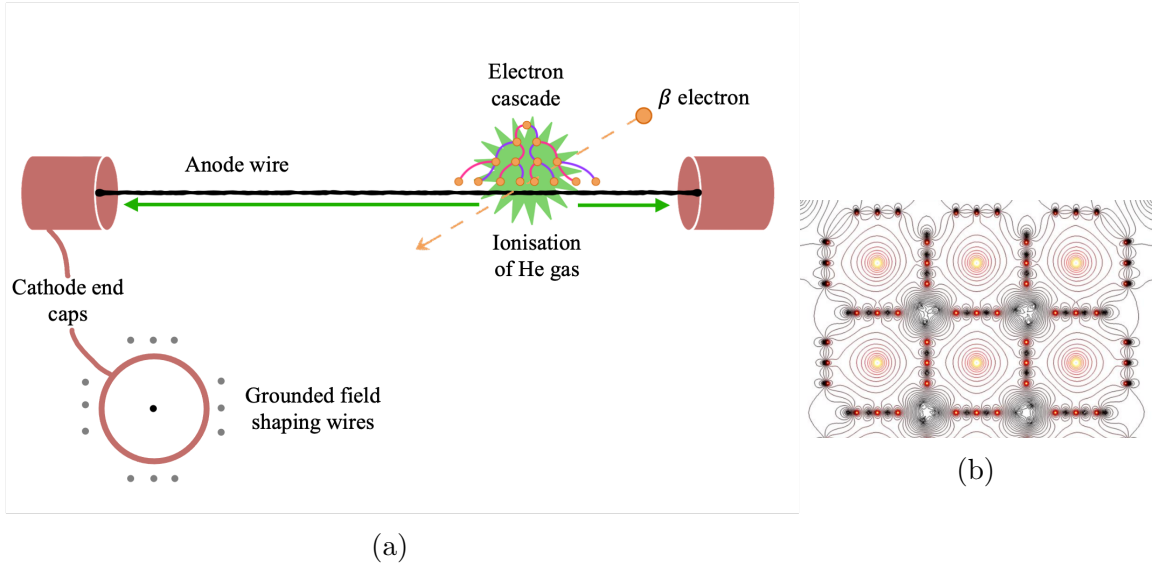


Figure 2.3: a) Side view of a tracker cell. There is a high-voltage wire (anode) in the middle and copper rings (cathodes) on its ends. The dashed line represents a passing electron, which caused an avalanche of electrons and consequential propagation of plasma along the anode. The figure was adapted from Ref. [35]. b) Electric field in tracker cells. (top view) Courtesy of Cheryl Patrick (SuperNEMO collaboration).

surrounded by 12 grounding wires. On each end of the anode, there is a copper ring (cathode). The inside of the tracker is filled with gas (95 % of helium with 4 % of ethanol and 1 % of argon). Passing particles ionize the gas, creating free electrons which can be attracted by the electric field around anodes (figure 2.3b). While being pulled to an anode, electrons ionize another nuclei. This creates electron avalanches, resulting in a measurable current signal. The time it takes for the avalanche to reach the anode gives us an information about the particle’s distance from the anode. Some avalanche electrons recombine with ions close to the anode. This recombination creates photons which cause further ionization of nearby gas atoms, creating more free electrons. These electrons are again pulled towards the anode, creating plasma along the anode. This cycle of ionization repeats, until the plasma reaches both of the cathode end caps. This results in a cathodic signal. Using the difference of times when the signal hit the top and the bottom cathode, we can calculate the height in which the particle passed. Properties of cathodic and anodic signals are discussed in more detail in section 3.2.1.

2.3 Calorimeter

The calorimeter allows us to measure energies of electrons coming from the $0\nu\beta\beta$ -decay — the main quantity of interest. The whole calorimeter is segmented and consists of 712 so-called optical modules (OMs; figure 2.4a). These modules are placed in two main walls parallel to the source foil, as well as above and below (“gveto”) and on the sides of the source foil (“xcalo”). Each optical module is a scintillation detector consisting of a photomultiplier tube (PMT) and a block of plastic scintillator (polystyrene; figure 2.4b). The “xcalo” and “gveto” OMs are reused from the previous experiment NEMO-3. They use 5” PMTs, and their resolution is 12 % at 1 MeV for “xcalo” and 15 % at 1 MeV for “gveto”. OMs used in the main walls use 8” PMTs and their scin-

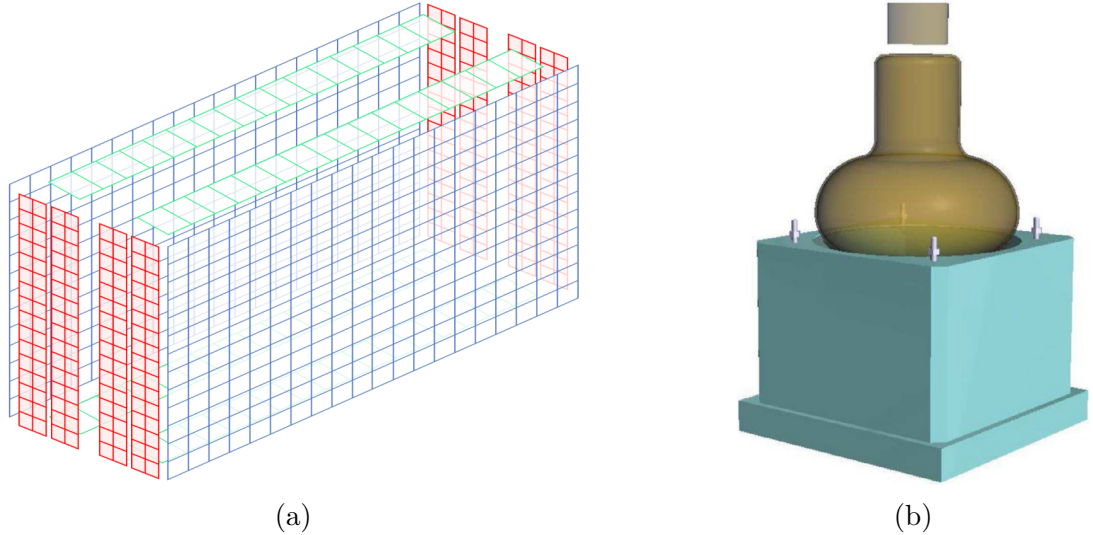


Figure 2.4: a) A scheme of the calorimeter, depicting its different sections. We divide the calorimeter into main walls (blue), “xcalo” (red) and “gveto” (green). The figure was adapted from Ref. [37]. b) Optical module consisting of a photomultiplier tube and a block of scintillator.

tillator blocks contain two additional substances improving light collection efficiency of PMT: 0.6 % of para-terphenyl (pTP) and 0.05 % of 1,4-bis(5-phenyloxazol-2-yl) benzene (POPOP). Several concentrations of these additives have been tested to find the optimal one [36]. Thanks to that, the main wall modules reach resolution of about 8 % at 1 MeV. The resolutions given in this paragraph are, however, simplified idealized values currently used in the simulation. They are based on real measurements, but the measurements were carried out in ideal conditions before the calorimeter was assembled. The actual achieved energy resolutions need to be studied again with for the fully built detector.

2.3.1 Optical module geometry identifier

To identify individual parts of the SuperNEMO detector, a so-called geometry identifier (GID) is used. For the purposes of this work, the OM GID is the most important. Each of the three groups of OMs (main wall, xcalo, gveto) has its respective GID format. GID of main wall modules is in format M:side:column:row (ex. M:1.4.9). Here side is either 0 or 1 denoting Italian or French side respectively, column is an integer from 0 to 19 and row is an integer from 0 to 12. Gveto GID is in format of G:side:row:column (ex. G:1.1.7). This time row is 0 or 1 denoting bottom or top of the detector respectively and column is an integer from 0 to 15. The xcalo GID format is X:side.part.column.row (ex. X:1.0.0.9). Here we also introduce the “part” number (0 or 1) because on each side of the detector there are two groups of xcalo OMs (see figure 2.4a). For xcalo the column number is either 0 or 1 and the row number goes from 0 to 15.

2.4 Background

When searching for a phenomenon, so rare as $0\nu\beta\beta$ -decay, a careful study of background is especially important. There are several sources, which are able to produce electron pairs with total energy in our region of interest, mimicking the signal of $0\nu\beta\beta$ -decay. We divide background sources into two groups: internal and external. Internal background originates from decaying contaminants of the source foil. In contrast, external background comes from all other sources outside the source foil. These can be contaminants of other parts of the detector, as well as radiation and radionuclides coming from outside the detector.

2.4.1 Internal background

The first process causing the appearance of internal background is the $2\nu\beta\beta$ -decay of ^{82}Se . This background cannot be removed, as it comes from the source isotope itself, which obviously has to be present. The only way to deal with this background is to achieve sufficient energy resolution to differentiate the $2\nu\beta\beta$ energy spectrum from $0\nu\beta\beta$.

Other two sources of internal background are beta decays of ^{208}Tl and ^{214}Bi . The Q_β value of ^{208}Tl is 5 MeV, which is above the $Q_{\beta\beta}$ -value of ^{82}Se allowing it to mimic the signal. The mimicking can happen in following ways [38]:

- Beta decay accompanied by an electron conversion
- Beta decay followed by Møller scattering of beta particles in the source foil
- Beta decay to an excited state, deexcitation by emitting a gamma ray followed by Compton scattering

The Q_β value of ^{214}Bi is 3.3 MeV, which is also higher than $Q_{\beta\beta}$ of ^{82}Se . ^{214}Bi decays into ^{214}Po . The ^{214}Po then α decays to ^{210}Pb with a short half-life of 0.164 ms. This coincidence of β electron and α can be recognized and suppressed thanks to the track reconstruction.

2.4.2 External background

External background can generally come either in the form of electrons or high energy gammas. An external electron can transverse the whole tracker perpendicularly to the source foil. This leaves a track in both halves of the tracker, which can look like a $0\nu\beta\beta$ event. Such events, however, can be recognized thanks to timing of the calorimeter as times of two subsequent hits caused by a single electron are different from times of hits caused by two electrons coming from the source foil. External gammas can again create background through different interactions. These can be electron-positron pair creation, two consecutive Compton scatterings or a Compton scattering followed by a Møller scattering.

External background can come from a wide range of sources. These can be cosmic muons, natural radionuclides present in the environment of the underground laboratory, or even radionuclides present in different parts of the detector. A detailed discussion of all sources can be found in [38]. A major source of external background is ^{222}Rn . It emanates from the mountain into the environment of the laboratory. ^{222}Rn is a very

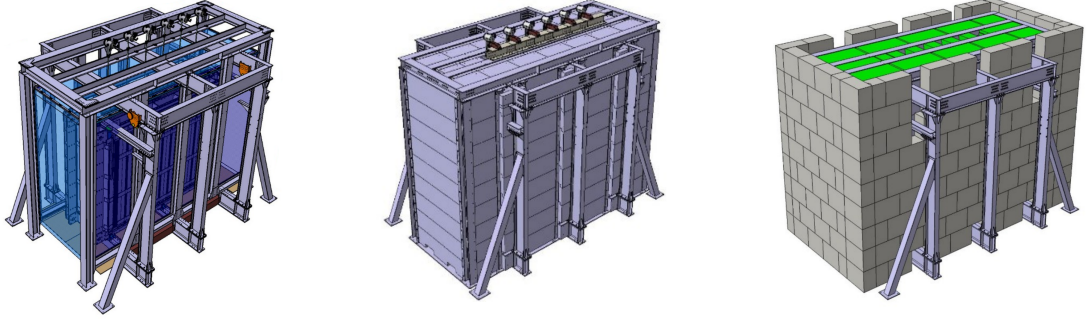


Figure 2.5: Shielding layers of the SuperNEMO detector: anti-radon shielding (left), iron shielding (middle), neutron shielding (right).

diffusive gas, allowing it to enter the inside of the tracker. Through decay within the ^{238}U decay chain, ^{222}Rn produces ^{214}Bi . ^{214}Bi can then decay in proximity of the source foil, mimicking the $0\nu\beta\beta$ signal as described in the previous section.

2.5 Shielding

In order to reduce external background as much as possible, it is necessary to ensure sufficient shielding of the detector. The detector is shielded against cosmic rays by 1700 meter thick layer of rock above the underground laboratory. This reduces the flux of cosmic muons by six orders of magnitude compared to the surface. Measurements performed inside the laboratory measured muon flux of $\Phi_\mu = 4.73 \text{ m}^{-2}\text{d}^{-1}$ [39]. Besides this natural shielding, there are also multiple layers installed around the detector. To reduce the amount of ^{222}Rn inside the detector, an air recycling system has been developed. The detector is enclosed in a tent, which is connected to a filtration system. Air inside the tent circulates through the filtration system, where ^{222}Rn is captured by activated charcoal. A significant portion of background gamma photons comes from neutron capture, which is why strong neutron shielding is also important. Neutrons are effectively shielded by materials containing elements with low atomic number. In the SuperNEMO experiment, neutron shielding will be constructed from polyethylene bricks filled with water. As a gamma shielding, on the other hand, we need material with high density and atomic number. A layer of iron shielding has been chosen for this purpose. All shielding layers can be seen in the figure 2.5. The effect of neutron and gamma shielding on measured background spectrum can be seen in the figure 2.6. A first part of the iron shielding is currently being installed, as can be seen in the figure 2.7.

2.6 Energy calibration system

Before we can start to measure energies of electrons and to look for the peak at the end of the double beta decay spectrum (figure 1.4) we need to calibrate the calorimeter. It is important to realize that properties of individual OMs will slightly differ as well, as they will slowly change with time. Therefore, it is necessary to calibrate each OM individually and to perform the calibration measurements periodically in sufficient time intervals.

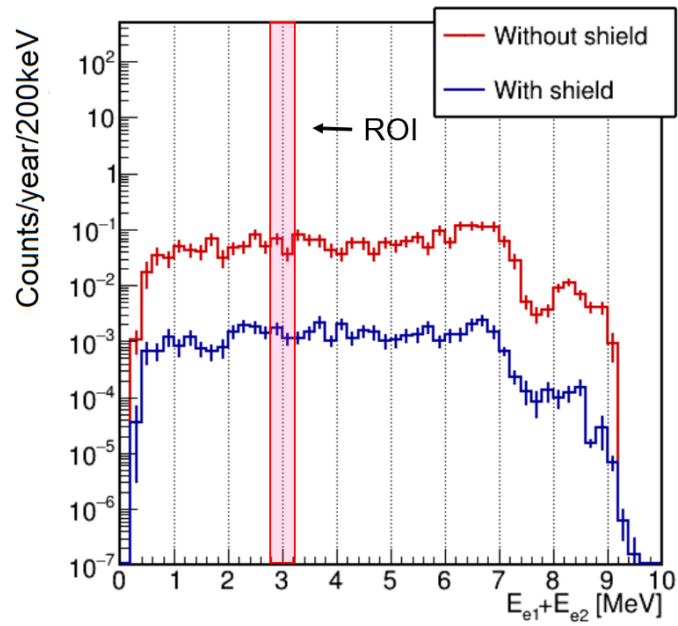


Figure 2.6: Simulated two electron background spectra with neutron and gamma shielding and without it. We can see that the use of shielding leads to background reduction of about two orders of magnitude. The figure was adapted from Ref. [38].

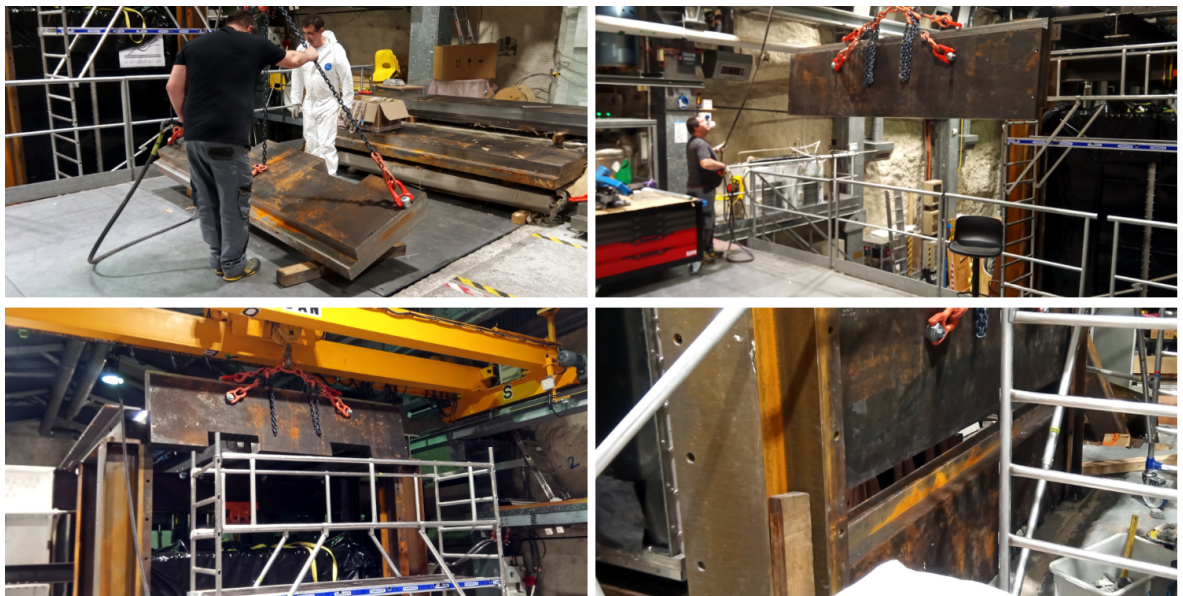


Figure 2.7: Photos from currently ongoing iron shielding installation.

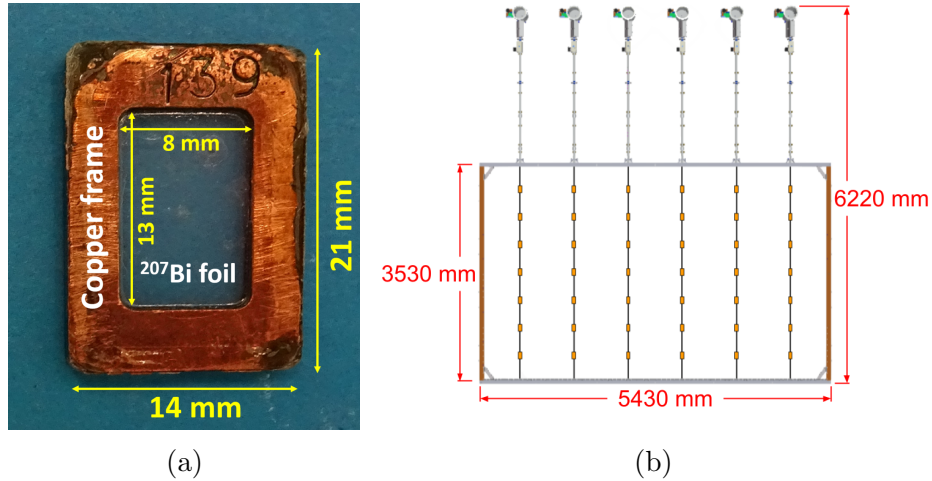


Figure 2.8: a) A ^{207}Bi calibration source consisting of a Mylar foil, a copper frame and a small droplet of ^{207}Bi in the middle (not visible). b) Automatic deployment system used to position the calibration sources in the middle of the detector. The small orange rectangles represent the calibration sources. The figure was adapted from Ref. [34].

The calibration measurement will be performed using a system of 42 calibration sources. Each source contains a small droplet of ^{207}Bi sandwiched between two transparent Mylar foils. The foils are stretched into a copper frame so that the ^{207}Bi droplet is in the middle (figure 2.8a). The positions of the ^{207}Bi droplets have been measured to ensure that they did not leak under the frame [34]. Before the calibration measurement, we need to place the calibration sources on chosen positions inside the detector. These positions should be the same for each calibration measurement. During this process, the detector also must stay sealed so that there are no leaks of the tracking gas. To place the sources in the middle of the detector, an automatic deployment system has been built (figure 2.8b). This system consists of 6 rods connected to stepper motors, using which we can place the calibration sources on precise positions along the source foil.

2.6.1 Principle of energy calibration

^{207}Bi atoms can undergo so-called internal conversion (IC) — a process during which an excited nucleus transfers its energy to one of the orbital electrons. This results in an emission of the electron and an X-ray. The electron can come from any of three electron shells commonly referred to as K, L and M-shells, where K is closest to the nucleus having the highest probability of IC and M is the most distant one with the lowest probability of IC. In a calibration measurement, we detect these IC electrons. We can then use the measured data to find a relationship between known energies of IC electrons and a charge collected in the optical module. Since the excitation energies of the nucleus are discrete as well as ionisation energies of electrons from different shells, the spectrum of IC electrons is also discrete. Having discrete spectrum is ideal for calibration, because it allows us to assign concrete energies to measured peaks (contrary to continuous spectrum of β -decay, for example). Moreover, energies of ^{207}Bi electrons are equally spaced (482, 976 and 1682 keV), which is also good for precision of the calibration. In the figure 2.9 we can see a simplified decay scheme of ^{207}Bi

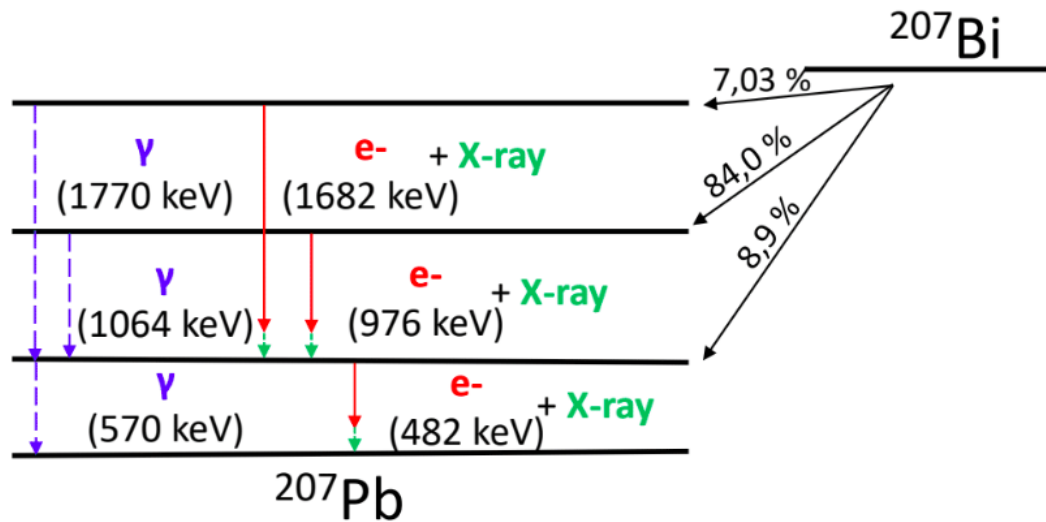


Figure 2.9: A simplified decay scheme of ^{207}Bi containing the most frequent transitions. ^{207}Bi can emit gamma rays through gamma decay or electrons and X-rays through internal conversion.

containing IC electrons from the K-shell. Finally, ^{207}Bi IC energies cover the interval of typical energies of electrons from double beta decay of ^{82}Se .

Chapter 3

SuperNEMO data formats and calibration data processing

3.1 Simulated data

In order to perform simulations, SuperNEMO collaboration uses its own simulation system called Falaise [40]. The system is based on Geant4 package developed in CERN [41]. Falaise contains information about geometry of the detector, properties of its parts, different types of decays, etc. It also offers a simple user interface which contains a range of options from which a user can choose to set up a simulation. Thanks to this, the setup of a simulation is very quick and convenient.

For standard use, Falaise offers 3 programs — flsimulate, freconstruct and flvisualize. Flsimulate simulates passage of particles through the detector. It produces information about particle interactions in materials and about energy deposited in different points of particle's trajectory. Flsimulate provides detailed simulation data about particles, which is not available in actual measurements. An output of Falaise simulation comes in a form of so-called brio file. Inside this file, data are divided into data banks. Data produced by flsimulate are saved in SD bank (Simulated Data). It contains information about particle types, energies, trajectories and individual interactions. A visualization of the SD bank from a single event can be seen in the figure 3.1a.

Data produced by flsimulate can be further processed by freconstruct. A run of freconstruct consists of so-called pipeline modules. These modules can perform different tasks from printing the data to complex analysis. As the name suggests, it is possible to chain pipeline modules, so that the output of one module is the input of the next one. A user can use predefined modules as well as define new ones to customize data processing. The main purpose of freconstruct is to provide response of the detector based on data produced by flsimulate. The output of freconstruct is another brio file. This file contains the SD bank previously produced by flsimulate as well as 4 other banks. First of them is CD bank (Calibrated Data). This bank contains quantities detected by different parts of the detector, including their uncertainties. Then there are TCD (Tracker Clustering Data) and TTD (Tracker Trajectory Data) banks. TCD contains information about clusters of tracker hits. These clusters should correspond to tracks of individual particles. From these clusters, trajectories of individual particles are extracted using a tracking algorithm. These trajectories are saved into TTD bank. Finally, there is PTD bank (Particle Track Data) which contains information

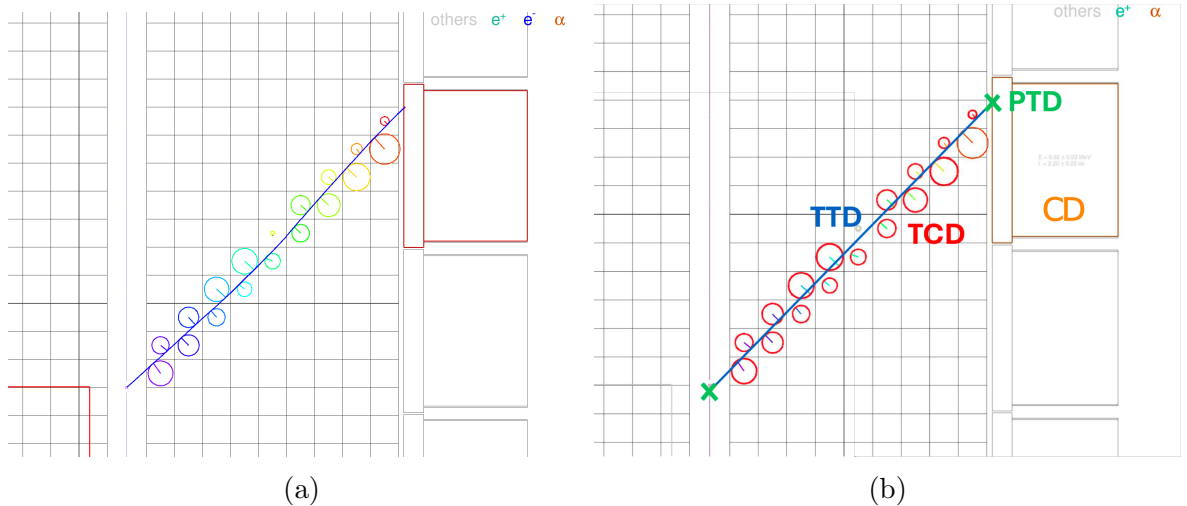


Figure 3.1: In the figure a), we can see an example of visualized data from the SD data bank. There is an electron (blue curve) coming from a calibration source to an OM (red). Along the way, it passes through several tracker cells (coloured circles). In the figure b), we can see data reconstructed based on the SD bank. There is a cluster of tracker hits (red) saved in the TCD bank, a reconstructed track (blue) saved in the TTD bank and two vertices of the track (green) saved in the PTD bank. The energy measured by the triggered OM is saved in the CD bank. The picture b) was edited with respect to the original flvisualize output to emphasise individual data banks.

reconstructed from its trajectory. These are the charge of the particle and vertices at the start and at the end of the trajectory. A visualization of reconstructed data banks can be seen in the figure 3.1b.

The third Falaise program called flvisualize is used to visualize data produced by flsimulate and freconstruct. Examples of such visualization are figures 3.1a and 3.1b. The main benefit of flvisualize is that it allows us to gain an intuition about data and to check whether the simulation behaves as we expect.

3.2 Real data

During the real measurement, SuperNEMO uses a complex system of electronics to extract signals from the tracker and the calorimeter. Since saving continuous signal from the whole detector would be very inefficient, SuperNEMO uses a trigger system to decide when to keep the data. Trigger looks for time and space coincidence between signal from the tracker and the calorimeter. Once the trigger condition is met, the signal from the whole detector (measured during a small time window around the trigger time) is saved. A unique trigger ID is assigned to these data. Signals from both the tracker and the calorimeter have characteristic waveforms, which are used to extract information about the particle's trajectory and energy.

3.2.1 Tracker signal

A tracker cell consists of three parts — anode, top cathode and bottom cathode (see the figure 2.3a). Each of these parts provides its own voltage signal. A raw signal from anode and both cathodes can be seen in the figure 3.2. Here t_0 is the drift time it takes

for the electron avalanche to reach the anode wire from the original point of ionization. t_5 and t_6 are times when the plasma propagating along the anode wire reaches the bottom and the top cathode, respectively. An important thing to notice here is that the spikes in the cathodic signal are accompanied by spikes in the anodic signal. Because of that, the spikes in the anodic signal represent the exact same information as the cathodic signals. The only difference is that, purely from the anodic signal, we are not able to distinguish which spike corresponds to the bottom cathode and which corresponds to the top one. Since voltage waveforms have variable amplitudes, we cannot define a single voltage threshold. Because of that, it is more convenient to work with derivatives of these waveforms. An example of the differentiated cathodic signal and anodic signal can be seen in figures 3.3 and 3.4 respectively. We can see that in the anodic signal, we define 4 new timestamps t_1 to t_4 . These can be used as a substitute for t_5 or t_6 , if one of them is missing. Ideally, times t_0 to t_6 should be measured from the time of the tracking gas ionization. This time, however, is not known, so we need to choose a different timestamp which is as close to the time of ionization as possible. For this purpose, we choose the time in which an OM was triggered by the particle. This is illustrated in the figure 3.5. In the figure t_a is the time of ionization, t_b is the time when the electron avalanche reaches the anode, t_e is the time it takes the particle to reach the OM from the point of ionization and t_{OM} is the time when the OM was triggered. For all reasonable cases, electrons detected by SuperNEMO can be considered relativistic. This means that the time t_e is in order of ns, while t_0 is in order of μs . Thanks to that, we can consider t_{OM} to be very close to t_a and approximate $t_0 = t_b - t_a \approx t_b - t_{OM}$.

Timestamps t_5 and t_6 are used to calculate the vertical coordinate of particle's trajectory. Based on the length of the tracking wire and the speed of plasma propagation, we can calculate the height in which the particle passed the wire. The drift time t_0 represents an information about horizontal distance in which the particle passed the tracking wire. The radius in which the particle passed the anode is calculated from t_0 using so-called drift model. A drift model describes the relationship between the drift time and the radius. This relationship depends on the shape of electric field around the anode. The shape has been studied by both experiments and simulations, resulting in two drift models. These can be seen in the figure 3.6. The red line represents the experimental drift model, while the blue line represents the one based on simulations. We can see that both of the models are piecewise functions. The first part of the model describes radii from 0 to 22 mm. In this interval, the models describe an approximately circular field in the central part of the tracker cell. In the interval from 22 to $22\sqrt{2}$ mm (~ 31.1 mm), the models describe the edges of the tracker cell. For radii larger than $22\sqrt{2}$ mm, the models are extrapolations without meaningful information.

3.2.2 Calorimeter signal

A typical waveform recorded by an OM when hit by a particle can be seen in the figure 3.7. The integral of the waveform is proportional to the total charge collected in the OM during interaction with the particle. This charge is in relationship with the energy deposited in the OM. Finding this relationship is the goal of the calibration.

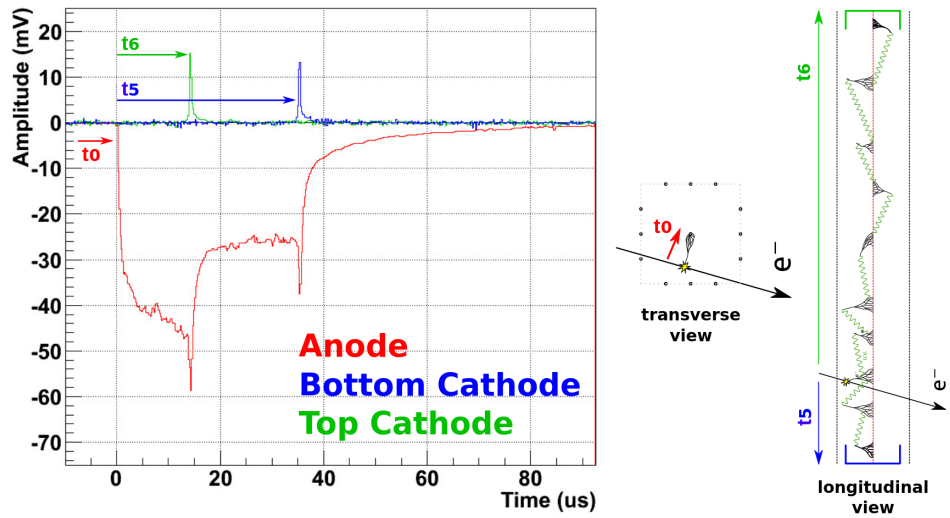


Figure 3.2: Cathodic and anodic signal of a tracking cell. We can see that t_0 corresponds to propagation of electron avalanche to the anode. t_5 and t_6 are times when the plasma propagating along the anode reaches the bottom cathode and the top cathode, respectively. In the anodic signal, there are two spikes corresponding to spikes in signal of bottom and top cathode. Courtesy of SuperNEMO collaboration.

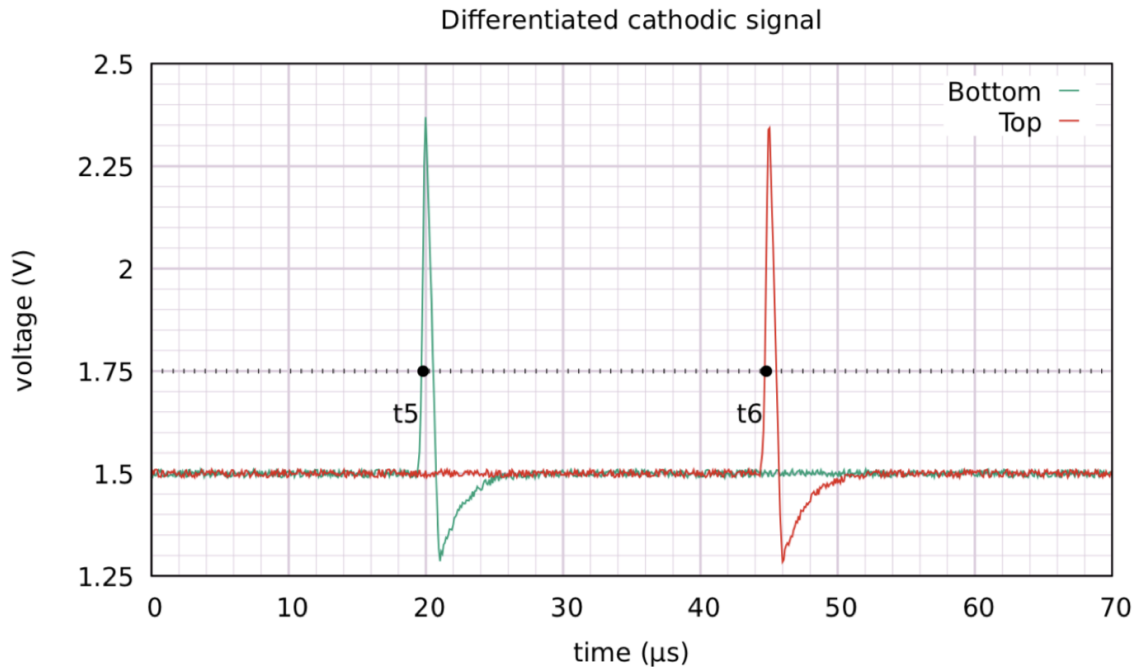


Figure 3.3: Differentiated cathodic signal. We can see two timestamps t_5 and t_6 corresponding to times when plasma reaches the bottom and top cathode. Courtesy of SuperNEMO collaboration.

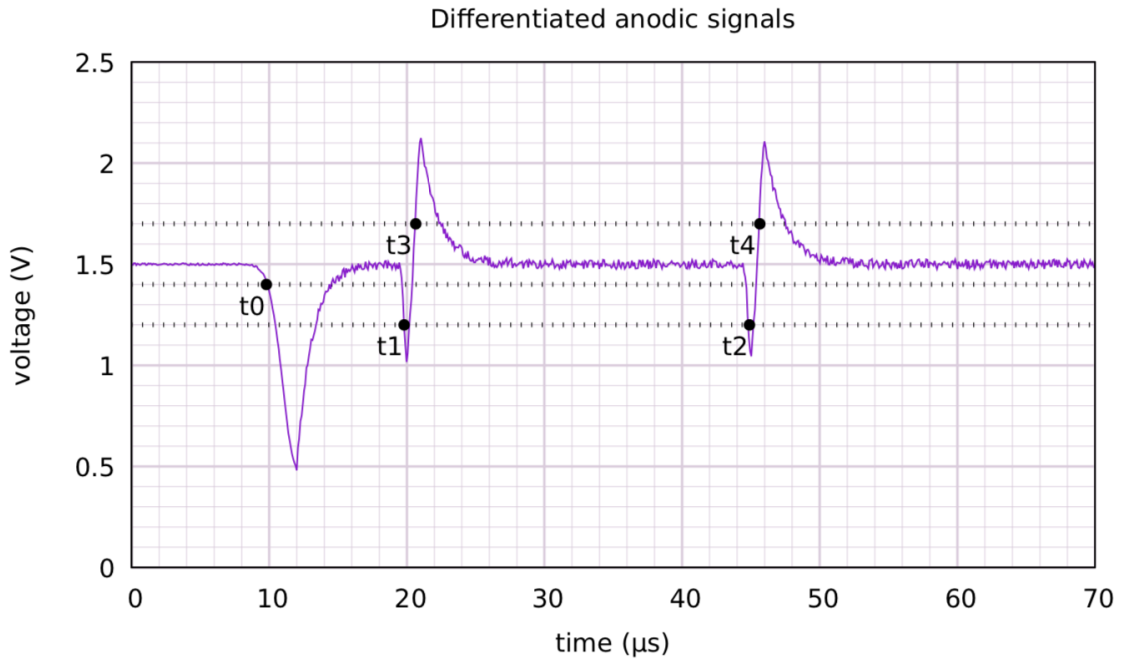


Figure 3.4: Differentiated anodic signal. t_0 represents the drift time and t_1 to t_4 represent times when plasma reaches the bottom and top cathode. Courtesy of SuperNEMO collaboration.

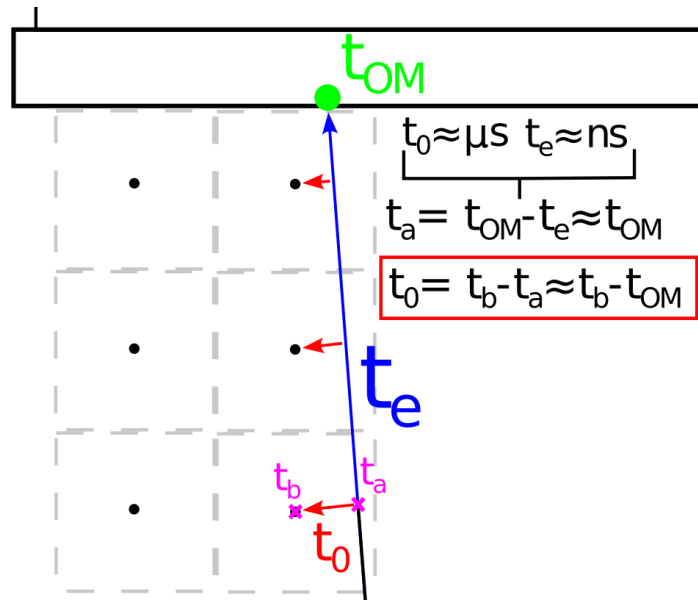


Figure 3.5: An illustration of approximation in drift time calculation. Here t_a is the time of ionization, t_b is the time when the electron avalanche reaches the anode, t_e is the time it takes the particle to reach the OM from the point of ionization and t_{OM} is the time when the OM was triggered. We do not know t_a to calculate $t_0 = t_b - t_a$, but because t_e is very short, we can approximate t_b with t_{OM} . This applies for all tracker hits.

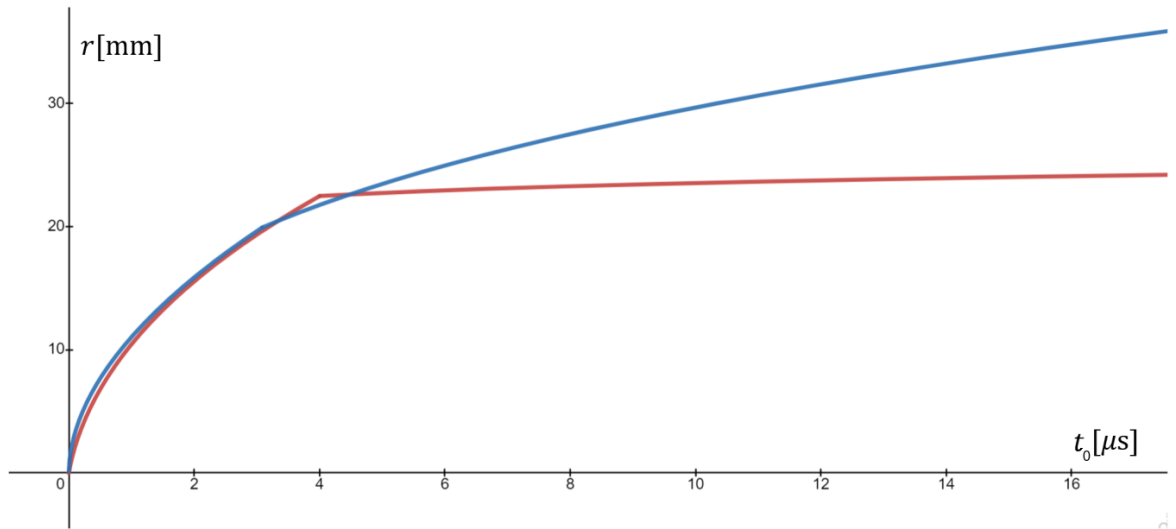


Figure 3.6: A plot of two drift models describing the relationship between the radius in which a particle passed an anode r and the drift time t_0 . The red line corresponds to a model obtained through experiments, while the blue line represents one based on simulations. The figure was adapted from Ref. [42].

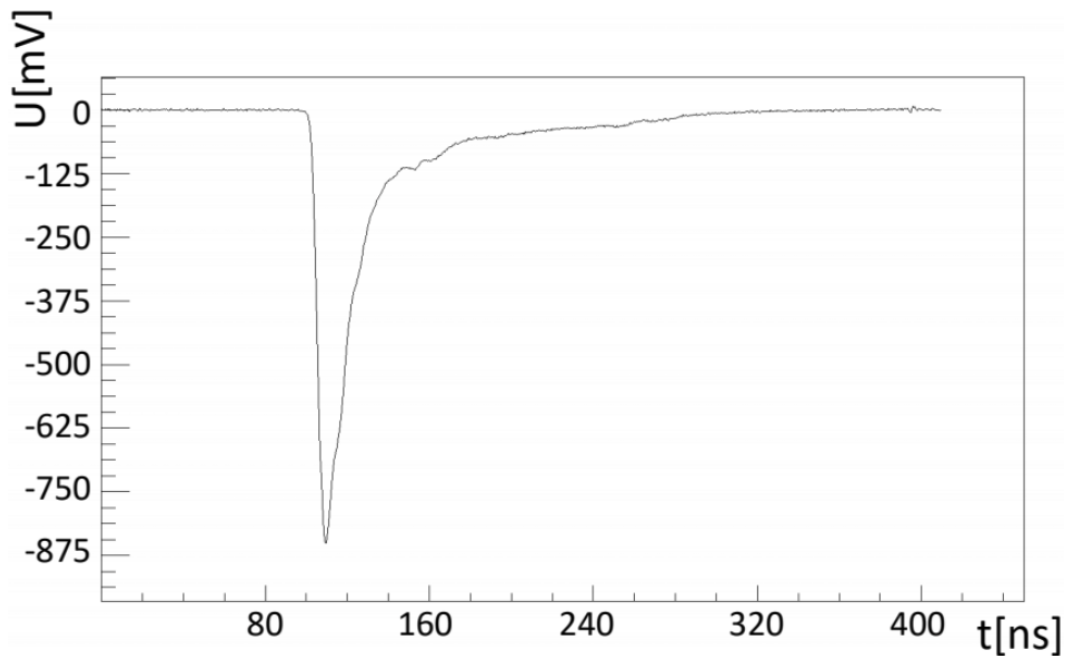


Figure 3.7: An example of waveform captured by an OM. The integral of the waveform corresponds to the energy of the particle.

3.2.3 SuperNEMO data formats

SuperNEMO uses a number of data formats to save and process data. These range from unstructured and simple ones used during the data acquisition (DAQ) to more structured ones which should provide a clear representation of the data suitable for data analysis.

3.2.3.1 Commissioning binary data (CBD)

Raw signals from the SuperNEMO detector are processed by so-called SNCrateSW DAQ software, which produces data files in what we call Commissioning Binary Data format. Data from the detector come in 6 data streams, resulting in 6 CBD files. Each file comes from one DAQ crate (3 from tracker, 3 from calorimeter). Signals in this format are not ordered by time nor their trigger ID. CBD are, however, very compact, optimized for the DAQ and serve as a basis for more structured formats.

3.2.3.2 Raw hit data (RHD) and Raw trigger data (RTD)

6 CBD files obtained during measurement run are later converted into 6 Raw Hit Data files. Each of these files contains signals from one part of the detector, sorted by their trigger IDs. These 6 files are then converted into one Raw Trigger Data file. This file contains signals from the whole detector, sorted by their trigger ID. This format represents signals as they are registered by readout electronics after a trigger. RTD format can already be used for data analysis, but it still contains some low-level information. It is more suitable for diagnostic of DAQ rather than for complex analysis tasks.

3.2.3.3 Raw event data (RED)

Finally, the RTD file is converted into Raw Event Data using an event builder which looks for triggers in a small time window and merges data with different trigger IDs into events based on their time coincidence. The idea is that these events provide similar data structure as events produced by simulation software Falaise. This makes working with RED files very natural for people previously working with simulations.

3.2.3.4 Unified digitized data (UDD)

Even though the RED format can already be quite conveniently used by data analysts, the final goal is to unify data formats of simulated and real data. UDD is a step in this direction. Real data formats up to RED were processed by a software separate from Falaise called SNFrontEndElectronics (SNFEE). UDD contains the same information as RED, but the data are in a form of Falaise data bank and are saved into a brio file readable by Falaise. The difference between UDD and the data banks produced by Falaise simulation is in the type of information included. The UDD bank contains information about electronic signals measured by different parts of the detector. These signals have to be further processed to extract physical quantities such as energy. This requires calibration of detector components. In the case of simulation, on the other hand, we get the physical quantities right away as a model of the electronics is not included in the simulation.

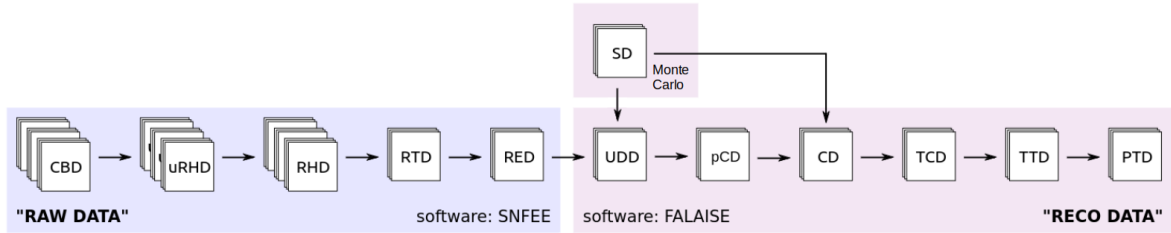


Figure 3.8: A diagram representing relationships between different data banks. Real data will be transformed from the low level CBD formats up to the same data banks, which are produced by Falaise simulations.

3.2.3.5 Future formats

The final step is to produce the same data banks as those produced by simulation based on the UDD data. First, the data from UDD will be transformed into pCD (pre-Calibrated Data). This new data bank contains preprocessed information from UDD. Some detailed information from UDD is discarded, and only the values needed to reconstruct the physical quantities of interest are kept. Finally, from the pCD format, the same data banks as the ones from the Falaise simulation will be produced. The continuity of all described data banks can be seen in the figure 3.8.

3.3 Calibration data

In the present, more than 100 hours of data with calibration sources deployed have already been measured. Measurement runs without the calibration sources have also been performed. These allow us to study the amount of background which we can expect in the calibration data. In the table 3.1 we can see a list of measurement runs data of which were used for analysis presented throughout this work.

3.3.1 Event

Data files in the RED format were used for analysis throughout the whole work. We can see an example of a typical event in the figure (3.9). Each event contains tracker hits and OM hits. A tracker hit gives us information about signal captured by a single tracker cell. It consists of tracker cell ID and timestamps extracted from anodic and cathodic signal (figures 3.3 and 3.4).

OM hit contains OM ID, time when the OM was triggered and information about measured waveform. The integral of the waveform is calculated to extract total collected charge, which gives us information about the particle's energy. The timestamp from the OM is also useful, since this is the reference time from which the timestamps t_0 to t_6 of tracker cells are measured (section 3.2.1).

3.3.2 Event selection

The first step in the data analysis is to filter out the background events using a properly chosen set of data cuts. In the case of calibration data, we only want to keep the events where an electron comes from a calibration source and hits an OM. Recognizing such events requires precise knowledge about event geometry.

Run number	Date	Measurement length	Number of events	Type
1086	JUL/31	~ 3 h	$5 \cdot 10^6$	calibration run
1087	JUL/31	~ 10 h	$4.4 \cdot 10^6$	background run
1090	AUG/01	~ 3 h	$6 \cdot 10^6$	calibration run
1093	AUG/01	~ 10 h	$5.3 \cdot 10^6$	background run
1097	AUG/02	~ 3 h	$5.5 \cdot 10^6$	calibration run
1100	AUG/02	~ 10 h	$5.5 \cdot 10^6$	background run
1105	AUG/03	~ 3 h	$8.2 \cdot 10^6$	calibration run
1108	AUG/03	~ 10 h	$4.3 \cdot 10^6$	background run
1112	AUG/04	~ 3 h	$6.9 \cdot 10^6$	calibration run
1115	AUG/04	~ 10 h	$4.7 \cdot 10^6$	background run
1119	AUG/05	~ 3 h	$6.2 \cdot 10^6$	calibration run
1126	AUG/06	~ 3 h	$8.2 \cdot 10^6$	calibration run
1133	AUG/07	~ 3 h	$5 \cdot 10^6$	calibration run
1149	AUG/11	~ 3 h	$5.2 \cdot 10^6$	calibration run
1156	AUG/12	~ 3 h	$6.1 \cdot 10^6$	calibration run
1163	AUG/13	~ 3 h	$6.5 \cdot 10^6$	calibration run
1170	AUG/14	~ 3 h	$6.3 \cdot 10^6$	calibration run
1175	AUG/15	~ 3 h	$6.4 \cdot 10^6$	calibration run
1180	AUG/16	~ 3 h	$6.3 \cdot 10^6$	calibration run
1190	AUG/19	~ 3 h	$5.3 \cdot 10^6$	calibration run
1195	AUG/20	~ 3 h	$6.2 \cdot 10^6$	calibration run
1200	AUG/21	~ 3 h	$5.8 \cdot 10^6$	calibration run

Table 3.1: A list of measurement runs, data of which were used for analysis, presented throughout this work.

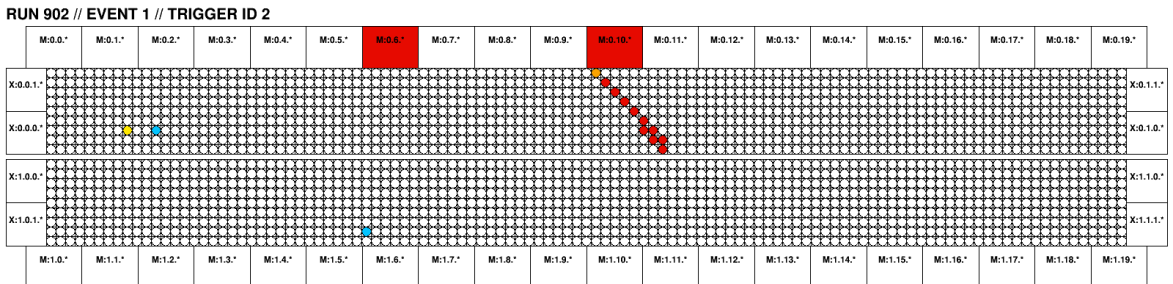


Figure 3.9: An example of ^{207}Bi calibration event. Coloured circles represent tracker hits. Red rectangles represent triggered OMs.

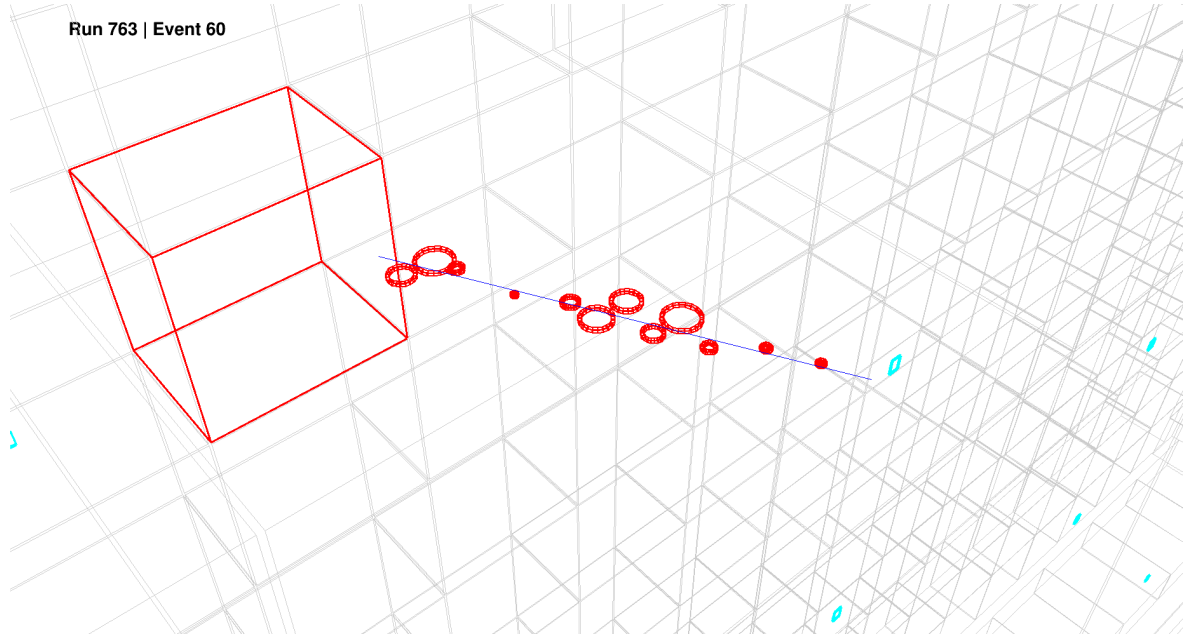


Figure 3.10: An example of a reconstructed electron trajectory. Red circles represent radii measured by tracker cells, the red box represents triggered OM, light blue rectangles represent calibration sources and the blue line is the reconstructed trajectory. The figure was adapted from Ref. [42].

3.3.2.1 Track reconstruction

Data in the RED format only give us an information about which tracker cells were triggered and about the signal which they measured. On a basic level, we could only check which tracker cells were triggered and based on this information decide which events to keep. This method, however, completely ignores any information about the vertical coordinate of the trajectory and even in the horizontal plane it is very imprecise.

The power of the tracker is in the fact that it allows us to very precisely reconstruct the whole trajectory of the particle. First, a drift model is applied to find in which height and how far from the wire the particle has passed. We can represent the information obtained by each tracker cell with a circle in given height. The second step is to fit these circles with a straight line (figure 3.10). This is done by a tracking algorithm. For simulated data, the tracking algorithm implemented in Falaise can be used. This algorithm, however, has not been converted to work with real data. Because of that, we use a different algorithm (currently in development) for both simulated and real data throughout the whole thesis [42]. Based on the reconstructed line, we find two vertices. The first one is the intersection of the line with the source foil plane, and the second line is the intersection with an OM front face.

3.3.2.2 Cut conditions

The goal is to design data cuts which would discard as many background events as possible while keeping most of the good ^{207}Bi events. The main two criteria we want to verify is whether the first vertex lies close to a calibration source and whether the second vertex lies on a front face of a triggered OM (like in the figure 3.11). In order to do this, we need to know exact positions of the sources and the OMs. This might seem trivial, as we know the dimensions of detector parts, but it is important

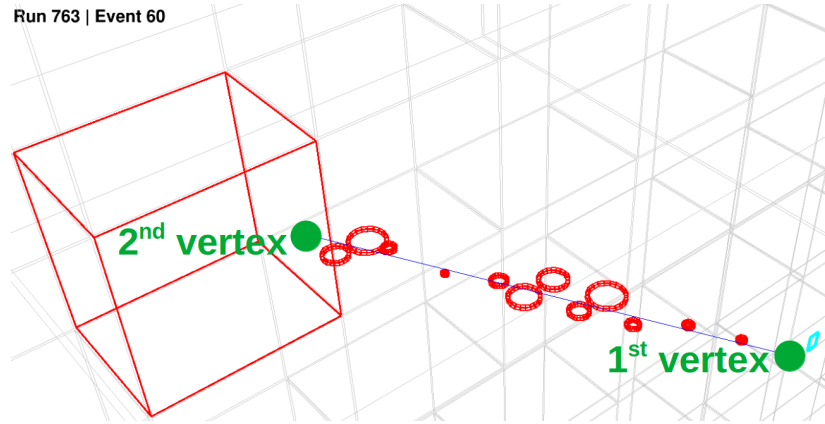


Figure 3.11: An example of a calibration event which would pass data cuts. The first vertex lies close to a calibration source (light blue rectangle) and the second vertex lies on a front face of a triggered OM (red rectangle).

to verify these values based on data. It is also important to understand that for the purpose of cuts, we do not really need to know the absolute dimensions of the detector parts. We only need to know where the tracker “sees” them. What we need to extract are some apparent positions which depend on the track reconstruction itself, not the real dimensions of the detector. If the reconstruction method changes, we might get different apparent positions, but this would not affect the cuts.

To find the calibration source positions, we use a cumulative histogram of positions of the first vertex (figure 3.12). We can see that hot spots form around calibration sources, as the most tracks come from these positions. To extract the source positions, we simply find the maximum bin in each hot spot, and we take its centre as the calibration source positions. A more precise statistical method for calibration source position extraction has already been developed [43] and work in this area of calibration source position is still ongoing. Once the development would be over, this version will be used in the final version of the calibration software. For the purpose of this work, the simple maximum finding method is sufficient.

When we have the source positions, we also need to state how far from these positions the vertex can be to be accepted. In table 3.2 we can see standard deviations of vertex positions around individual sources in y and z coordinates. Here we use a convention where y and z coordinates are parallel to the source foil, z being vertical. The x -axis is then perpendicular to the source foil. We also choose origin in the middle of the detector (figure 3.13a). This convention is used through the whole thesis. For the cut, we require that the vertex lies inside an elliptical area around the source (figure 3.14a). Semi-axes of these ellipses were chosen as 3σ based on values from 3.2. As the values are only for the first two columns of sources, we take their averages for the other sources.

In the second criterion, we need to check if the second vertex lies on a triggered OM. Again, we first need to extract apparent positions of OMs. As in the previous case, we use cumulative histograms. This time, we construct a separate histogram for each OM. Each histogram contains second vertex positions from all events where the given OM was triggered. The second vertices were found as an intersection of the track and a plane at either $x = -435$ mm or $x = 435$ mm (figure 3.13b). We can see an example of such histogram in the figure 3.12. The vertices are generally clustered inside a

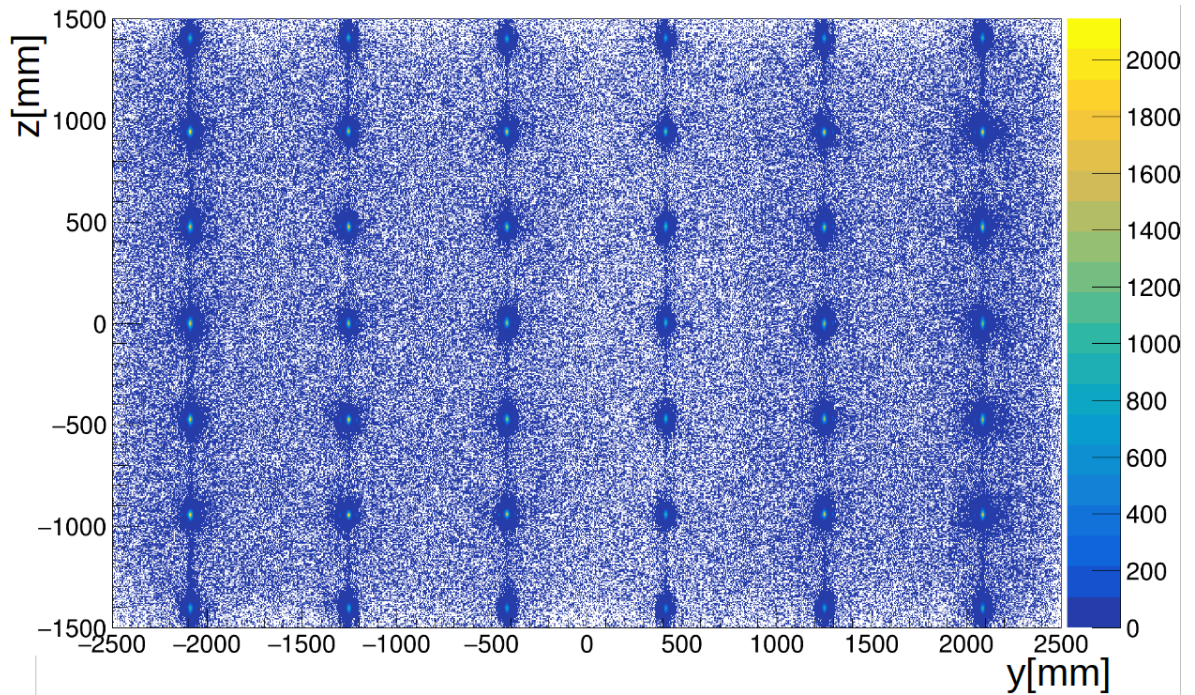


Figure 3.12: A cumulative histogram of track vertices lying in the source foil plane. We can see hot spots around calibration sources, which most of the tracks come from.

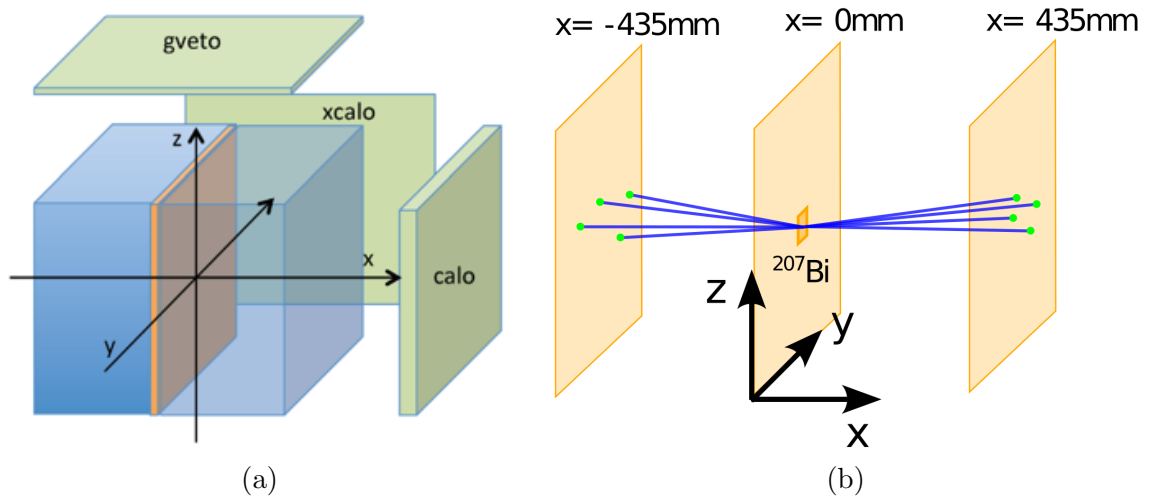


Figure 3.13: a) The SuperNEMO coordinate system used throughout the whole thesis. The origin is in the middle of the detector, y and z axes are parallel to the source foil and x -axis is perpendicular. Courtesy of the SuperNEMO collaboration. b) The second vertex of a track (green) is found as an intersection of the track and a plane at either $x = -435$ mm or $x = 435$ mm. The middle of the coordinate basis was moved compared to (a) for better clarity of the image.

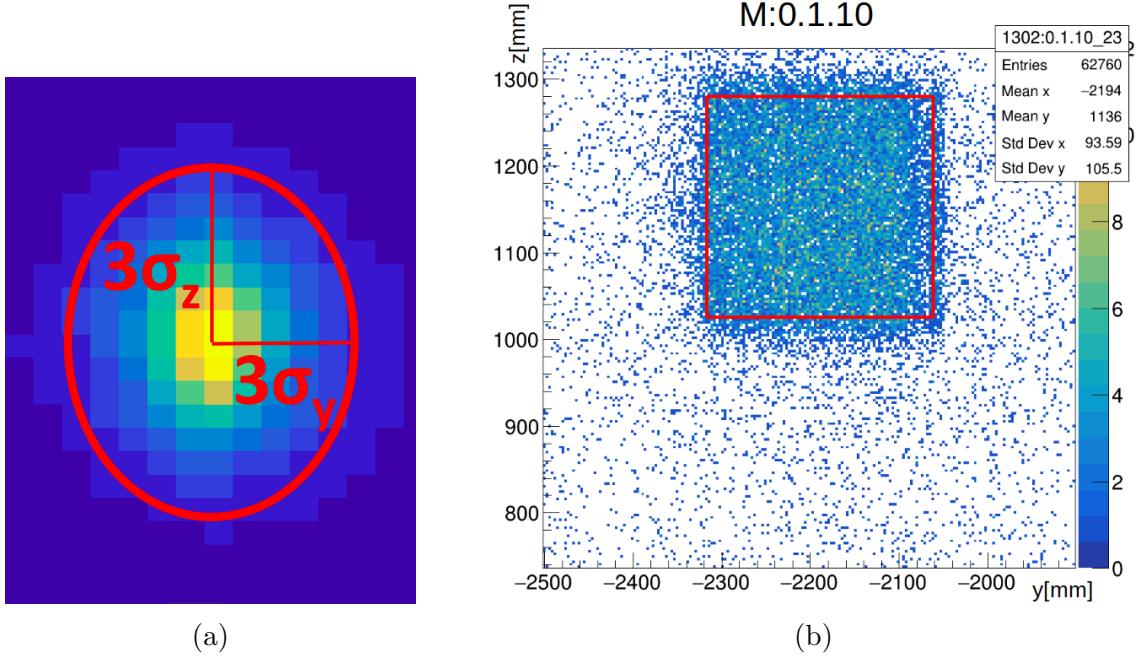


Figure 3.14: a) For the calibration source cut, we only accept vertices which lie inside an ellipse around the calibration source. b) A cumulative histogram of the second track vertices from events where one chosen OM was triggered. We can see that most of the vertices lie inside a box. The red box represents the apparent position of the OM.

rectangle. If the track and vertex reconstruction would perfectly correspond to reality, the rectangle should become a square sized 256×256 mm. The track reconstruction, however, depends on values such as effective anode length or x-position of the OM front face. These are only known with certain level of uncertainty. Fortunately, the uncertainties are not as significant, and we can still consider the vertices to be clustered inside a 256×256 mm square within a reasonable level of precision. To find the apparent position of each OM, we can find a 256×256 mm sized box containing the highest number of counts in the histogram. The position of this box is the apparent position of the OM front face (red box in the figure 3.14b). Now, for the vertex to be accepted, we require that it lies inside this box.

Besides checking the vertex positions, we also add two less significant criteria. The

1st column			2nd column		
Row	σ_y [mm]	σ_z [mm]	Row	σ_y [mm]	σ_z [mm]
1	8.3	10.3	1	8.3	10.4
2	8.3	9.9	2	8.4	9.5
3	8.1	10.1	3	8.4	9.9
4	8.2	10.2	4	8.4	10.3
5	8.2	10.0	5	8.3	10.1
6	8.2	9.8	6	8.4	9.8
7	8.2	10.1	7	8.3	10.4

Table 3.2: A table of vertex position standard deviations around individual calibration sources in the first two columns. We can see that the standard deviation is higher in the z-coordinate. The values were taken from [43].

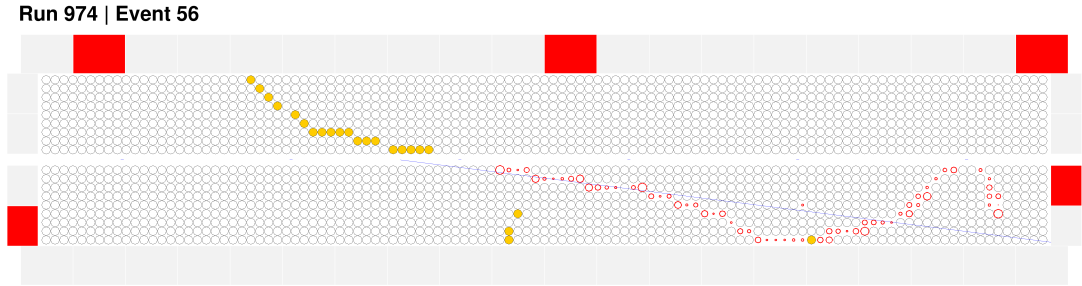


Figure 3.15: An example of a chaotic calibration event. Such events are excluded by the data cut checking for number of triggered tracker cells.

first one checks if the number of triggered tracker cells inside a time window from -0.2 to $5 \mu s$ relatively to the OM trigger time is lower than 16. This filters out chaotic events with long trajectories, which could potentially bring more uncertainty to the results. An example of such event can be seen in the figure 3.15. The choice of the time interval was based on the fact, that most tracker hits fall into this interval. The negative value of -0.2 was used because some tracker hits are assigned a negative time due to delay caused by cable length. The second criterion checks that there are at least 4 tracker hits in an area near the calibration source. For that, we check a rectangular area sized 242×220 mm ($=11 \times 10$ tracker cell radii). This can be seen in the figure 3.16. This condition filters out events where the electron could originate from a Compton scattering in the middle of the tracker. If such an electron went in the right direction, it could fake a track coming from a calibration source.

To summarize, for the event to be accepted it has to pass four conditions:

1. The first vertex lies inside an ellipse around a calibration source.
2. The second vertex lies on the front face of a triggered OM.
3. The number of triggered tracker cells inside a small time window is lower than 16.
4. There are at least 4 triggered tracker cells close to the calibration source.

If any of these conditions is not met, the event is discarded.

3.3.3 Calibration spectra

As stated in the chapter 2, the calibration of individual OMs will be performed using measured energy spectra of ^{207}Bi electrons. We applied the data cuts described in the previous section on both the background data and the calibration data to find out how many background events we can expect in energy spectra of OMs. For the background data, we get on average 0.56 events per hour per OM, while for the calibration data we get 901 events per hour per OM. This shows that the background is very efficiently reduced by the data cuts.

In the figure 3.17 we can see an example of an energy spectrum measured by a single OM compared to its background. We can see two peaks corresponding to the energies of electrons from the internal conversion of ^{207}Bi . Notice that the x-axis is

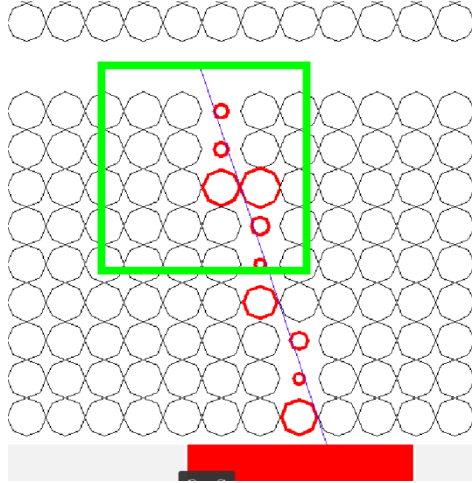


Figure 3.16: A visualization of the data cut for number of triggered tracker cell near a calibration source. For this event, we check the number of triggered tracker cells inside the green box. This number has to be at least 4 to pass the cut.

in units of charge, as we yet do not know the calibration parameters to transform the charge into energy. Each of the peaks actually consists of three discrete energies merged together. These are the energies of electrons from the K, L and M shells. In the figure 3.18 we can see the theoretical spectrum simulated by Falaise for comparison. In the table 3.3 we can see intensities of individual peaks in the theoretical spectrum. We will sometimes refer to the first peak as the 482 keV peak and to the second peak as the 976 keV peak, referring to the energies of K-shell electrons. We could potentially observe a third 1682 keV peak, but its intensity is very low so it is hardly recognizable in spectra of individual OMs. However, it is possible to observe it when combining data from all OMs.

I_{482}	I_{555}	I_{567}	I_{976}	I_{1049}	I_{1061}	I_{1682}	I_{1755}	I_{1767}
1,52%	0,44%	0,15%	7,03%	1,84%	0,54%	0,026%	0,004%	0,001%

Table 3.3: Intensities of ^{207}Bi internal conversion electron energies.

3.3.3.1 Gain correction

The gain of a photomultiplier measures its ability to amplify the received signal. In context of OM calibration, the gain determines the amount of charge measured by the OM after deposition of certain amount of energy in the scintillator. The gain of OMs can change with time. These changes cause that charge spectra measured in different times differ by a scaling factor. This can be seen in the figure 3.19. The spectra were measured by the same OM but with an eight-day time gap. For most OMs the difference is not as significant, but it is important to deal with the gain variation in some way, as it can artificially widen the peaks or even deform the spectrum in a way which makes it impossible to properly fit it.

Let us assume that we have data from N calibration measurement runs. For each OM, we can correct the gain in the following way. We fit the 976 keV peak in each run's spectrum measured by given OM by a sum of three Normal distributions. The fitting process will be described in more detail in the chapter 4. At this point, it is

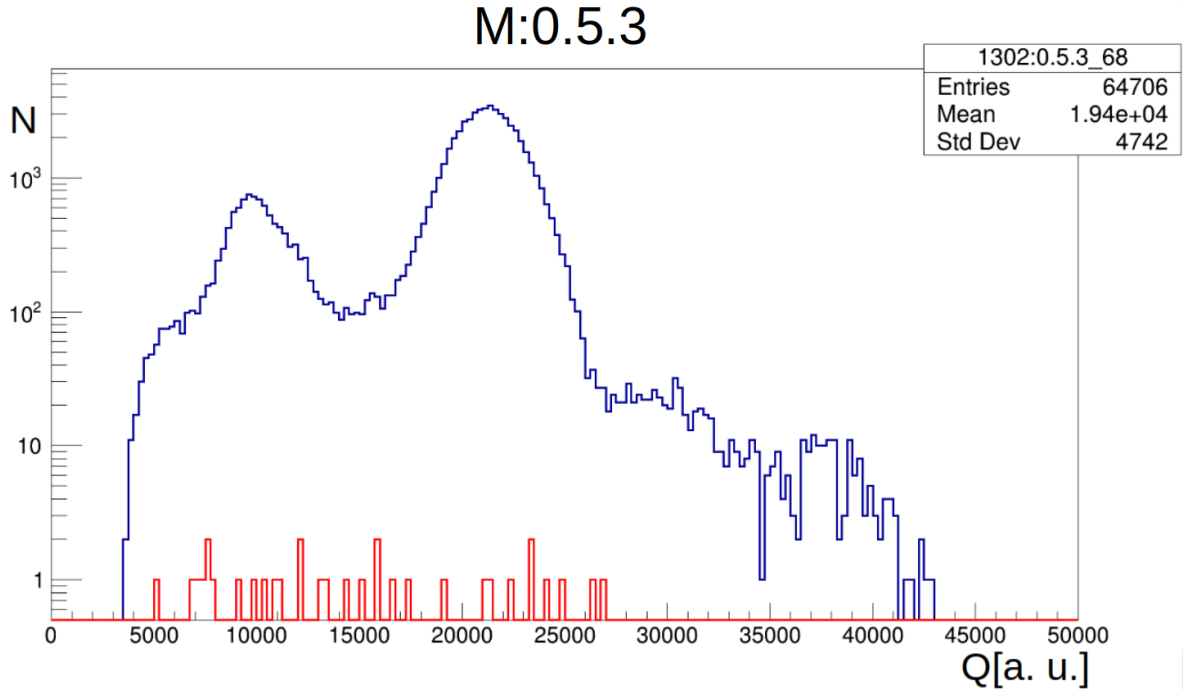


Figure 3.17: An example of the ^{207}Bi spectrum (blue) measured by a single OM (M:0.5.3) compared to background (red) measured by the same module. The ^{207}Bi spectrum comes from the 17 calibration runs (~ 51 h of measurement) from table 3.1 and the background spectrum comes from the 5 background runs (~ 50 h of measurement). We can see two peaks corresponding to the energies of ^{207}Bi electrons.

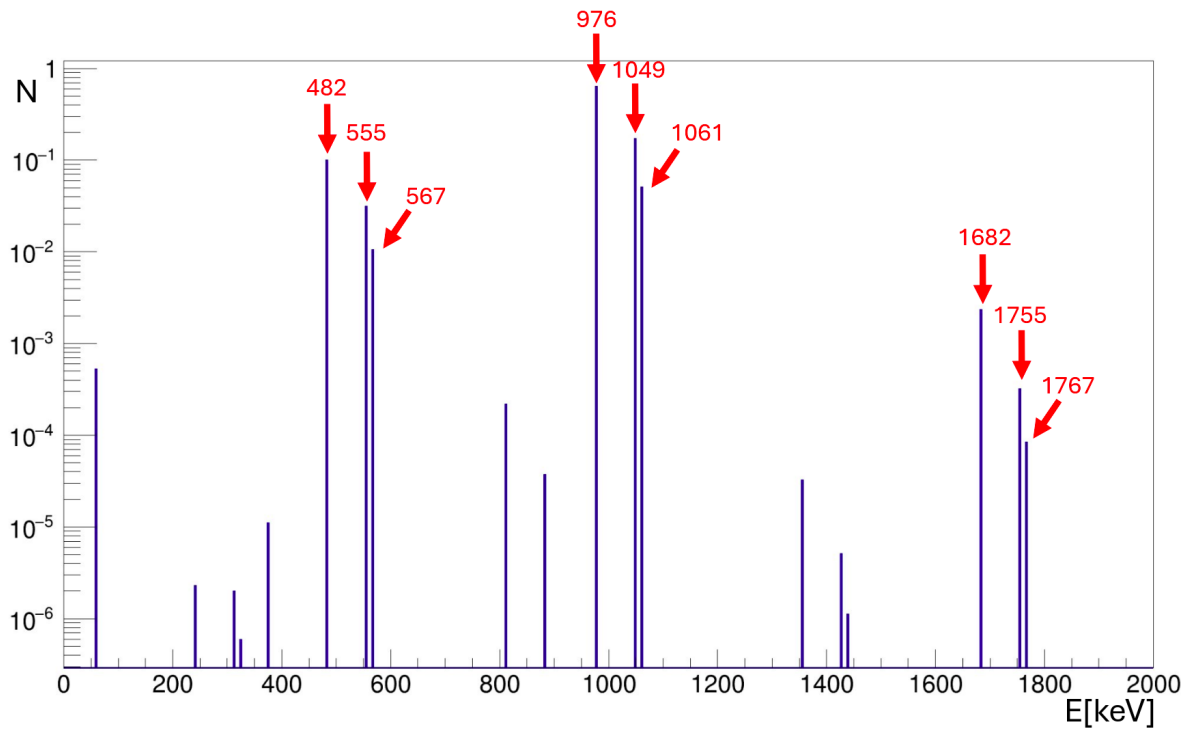


Figure 3.18: The theoretical ^{207}Bi electron spectrum simulated by Falaise. We can see three groups each containing three peaks corresponding to K, L and M shells. The intensities of individual energies can be found in the table 3.3.

Gain variation

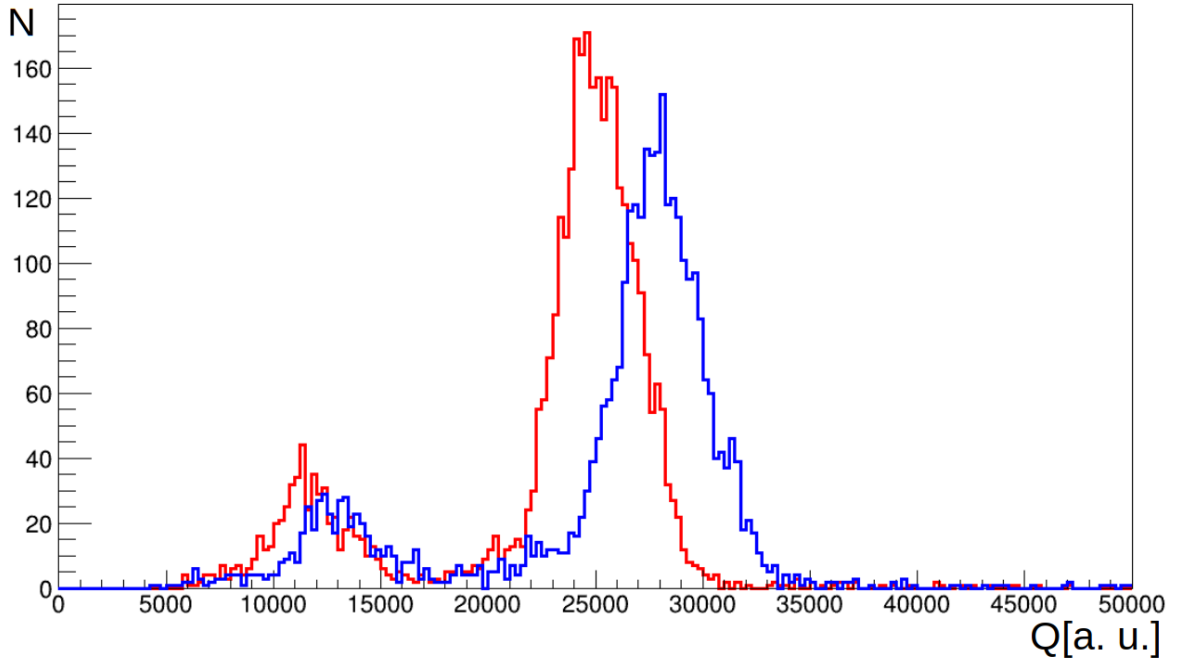


Figure 3.19: A comparison of two charge spectra measured by the same OM (M:0.8.8). The red spectrum (run 1086) was measured 8 days after the blue one (run 1133). We can clearly see that the spectra differ by a scaling factor. This is caused by variation in gain of the photomultiplier.

only important that from the fits we extract positions of the 976 keV peak in each run. Let us call these $\mu_1, \mu_2 \dots \mu_N$. From these positions we then calculate the correction factor for each run

$$K_j = \frac{\frac{1}{N} \sum_{i=1}^N \mu_i}{\mu_j}, \quad (3.1)$$

where j is the index of the given run. Finally, in each run, we iterate through all measured charges and calculate corrected charges as

$$Q_{corr} = K_j Q, \quad (3.2)$$

where Q is the original charge. In the figure 3.20, we can see a comparison of spectra measured by an OM with bad gain variation. The first spectrum is before application of the gain correction, and the second is after.

3.3.3.2 Calibration parameter calculation

Based on the measured spectra such as the one in the figure 3.17 we could already easily extract calibration parameters. We would first fit both of the peaks with a sum of three Gaussian functions. From the fits we would extract positions of the peaks. Let us call these Q_1 and Q_2 . We can assume that the relationship between energy and charge is linear $E = a_j Q + b_j$, where a_j and b_j are the calibration parameters we are trying to find and j identifies specific OM. Now, since we know that Q_1 and Q_2 correspond to the energies of 482 and 976 keV, we can simply find a_j and b_j by solving a system of two linear equations

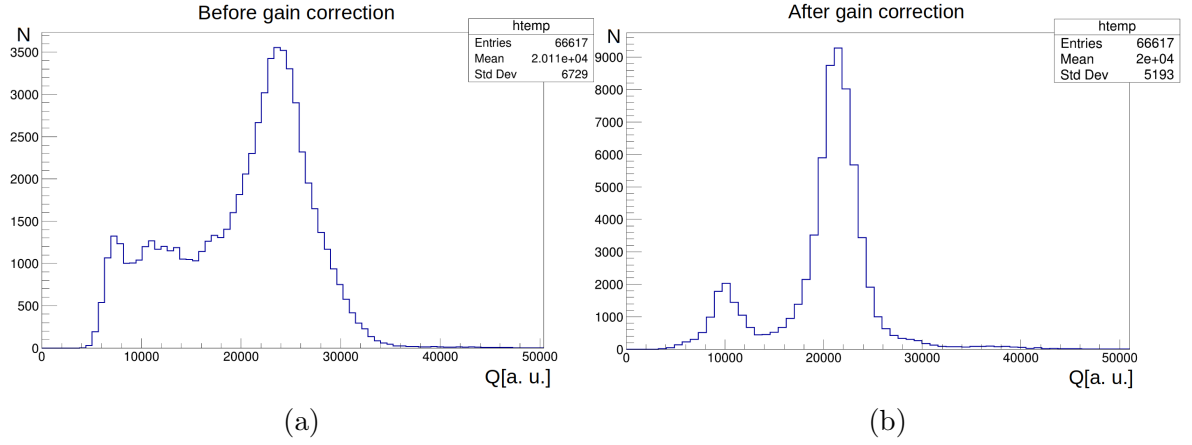


Figure 3.20: In the picture a), we can see a charge spectrum composed of data from 17 calibration runs 1086-1200 (table 3.1). In the picture b), we see the same spectrum after application of the gain correction.

$$E_1 = a_j Q_1 + b_j, \quad (3.3)$$

$$E_2 = a_j Q_2 + b_j, \quad (3.4)$$

where $E_1 = 482$ keV and $E_2 = 976$ keV.

Using this simple process, we could obtain a set of calibration parameters for each OM. The quality of calibration parameters obtained in this way would unfortunately be very insufficient. The reason for that is that this approach completely ignores significant effects which influence the measured energy spectrum. The nature of these effects and methods to correct them will be described in the following chapter.

Chapter 4

Energy corrections

Precise calibration of OMs requires us to account for certain physical effects which influence the measured ^{207}Bi electron energy spectrum. In the figure 4.1 we can see a scheme of a calibration event. We can see that the electron first passes through layers of matter, where it loses part of its energy. Then it reaches an OM, the response of which is also influenced by several phenomena. Finding suitable models of these effects which account for these corrections can potentially improve the energy resolution of the whole experiment. In the following sections, we will describe two groups of corrections: optical corrections and energy loss corrections.

4.1 Optical corrections

The optical corrections account for effects taking place in OMs themselves. These effects result in non-uniformity and non-linearity of OMs. By non-uniformity, we refer to the fact that the response of an OM depends on the point where a particle deposits its energy. For example, an electron hitting the OM in the corner results in a different signal than if an identical electron hit the centre. This dependency can be seen in the figure 4.2a, which depicts a multiplicative factor by which the measured energy differs from the deposited one. By non-linearity, we mean a deviation from the linear relationship between the measured charge and the particle's energy. Ideally, the response should be perfectly linear, although this is never the case. The optical corrections describing these effects have already been developed and implemented into Falaise by Arnaud Huber and Axel Pin [44][45] (in French).

4.1.1 Birks' law and Cherenkov radiation

The non-linearity of an OM is its deviation from the linear relationship between measured charge and energy deposited by a particle. The non-linearity of OMs is influenced by two effects: Birks' law and Cherenkov radiation. The non-linearity effect described by the Birks' law comes from the fact that part of the energy deposited by the particle results in ionization of molecules instead of scintillation light generation. The Birks' law describes light yield of a particle passing through a scintillator as a function of energy loss per path. It has a form [46]:

$$\frac{dS}{dx} = \frac{A \frac{dE}{dx}}{1 + k_B \frac{dE}{dx}}, \quad (4.1)$$

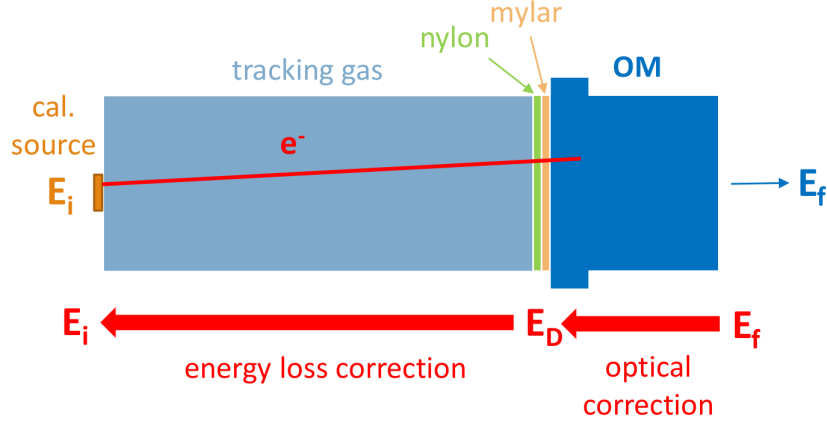


Figure 4.1: A scheme of an event from calibration measurement. Our goal is to estimate the initial energy E_i from the measured energy E_f by application of the optical corrections and the energy loss corrections.

where $\frac{dS}{dx}$ is light yield per path length, $\frac{dE}{dx}$ is energy loss per path length and A and k_B are constants specific for material of the scintillator and type of the particle. From the equation (4.1) we can see this effect is more significant for high $\frac{dE}{dx}$ where $\frac{dS}{dx}$ saturates, while for low $\frac{dE}{dx}$ the relationship approaches linearity.

The second non-linearity effect is the Cherenkov radiation. Cherenkov radiation is emitted when the particle travels through a block of scintillator faster than the speed of light in a given material. This effect results in an additional non-linearity in the amount of light generated in the scintillator and needs to be taken into account in the calibration.

We can describe the non-linearity resulting from Birks' and Cherenkov effect by a single formula

$$E_f = \alpha E_{BC} + \beta (E_{BC})^\gamma, \quad (4.2)$$

where E_f is the energy observed by the OM, E_{BC} is the deposited energy cleaned of the Birks' and Cherenkov effect and α , β and γ are empirical constants. As γ is not an integer, this formula has to be solved numerically for E_{BC} . This can be done simply using a standard root finding method. The Newton-Raphson method has been used in this work. The method is described for example in [47].

4.1.2 Geometrical non-uniformity

When a particle deposits its energy inside the scintillator block, the emitted scintillation light scatters inside the scintillator block (figure 4.2b). How much of this light is collected by the PMT depends on the point of energy deposition. This results in the geometrical non-uniformity. This geometrical dependence cannot be described by a simple model, but has to be based on a simulation of the OM with given geometry and material properties. We represent the geometrical correction by a single multiplicative factor depending on the point of energy deposition $G(x, y, z)$. We then calculate the real deposited energy as

$$E_D = \frac{E_{BC}}{G(x, y, z)}. \quad (4.3)$$

Gammas penetrate deep into the scintillator, which is why we have to consider G as a function of all three coordinates. In contrast to that, the mean free path of

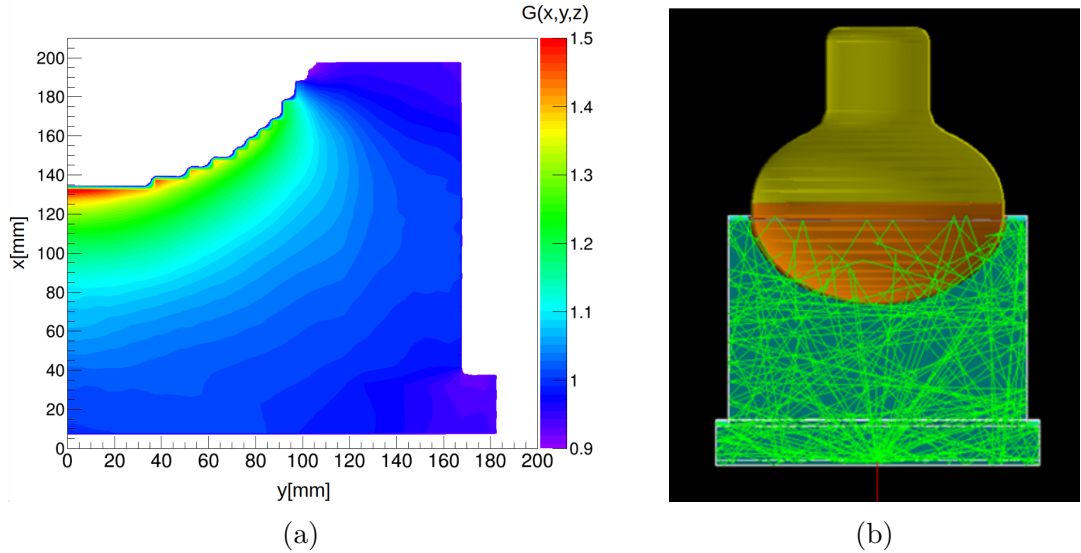


Figure 4.2: a) A slice through the 3D histogram of the geometrical correction multiplicative factor. b) A visualization of photon scattering inside the scintillator of an OM. The number of photons collected by the PMT depends on the point of energy deposition. This influences the resulting response of the OM. Both figures were adapted from Ref. [45] (in French).

electrons inside the plastic scintillator medium (polystyrene) is very short. Therefore, the electrons deposit all of their energy in a very small spot on the front face and do not penetrate into the OM. Thanks to this, we do not need to consider the depth x coordinate and G becomes a function of only y and z . The simulation of the geometrical non-uniformity has been done in the past by Arnaud Huber [45] (in French). Values of the G factor were saved as a 3D histogram. A slice through this histogram can be seen in the figure 4.2a. Using this 3D histogram in the Falaise software would be very memory expensive, which is why there was a desire to replace it with a model which would not be as memory demanding while not losing too much precision. This was done by fitting the histogram by a polynomial of the tenth order [44] (in French). This way we only need 286 coefficients instead of the whole histogram.

4.2 Energy loss corrections

The second group of energy corrections deals with energy losses of ^{207}Bi electrons. Electrons coming from the calibration sources have to pass through the tracker before they reach an OM. Because of this, they lose part of their energy in the tracking gas present in the tracker. Moreover, there is a Mylar foil on the front face of each OM which ensures better light collection, and also a nylon foil in front of main wall OMs which improves the gas tightness of the tracker. These foils also add to the energy losses of electrons.

In the figure 4.3 we can see that the measured spectrum (blue) is shifted to lower energies compared to the theoretical values (green dots) where they should have been, were it not for the energy losses. This shift also is not the same for the whole spectrum, but depends on energy. Less energetic electrons tend to lose more energy. Besides shifting the peaks, the energy losses also increase the width of the peaks. This worsens

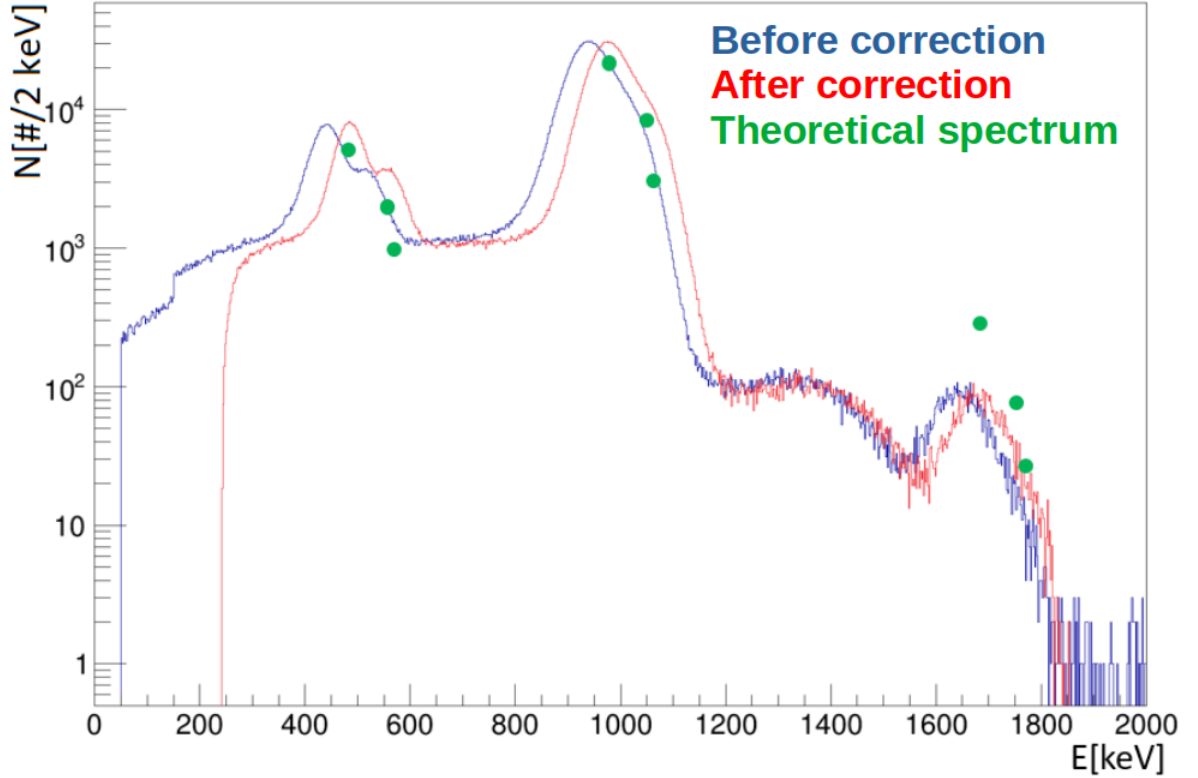


Figure 4.3: A comparison of a ^{207}Bi spectrum before and after applying a correction based on the phenomenological energy loss model. We can see that after the correction, the peaks moved much closer to the theoretical energies. The figure was adapted from Ref. [48] (in Czech).

the energy resolution of the whole detector. Thanks to the tracker, we have very precise information about trajectories of electrons. The idea is that we leverage this information to estimate lost energy of each electron and add it to the measured one. This can decrease the effect of energy losses to the energy resolution.

4.2.1 Phenomenological model

In the previous work, a phenomenological model of energy losses has been developed [48] (in Czech). It was assumed that the energy lost along the trajectory depends on the length of the trajectory d and on the electron's energy E . The model was based purely on simulated data. A simulation of $5 \cdot 10^7$ electron events has been used (each containing one electron). These electrons had uniform energy resolution from 50 to 2000 keV and were emitted from calibration sources (figure 2.8b). A result of this simulation can be seen in the figure 4.4a. The plot depicts the dependence of the lost energy on d and E . Each point represents an average energy loss ΔE for a given d and E . Lost energy of individual electrons was calculated as $\Delta E = E_i - E_f$, where E_i is the initial energy and E_f is the energy deposited in an OM.

From the simulated data, it was observed that the dependence of ΔE on d (for fixed E) is linear and the dependence of ΔE on E is approximately exponential. Based on these observations, the following model has been proposed

$$\Delta E(d, E) = (p_1 d + p_2) e^{p_3 E} + p_4 d + p_5, \quad (4.4)$$

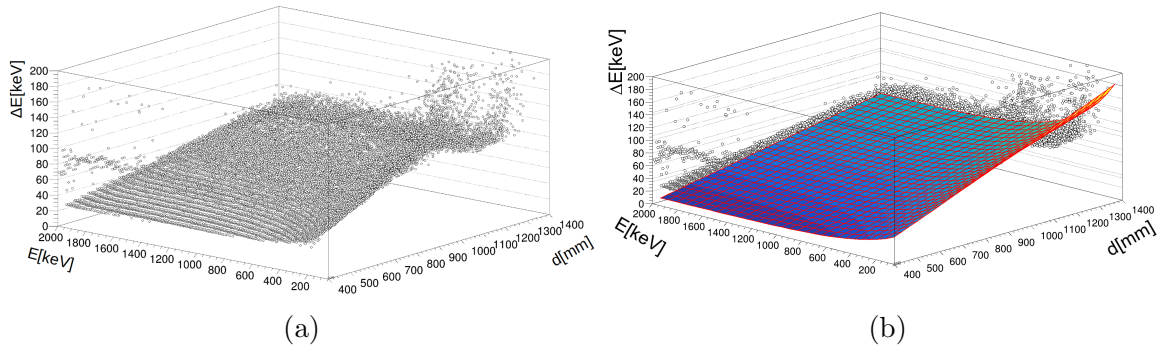


Figure 4.4: a) A dependence of the lost energy on the length of the trajectory d and electron's energy E extracted from simulated data. Each of the points represents an average loss ΔE for a given E and d . b) A fit of the simulated data using the phenomenological model (4.4).

where p_1 to p_5 are fitting parameters. We can see that the function combines the linear relationship in one variable and the exponential one in the other. The simulated data were fitted using this model. The result can be seen in the figure 4.4b.

The proposed phenomenological model fits the simulated data well. It has been also applied on the simulated ^{207}Bi spectrum, and it has been shown that the correction shifts the peaks back very close to the correct energies and that it lowers the FWHM of the peaks, improving the energy resolution. The effect of the energy spectrum can be seen in the figure 4.3. There are, however, a number of problems with this model.

The first problem is the high number of fitting parameters. With five fitting parameters, we could argue that the model simply overfits the simulated data, which is not ideal. Using a more sophisticated model, we could lower the number of fitting parameters, resulting in more robust correction. Moreover, the parameters do not have any physical interpretation. It would be better to have parameters which would be directly linked to the physical properties of the detector so that we could verify if the values we get are reasonable. The second problem is that the model considered energy losses in Mylar and nylon to be negligible, which is not the case. These losses added to the values of ΔE , so they influenced the values of fitting parameters. Because of that, we can say that they were included in some way. The problem is that the model does not treat them separately. Finally, this analysis has been done using the Falaise tracking algorithm and a simulation where the magnetic field was active. Real measurements have, however, so far been performed without the magnetic field and the measured data will be processed with a newer tracking algorithm. To check if these changes affect the resulting fit, we have replicated the previous analysis for the newer tracking algorithm and a simulation without the magnetic field. In the figure 4.5 we can see a comparison of fitting error for the new dataset and the original one. We can see that for the new dataset, there are areas where the fitting error is significantly higher. It seems that the phenomenological model no longer provides description as good as in the previous analysis.

4.2.2 Physics based model

The shortcomings of the phenomenological energy loss model lead us to the conclusion that we need to replace it with a new one. The goal is to find a model with lower

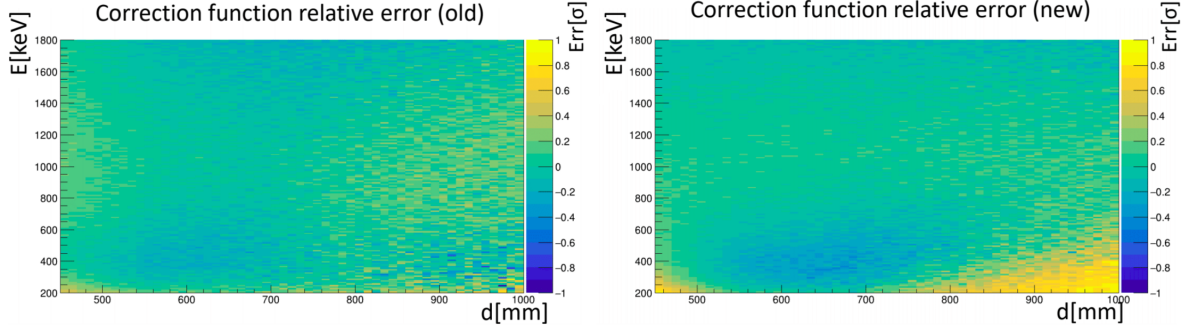


Figure 4.5: A comparison of fitting error obtained by fitting formula (4.4) to two different datasets. The new dataset differs from the old one in absence of magnetic field inside the detector and by using different tracking algorithm.

number of fitting parameters which would be based on physical theory.

4.2.2.1 Bethe-Bloch formula

For low energy electrons, such as those emitted by ^{207}Bi , the prevailing mechanism of energy losses is ionization of surrounding atoms. These energy losses can be described by the Bethe-Bloch formula. For electrons, the formula has the following form [49]

$$\frac{dE}{dx} = \frac{2\pi N_A \langle Z/A \rangle}{m_e c^2} \left(\frac{e^2}{4\pi\epsilon_0} \right)^2 \frac{\rho}{\beta^2} \Phi(E), \quad (4.5)$$

where N_A is the Avogadro constant, $\langle Z/A \rangle$ is the average of ratios of atomic numbers and atomic masses weighted by fraction masses of gas components, m_e is the rest mass of electron, e is the elementary charge, ϵ_0 is the permittivity of vacuum, ρ is density of the material, I is mean excitation energy of the gas, E is energy of the electron, dE/dx is the mean energy loss per unit of length (stopping power) and

$$\beta = \frac{v}{c} = \frac{2m_0 c^2 E_k + E_k^2}{(m_0 c^2 + E_k^2)^2} \quad (4.6)$$

is the relativistic factor. $\Phi(E)$ is an energy dependent term of form

$$\Phi(E) = \ln \frac{m_e c^2 \beta^2 E}{2I^2 (1 - \beta^2)} - \left(2\sqrt{1 - \beta^2} - 1 + \beta^2 \right) \ln 2 + 1 - \beta^2 + \frac{1}{8} \left(1 - \sqrt{1 - \beta^2} \right)^2. \quad (4.7)$$

4.2.2.2 Calculating energy losses of electrons

There are several concerns regarding the calculation of energy loss using equation (4.5). First, there are three material specific constants, the value of which we need to specify. These are $\langle Z/A \rangle$, ρ and I . For Mylar and nylon, these are tabular values. We can find them in the table 4.1. For the tracking gas, the situation is more complicated because we need to calculate the constants based on its composition. $\langle Z/A \rangle$ is simply a weighted average of Z/A ratios of all elements contained in the gas,

$$\langle Z/A \rangle = \sum_i \frac{w_i Z_i}{A_i}, \quad (4.8)$$

	$\langle Z/A \rangle$	$\rho[\text{g/cm}^3]$	$I[\text{keV}]$
Mylar	0.517964	1.4	0.0787
nylon	0.547912	1.14	0.0639

Table 4.1: Constants used in the Bethe-Bloch formula for Mylar and nylon. $\langle Z/A \rangle$ was calculated using formula (4.8). ρ and I were taken from [50].

Element	w	Z	A[g/mol]	I[eV]	Gas component	ω	M[g/mol]
He	0.629058	2	4.0026	41.8	He	0.95	4.0026
Ar	0.040018	18	39.948	188	Ar	0.01	12.011
H	0.158962	1	1.0078	19.2	Ethanol	0.04	15.999
C	0.105874	6	12.011	78			
O	0.066088	8	15.999	95			

Table 4.2: Table constants used in equations (4.8), (4.9) and (4.11). I was taken from [50].

where w_i are mass fractions of elements of the tracking gas. For the mean excitation energy I we use formula

$$I = \exp \frac{\sum_i w_i \frac{Z_i}{A_i} \ln I_i}{\langle Z/A \rangle}, \quad (4.9)$$

where I_i are excitation energies of tracking gas elements. The tracking gas consists of helium, argon, and ethanol, giving us 5 different elements. Values for these elements, which were used in equations (4.8) and (4.9) can be found in the table 4.2.

The property of the tracking gas which is measured is its pressure, not the density, appearing in the Bethe-Bloch formula. Assuming that the tracking gas follows the ideal gas equation, we can express the density as

$$\rho = \frac{M_m p}{RT}, \quad (4.10)$$

where R is the molar gas constant, $T \approx 298$ K is temperature of the tracking gas and M_m is molar mass of the tracking gas. We calculate M_m as weighted average of molar masses of gas components,

$$M_m = \omega_{He} M_{He} + \omega_{Ar} M_{Ar} + \omega_{Et} M_{Et}. \quad (4.11)$$

The values used in this formula can be found in the table 4.2.

From the equation (4.5) we can see that the stopping power $\frac{dE}{dx}$ depends on the energy of the electron. This means that to calculate the energy ΔE lost along the trajectory, we need to integrate the formula. This gives us an equation

$$\int_{E_2}^{E_1} \frac{\beta}{\Phi(E)} dE = \frac{2\pi N_A \langle Z/A \rangle}{m_e c^2} \left(\frac{e^2}{4\pi\epsilon_0} \right)^2 \rho d, \quad (4.12)$$

where E_1 is the initial energy, E_2 is the final energy, $\Delta E = E_1 - E_2$ and d is the length of the trajectory. The integral on the left side is complicated and cannot be solved analytically. Luckily, it turns out that for reasonably small ΔE the changes of the integrand along the integration interval are very small. Thanks to this, we can

Energy loss calculation comparison

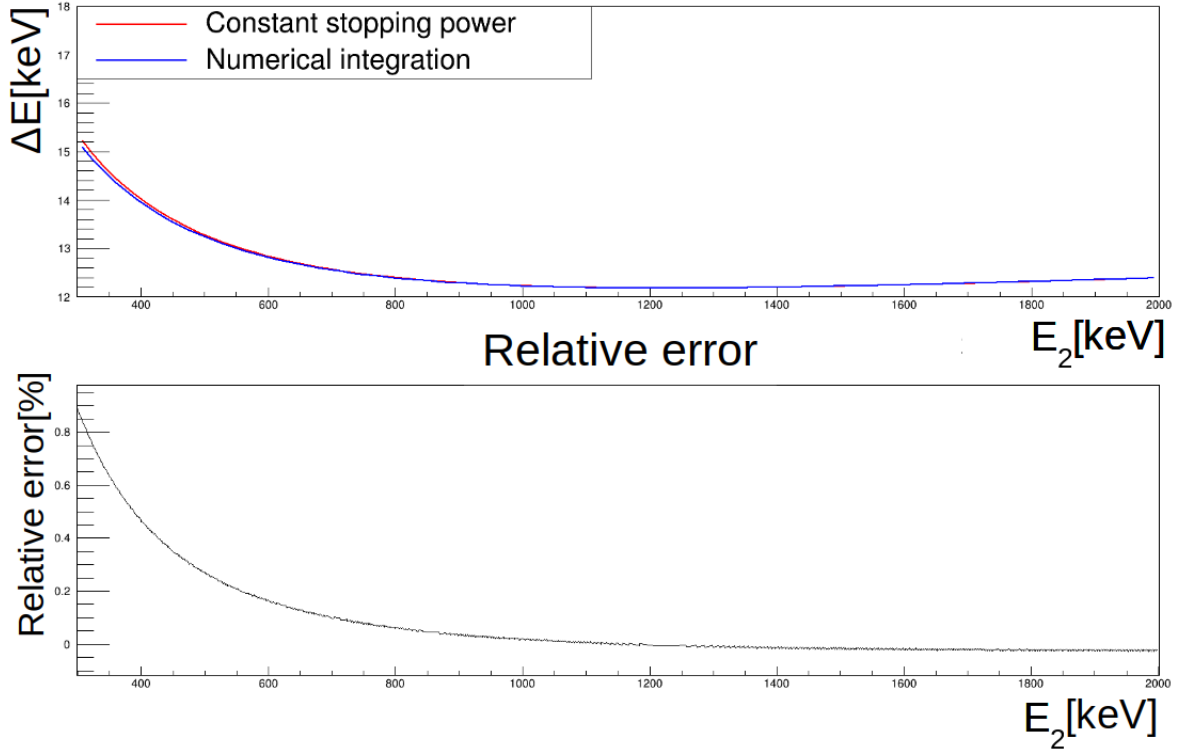


Figure 4.6: Energy losses of electrons passing through 50 μm of Mylar. We can see that the relative error of the calculation with constant stopping power is lower than 1% when compared to numerical integration of the equation (4.5).

consider $\beta^2/\Phi(E)$ to be approximately constant. This allows us to calculate the lost energy simply as

$$\Delta E(d, E) = \frac{dE}{dx}(E_2) d. \quad (4.13)$$

The phenomenological model used the same assumption of linear dependence of ΔE on d , but it arrived to it through a data driven approach, while here we have derived it ab initio. In the figure 4.6 we can see a comparison between the energy loss calculated using numerical integration of the equation (4.12) and the energy loss calculated with constant stopping power. The values were calculated for electrons passing through 50 μm of Mylar. We can see that the error of the constant stopping power approximation is lower than 1%.

4.3 Application of energy corrections

Let us assume that an OM measures electron energy E_f . This energy is influenced by the effects described in the previous sections. In the case of unknown initial energy E_i (such as in double beta decay measurement) we could estimate it by applying energy corrections on E_f . For the calibration data, we know the initial energies of ^{207}Bi electrons, but to unify the approach, we will still calculate the estimate of initial energy from E_f . In the figure 4.1 we can see a scheme of a calibration event. We can see that from E_f we go backwards and apply the corrections for the individual effects one by one. We first apply the optical corrections (section 4.1) which gives us energy

E_D as

$$E_D(E_f, y, z) = \frac{E_{BC}(E_f)}{G(y, z)}, \quad (4.14)$$

where E_{BC} is the energy calculated directly from E_f by application of the corrections for Birks' and Cherenkov effect and $G(y, z)$ is the geometrical correction factor. E_D is an estimate of the actual energy deposited in the OM (cleaned of the optical effects). From E_D we calculate an estimate of E_i by application of the energy loss corrections (4.2)

$$\begin{aligned} E_i(E_D, d_M, d_n, d_g; p) = & E_D && \text{(deposited energy)} \\ & + \Delta E_M(d_M, E_D) && \text{(loss in Mylar)} \\ & + \Delta E_n(d_n, E_D + \Delta E_M) && \text{(loss in nylon)} \\ & + \Delta E_g(d_g, E_D + \Delta E_M + \Delta E_n; p) && \text{(loss in the gas),} \end{aligned}$$

where ΔE_M , ΔE_n and ΔE_g are energy losses in Mylar, nylon and gas respectively, and d_M , d_n and d_g are distances passed through Mylar, nylon and gas respectively. In this formula, there are several important things to mention. First, the only parameter which we state explicitly is the tracking gas pressure. The reason for that is that it will be used as a fitting parameter later on. The other parameters from the Bethe-Bloch formula are considered to be known constants, and we do not include them for clarity. Second, we can see that the energy lost in each layer is calculated using energy at the end of this layer instead of the energy deposited in the OM. For example, ΔE_n is calculated based on $E_D + \Delta E_M$ instead of only E_D . This difference is very small, and simply using E_D in all functions would not result in too much error. As we saw in the figure 4.6 the stopping power changes very little with small changes of energy. This subtlety, however, does not add any complexity to the calculation. Finally, each of the energy loss functions depends on the distance passed through a given material. The distinction between the distances is important for curved trajectories. For straight trajectories (which we expect since the magnetic field is not active) these distances are linearly dependent, and we can replace them using a single variable. This can be seen in the figure 4.7. We can see that we can calculate the values d_M , d_n and d_g from thicknesses of the layers and the angle θ between the track and the source foil plane using a simple formula

$$d = \frac{L}{\cos \theta}, \quad (4.15)$$

where L is the thickness of a given layer. In our case, we will use values $L_M = 12 \mu\text{m}$, $L_n = 25 \mu\text{m}$ and $L_g = 435 \text{ mm}$ for Mylar, nylon and gas respectively. To summarize, the final formula to estimate E_i from E_f is

$$\begin{aligned} E_i(E_f, \theta, y, z; p) = & \frac{E_{BC}(E_f)}{G(y, z)} && \text{(deposited energy)} \\ & + \Delta E_M \left(\theta, \frac{E_{BC}(E_f)}{G(y, z)} \right) && \text{(loss in Mylar)} \\ & + \Delta E_n \left(\theta, \frac{E_{BC}(E_f)}{G(y, z)} + \Delta E_M \right) && \text{(loss in nylon)} \\ & + \Delta E_g \left(\theta, \frac{E_{BC}(E_f)}{G(y, z)} + \Delta E_M + \Delta E_n; p \right) && \text{(loss in the gas).} \end{aligned} \quad (4.16)$$

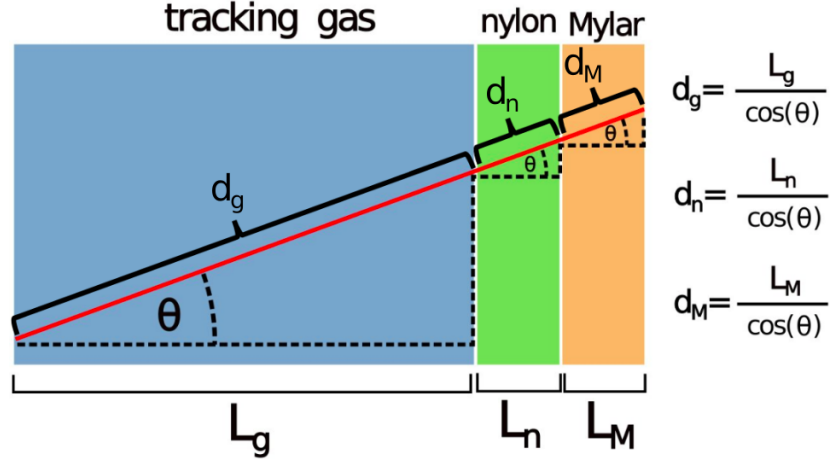


Figure 4.7: A track passing through layers of material. We can see that the distances passed through these layers can be calculated from the thickness of these layers and the angle θ between the track and the source foil plane.

4.3.1 Validation of the energy loss corrections using simulation

We have proposed a model where the only value which we consider to be a free parameter of the model is the pressure of the tracking gas. Notice that this is a big improvement compared to the phenomenological model, which used 5 free parameters (equation (4.4)). To validate whether the proposed model corresponds to the energy losses we observe, we need to find out which value of pressure we need to use to compensate the energy losses completely. We first attempt to find this value based on simulated data.

To validate the energy loss corrections, we use a dataset of 10^8 simulated ^{207}Bi calibration events. We first choose an arbitrary pressure p . Using this value of p , we calculate an estimate of initial energy E_i of each detected electron using the method described in the previous section. This way we get the global energy spectrum of electrons. Finally, if the energy loss corrections for chosen p compensate the energy losses exactly, the peaks in the global energy spectrum should be at the theoretical energies (482, 976 and 1682 keV). To find positions of the peaks, we fit each of them using a sum of three normal distributions

$$f_j(E; N_{jk}, \mu_{jk}, \sigma_{jk}, C_j) = \sum_{k=1}^3 N_{jk} N(E_i; \mu_{jk}, \sigma_{jk}) + C_j, \quad (4.17)$$

where $N(E_i; \mu_{jk}, \sigma_{jk})$ is a normal distribution with mean μ_{jk} and standard deviation σ_{jk} , N_{jk} are normalization constants, C_j is an additional constant, $j \in \{1, 2, 3\}$ is an index of the peak and k denotes an energy line in a given peak (K, L or M shell). The function (4.17) has 10 fitting parameters. From the theoretical spectrum (figure 3.18) we know ratios of N_{jk} , μ_{jk} and σ_{jk} . Thanks to this, we can express the parameters of the second and the third Gaussian in the sum using the parameters of the first one. The fitting function then gains the following form,

$$f_j(E_i; N_j, \mu_j, \sigma_j, C_j) = N_j G(E_i; \mu_j, \sigma_j) + \sum_{k=2}^3 n_k N_k G(E_i; k_k \mu_k, s_k \sigma_k) + C_j, \quad (4.18)$$

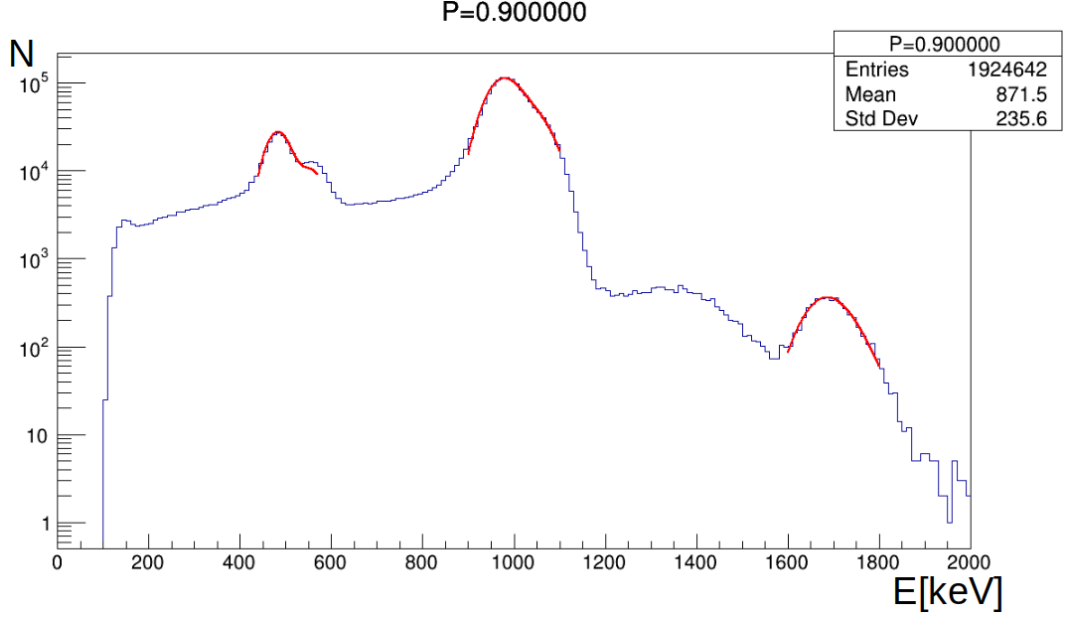


Figure 4.8: An example of a fit of the simulated global energy spectrum for pressure $p = 0.9$ bar. Each of the peaks is fitted with a sum of three normal distributions (equation (4.18)).

where n_j , k_j and s_j are ratios between the parameters. Their values are in the table 4.3. We will keep C_j as a free parameter only for the first peak, as it lies on a plateau behind the second peak. We will set it to zero for the other two peaks. This leaves us with 4 fitting parameters for the first peak, and with 3 for each of the other two peaks. The choice of the fitting function is described in more detail in Ref. [48] (in Czech). In figure 4.8, we can see an example of a fitted spectrum for $p = 0.9$ bar.

By repeating the process described above for different values of p , we find a p for which the peaks are closest to the correct energies. Using this method, we got $p = 0.921$ bar. To estimate the uncertainty of this value, we used bootstrapping, randomly sampling 10% of the original dataset in each iteration. The distribution of p values after 1000 iterations can be seen in the figure 4.9. We can see that the value of pressure including uncertainties is $p = (0.921 \pm 0.006)$ bar. The value of pressure used in Falaise is 0.89 bar. This value does not match the extracted value within uncertainty. There seems to be a small systematic error of the extracted value. Nevertheless, our model is able to determine the value of pressure with error of only 0.03 bar, which is a good confirmation of its reliability.

This way, we have verified that the energy loss model corresponds with the energy

	n_2	k_2	s_2	n_3	k_3	s_3	C_j
f_1	$\frac{I_{555}}{I_{482}}$	$\frac{555}{482}$	$\sqrt{\frac{555}{482}}$	$\frac{I_{567}}{I_{482}}$	$\frac{567}{482}$	$\sqrt{\frac{567}{482}}$	free parameter
f_2	$\frac{I_{1049}}{I_{976}}$	$\frac{1049}{976}$	$\sqrt{\frac{1049}{976}}$	$\frac{I_{1061}}{I_{976}}$	$\frac{1061}{976}$	$\sqrt{\frac{1061}{976}}$	0
f_3	$\frac{I_{1755}}{I_{1682}}$	$\frac{1755}{1682}$	$\sqrt{\frac{1755}{1682}}$	$\frac{I_{1767}}{I_{1682}}$	$\frac{1767}{1682}$	$\sqrt{\frac{1767}{1682}}$	0

Table 4.3: Table of coefficients used in fitting function (4.18). The C_j parameter is kept as a free one only for the first peak, as it lies on a plateau behind the second peak.

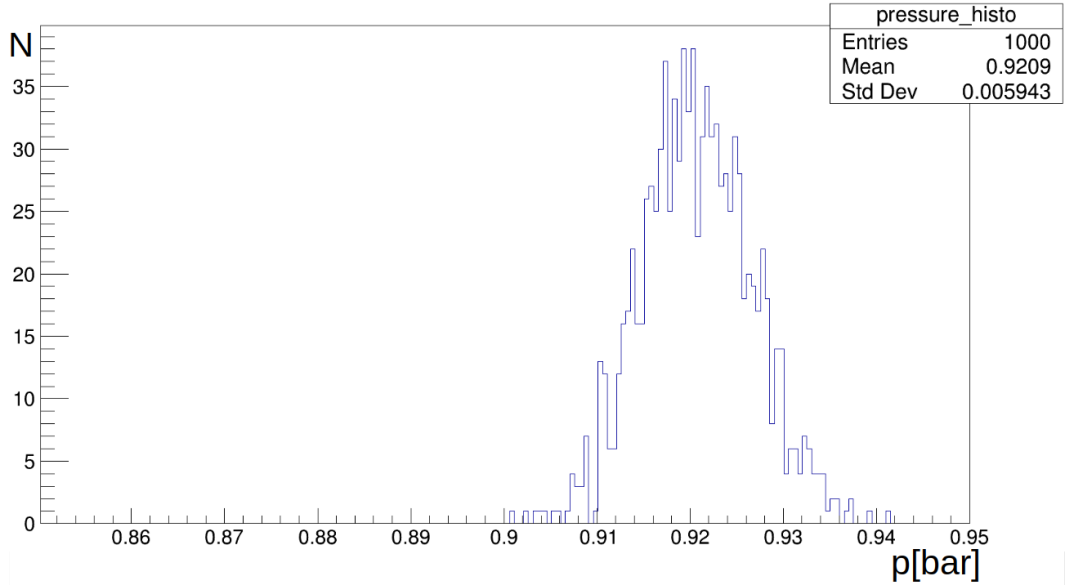


Figure 4.9: A distribution of pressures extracted in 1000 bootstrapping iterations. We can see that the value of pressure is $p = (0.921 \pm 0.006)$ bar.

losses produced by the simulation. Obviously, this is only a part of the story, as we mainly need to verify that the model corresponds with the real data. This, however, cannot be done by the same method. In the simulated data, we get the observed energy E_f right away, as if the OMs were already calibrated. In the real data, the observed quantity is charge Q and to apply the corrections we also need to find calibration parameters for each OM which transform Q into E_f . Instead of only having 1 fitting parameter being the tracking gas pressure, we will have $2N+1$ fitting parameters where N is the number of OMs. A method to extract these parameters from the calibration data will be described in the next chapter.

Chapter 5

Development of the calibration algorithm

We will again assume that the relationship between observed charge Q and energy E_f is

$$E_f = a_j Q + b_j, \quad (5.1)$$

where a_j and b_j are calibration parameters. The index j denotes a specific OM, as the parameters are unique for each OM. The observed energy E_f is influenced by the non-linearity and non-uniformity of the OM, as well as by the effect of energy losses (figure 4.1). These effects add more uncertainty to the measured spectrum. The idea of the energy corrections described in the chapter 4 is that we can use information from the tracker to partially reduce this additional uncertainty, resulting in more precise values of a_j and b_j . Substituting equation (5.1) into formula (4.16) we get

$$\begin{aligned} E_i(a_j, b_j, Q, \theta, x, y; p) &= \frac{E_{BC}(a_j Q + b_j)}{G(y, z)} && \text{(deposited energy)} \\ &+ \Delta E_M \left(\theta, \frac{E_{BC}(a_j Q + b_j)}{G(y, z)} \right) && \text{(loss in Mylar)} \\ &+ \Delta E_n \left(\theta, \frac{E_{BC}(a_j Q + b_j)}{G(y, z)} + \Delta E_M \right) && \text{(loss in nylon)} \\ &+ \Delta E_g \left(\theta, \frac{E_{BC}(a_j Q + b_j)}{G(y, z)} + \Delta E_M + \Delta E_n; p \right) && \text{(loss in the gas)}. \end{aligned} \quad (5.2)$$

We can see that besides parameters a_j and b_j , which are specific for each OM, E_i now also depends on values θ , y and z , which are specific for each electron. To demonstrate the problem which it brings to the extraction of calibration parameters, let us first show how we would proceed if E_i was only a function of a_j , b_j and Q ($E_i = f(a_j, b_j, Q)$). In that case, we could again fit the peaks in the spectrum to extract their positions Q_1 and Q_2 . Knowing that these values correspond to energies $E_1 = 482$ keV and $E_2 = 976$ keV we would find a_j and b_j by solving a system of two equations.

$$E_1 = f(a_j, b_j, Q_1) \quad (5.3)$$

$$E_2 = f(a_j, b_j, Q_2) \quad (5.4)$$

This is analogical to the approach described in the section 3.3.3.2, only now we have a general function f . In case of $E_i = f(a_j, b_j, Q, \theta, x, y)$ it is no longer possible to write

the problem as a system of two equations. The reason for this is that now f is no longer a function acting on the charge spectrum as a whole, but it is a function acting on each electron individually. Because of that, it is no longer possible to extract the calibration parameters from the measured spectrum in a single fit. The only thing we can do is to choose a_j and b_j , calculate E_i for all electrons to get the spectrum of initial energies and only then check if the peaks in the spectrum are at correct positions, verifying our initial choice of a_j and b_j .

5.1 Calibration algorithm

To find calibration parameters of each OM, we apply the data cuts described in the chapter 3 to filter out background events. We also choose a fixed value of p common for all modules. The choice of this value will be commented on later. Then to find a_j and b_j we will proceed in the following way for each OM:

1. Choose arbitrary a_j and b_j .
2. Calculate $E_f = a_j Q + b_j$ for each electron detected by given OM.
3. Apply energy corrections to calculate E_i for each electron detected by given OM (equation (4.16) from chapter 4).
4. Fit the E_i energy spectrum using functions from the equation 4.18 to find positions μ_1 and μ_2 of the first and the second peak.
5. Calculate $L(a_j, b_j) = (\mu_1 - E_1)^2 + (\mu_2 - E_2)^2$, where $E_1 = 482$ keV and $E_2 = 976$ keV.

The point of this whole process is that the peaks in the E_i spectrum should be at the correct energies (482 and 976 keV), provided we have chosen correct a_j and b_j . The distance of the peaks from the correct energies is measured by the function $L(a_j, b_j)$, the value of which depends solely on the initial choice of a_j and b_j .¹ We will call this function a loss function. As we are only fitting two peaks, and we have two unknown parameters a_j and b_j it is theoretically possible to find values of these parameters for which $\mu_1 = E_1$ and $\mu_2 = E_2$. In this case $L(a_j, b_j) = 0$. This leads us to a conclusion that we need to find a_j and b_j for which L reaches its minimum.

5.1.1 Minimisation of the loss function

In the figure 5.1 we can see a visual representation of the process described in the section 5.1. Obviously, there is no analytical solution to the problem of minimizing the loss function. The calculation of $L(a_j, b_j)$ includes operations such as fitting the energy spectrum, which cannot be dealt with analytically. At the beginning of the process, we do not know which calibration parameters to choose to get $L(a_j, b_j) = 0$. Only at the end do we learn if the choice of a_j and b_j was correct. This leads us to use a numerical method which would allow reaching the minimum efficiently.

¹ $L(a_j, b_j)$ also depends on the initial choice of p , but for now we consider p to be fixed and a_j and b_j to be unknowns.

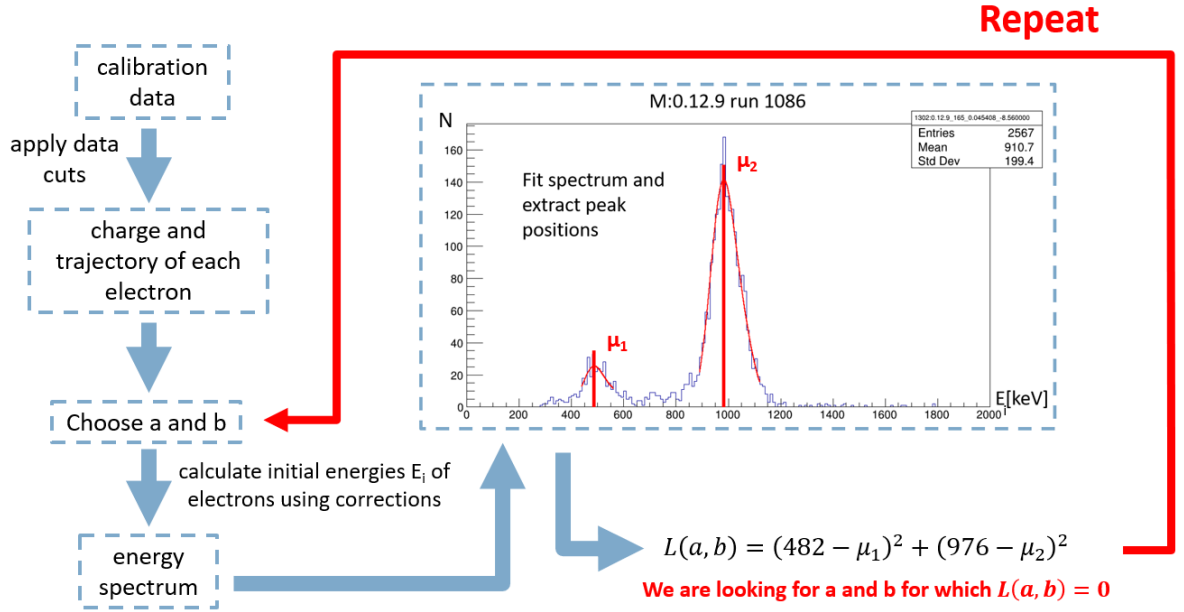


Figure 5.1: A diagram of the calibration algorithm. At the beginning, we apply data cuts and extract measured charge and trajectory of each electron. After that, we choose an arbitrary pair of calibration parameters a and b to calculate the spectrum of E_i . We fit the spectrum and extract the positions of the peaks μ_1 and μ_2 . Based on these positions, we calculate $L(a, b)$ expressing how far the peaks are from the correct values. We repeat the process until we find calibration parameters for which L is very close to zero.

5.1.1.1 Properties of the loss function

The loss function has specific properties which will influence our choice of the numerical minimization method. In the figure 5.2 we can see an example of the loss function for one chosen OM. We can see that there is a clear global minimum in the middle. This is to be expected, as there should not be ambiguity in choice of the most optimal calibration parameters. The second thing to note is that there are points in which the value of the function is clearly higher than in their neighbourhood. This comes from the fact that fitting of the E_i energy spectrum is involved in the calculation of the loss function. These fits sometimes fail to converge to the optimal solution, which results in this noise in the loss function. This noise could potentially even create local minima. Finally, it is important to note that evaluation of the loss function is computationally expensive. It requires us to calculate E_i for each electron detected by given OM and also to fit the resulting spectrum. The computational complexity also rises with the number of events in the calibration data, as for more events we need to make more calculations of E_i . Of course, with more events the noisiness of the loss function falls and the precision of the calibration rises, so it is desired to use bigger calibration datasets in spite of higher computational time.

The nature of the loss function narrows our choice of the minimization algorithm. For example, we cannot really reliably calculate the gradient of the function. There is no way to analytically express the gradient, and the noisiness of the function would cause a numerical calculation of the gradient to be very unstable. This rules out a whole class of gradient descend methods which are commonly used for minimization of multidimensional functions. In our case, we need a method which only uses functional

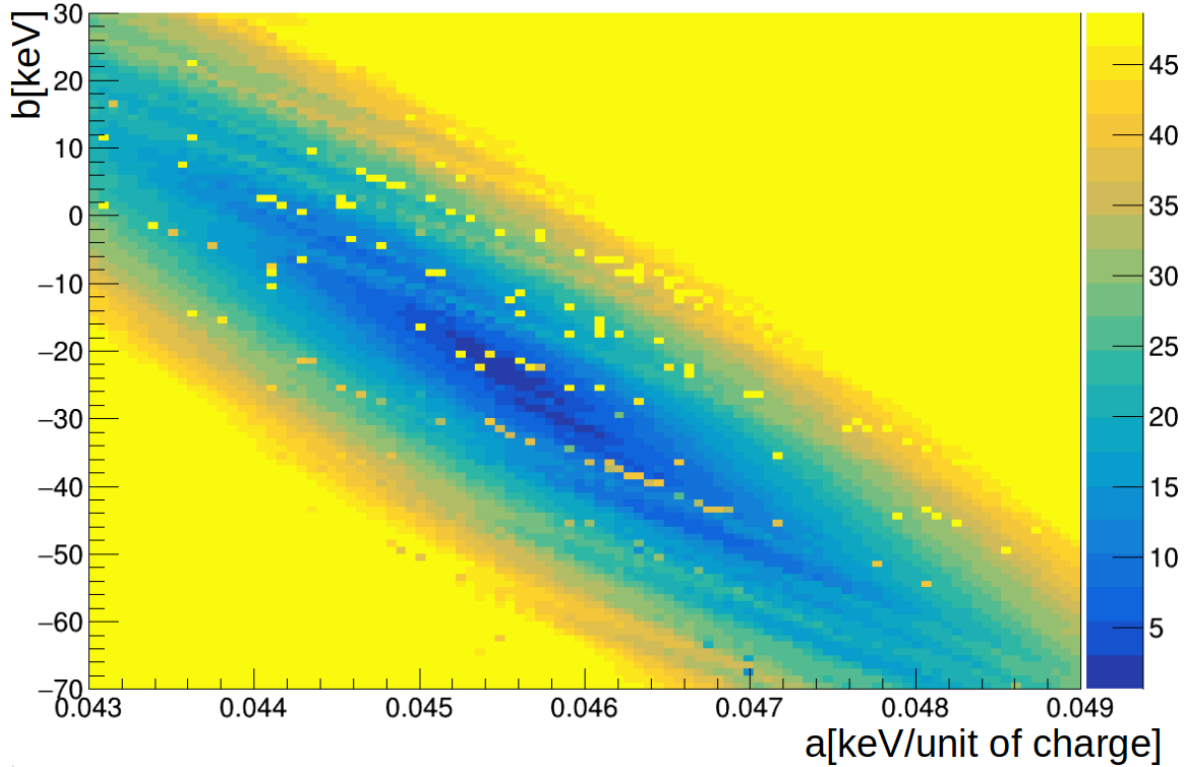


Figure 5.2: An example of the L function. We can see a clear global minimum in the middle. There is also a noise resulting from failed fits of the E_i spectrum.

values. We also need to make sure that the method is sufficiently robust to the noisiness.

5.1.1.2 Grid search

A very simple method which can be used for the minimization problem is the grid search. We simply choose a grid of points, evaluate the loss function in each of them, and find the one with the lowest value. In the next step, we can construct a finer grid around the lowest point. We repeat this until the value of L reaches the chosen threshold. In the figure 5.3 we can see grids chosen in two iterations of the algorithm.

The advantage of this algorithm is that if we adjust the shrinking of the grid correctly, it is very robust to the noise. If the fit in one of the function evaluations fails, the algorithm can correct itself in the next step. On the other hand, the algorithm requires a lot of function evaluations, making it slow. Especially for the bigger datasets, which will be used in practice, we would like to have a faster method.

5.1.1.3 Downhill simplex method

The downhill simplex method is a relatively simple minimization method which does not require calculation of gradients. It is described for example in Ref. [47]. In general, it is used to find a minimum of an N -dimensional function. In each step, it evaluates the function in $N+1$ points. According to functional values in these points, it chooses the points for the next step. In most cases, the point with the highest functional value is replaced.

In our case, we will evaluate the loss function in three points in every step. Let us switch to vector notation, where $\vec{x} = (a, b)$ and $L(\vec{x}) = L(a, b)$. In every step, we will

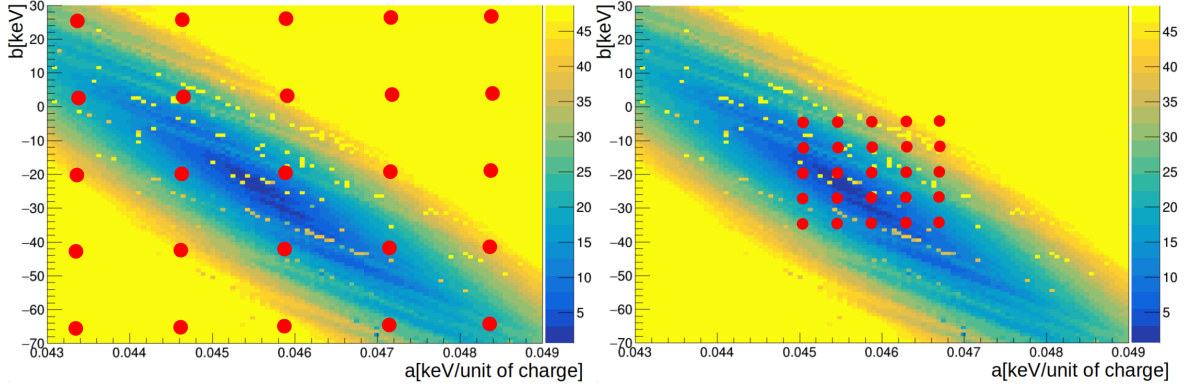


Figure 5.3: An example of two iterations of the grid search algorithm. In the second step, we construct a finer grid around the lowest point from the first step.

proceed in the following way:

1. Evaluate the loss function in three points \vec{x}_1 , \vec{x}_2 and \vec{x}_3 and let us assume that $L(\vec{x}_1) \leq L(\vec{x}_2) \leq L(\vec{x}_3)$.
2. Calculate $\vec{x}_o = \frac{\vec{x}_1 + \vec{x}_2}{2}$.
3. Calculate $\vec{x}_r = \vec{x}_o + \alpha(\vec{x}_o - \vec{x}_3)$. If $L(\vec{x}_1) \leq L(\vec{x}_r) < L(\vec{x}_3)$ then replace \vec{x}_3 with \vec{x}_r and go to 1.
4. If $L(\vec{x}_r) < L(\vec{x}_1)$ then calculate $\vec{x}_e = \vec{x}_o + \gamma(\vec{x}_r - \vec{x}_o)$. If $L(\vec{x}_e) < L(\vec{x}_r)$ then replace \vec{x}_3 with \vec{x}_e and go to 1, else replace \vec{x}_3 with \vec{x}_r and go to 1.
- 5a If $L(\vec{x}_r) < L(\vec{x}_3)$ then compute $\vec{x}_c = \vec{x}_o + \rho(\vec{x}_r - \vec{x}_o)$. If $L(\vec{x}_c) < L(\vec{x}_r)$ then replace \vec{x}_3 with \vec{x}_c and go to 1, else go to 6.
- 5b If $L(\vec{x}_r) \geq L(\vec{x}_3)$ then compute $\vec{x}_c = \vec{x}_o + \rho(\vec{x}_3 - \vec{x}_o)$. If $L(\vec{x}_c) < L(\vec{x}_3)$ then replace \vec{x}_3 with \vec{x}_c and go to 1, else go to 6.
- 6 Replace \vec{x}_2 with $\vec{x}_1 + \sigma(\vec{x}_2 - \vec{x}_1)$, \vec{x}_3 with $\vec{x}_1 + \sigma(\vec{x}_3 - \vec{x}_1)$ and go to 1.

α , γ , ρ and σ are constants where $\alpha > 0$, $\gamma > 1$, $0 < \rho \leq 0.5$ and $0 < \sigma \leq 1$. We choose $\alpha = 1$, $\gamma = 2$, $\rho = 0.5$ and $\sigma = 0.5$. The steps 3, 4, 5 and 6 are commonly called reflection, expansion, contraction and shrink respectively. This refers to the movement of the simplex. The different steps can be seen in the figure 5.4. For termination of the algorithm, we again choose a fixed threshold. We know that the minimal value of the loss function is always 0 so we can choose the threshold as a small positive value. When any of the values $L(\vec{x}_1)$, $L(\vec{x}_2)$ and $L(\vec{x}_3)$ in the step 1 gets lower than the threshold, we stop the algorithm.

The downhill simplex method requires significantly lower number of function evaluations than the grid search method, making it much faster. The only concern is its robustness to the noisiness of the loss function. Especially for smaller calibration datasets, the function can converge to a local minimum created by the noise. When tested on bigger datasets, however, the method converges well in the vast majority of cases. A solution for the cases where it fails could be to rerun the minimization using the grid search.

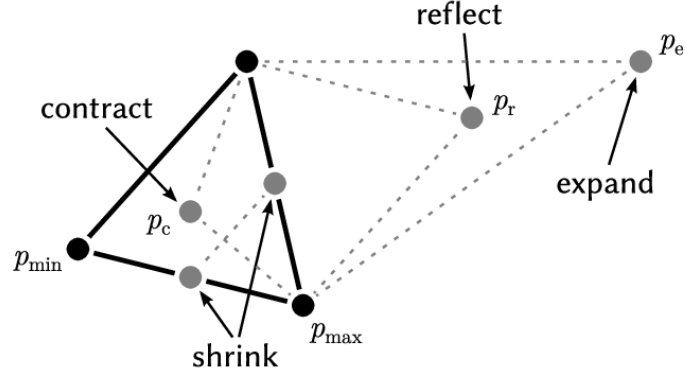


Figure 5.4: Four different steps of the downhill simplex method. The figure was adapted from Ref. [51].

There are algorithms which achieve faster convergence than the downhill simplex method. The simplex method was mainly chosen for its simplicity, as a first attempt to solve the problem. If there will be a need for better performance in the future, more advanced algorithms can be tested. However, the calibration process will not be performed on a daily basis, so there might not be a need for further optimization. The processing of 51 h of calibration data using the downhill simplex method took less than 20 minutes on a single processor. For the grid search method, the processing time varies based on its configuration, but typically reaches several hours.

5.1.2 Dependence of the calibration parameters on the tracking gas pressure

In the section 5.1 we considered the pressure p to be a fixed constant. Now we will be interested in how its choice influences the calibration parameters. Let us come back to the formula for calculation of E_i from the chapter 4

$$\begin{aligned}
 E_i(E_D, \theta; p) = & E_D && \text{(deposited energy)} \\
 & + \Delta E_M(\theta, E_D) && \text{(loss in Mylar)} \\
 & + \Delta E_n(\theta, E_D + \Delta E_M) && \text{(loss in nylon)} \\
 & + \Delta E_g(\theta, E_D + \Delta E_M + \Delta E_n; p) && \text{(loss in the gas)}.
 \end{aligned}$$

If we neglect the optical correction, we have $E_D = E_F = a_j Q + b_j$. We can then write the formula as

$$\begin{aligned}
 E_i(Q, \theta; p, a_j, b_j) = & a_j Q + b_j && \text{(deposited energy)} \\
 & + \Delta E_M(\theta, a_j Q + b_j) && \text{(loss in Mylar)} \\
 & + \Delta E_n(\theta, a_j Q + b_j + \Delta E_M) && \text{(loss in nylon)} \\
 & + \Delta E_g(\theta, a_j Q + b_j + \Delta E_M + \Delta E_n; p) && \text{(loss in the gas)}.
 \end{aligned}$$

The $a_j Q$ term is the most significant one. We can see that both b_j and ΔE_g are values added to the $a_j Q$ term. It is also important to note that ΔE_g scales linearly with p . This gives us an intuition that changing p by a certain value is in some way equivalent to changing b_j for all OMs. This equivalence is not exact because b_j is a parameter of

a specific OM, while ΔE_g is calculated for each detected electron separately. Despite this, the mentioned relationship between the terms is still important. Thanks to this, we can expect that the b parameter averaged over all OMs will change approximately linearly with p . On the other hand, the average of a should be unaffected by p .

Because both b_j and the energy loss terms (ΔE_M , ΔE_n and ΔE_g) shift E_i , we can state a hypothesis that all the energy shift can be explained by energy losses. Then the average b_j would be equal to zero. This hypothesis allows us to verify the energy loss correction on the real data. If the value of p , for which the average b_j is zero, is the same as the real pressure of the tracking gas measured during the measurement, then we could assume that the energy loss model corresponds to the real data and that it explains all the shift of E_i .

In the figure 5.5, we can see distributions of b_j obtained without any energy corrections (red), with only the optical corrections (green), with only the energy loss corrections (purple) and with both the optical corrections and the energy loss corrections (blue), using the real value of pressure $p = 0.88$ bar. The means of these distributions are 63.6 keV, 35.2 keV, 26 keV and -2.1 keV, respectively. We can see that the energy corrections move the distribution much closer to zero. This leads us to the conclusion, that the b parameter can be explained by energy losses of electrons for the most part. It is also important to note, that one of the corrections on its own does not shift the distribution of b to zero. It is only their combination which results in a very low absolute value of average b .

In the figure 5.6a we can see how the distribution of b changes for p different from the real value of 0.88 bar. Average b equal to zero is reached for $p = 0.82$ bar. As in the case of simulation, this value is slightly different from the expected value of 0.88 bar. Again, there seems to be slight systematic error. In the figure 5.6b we can see how distribution of the a parameter depends on value of p . In this case, the distribution does not change with p . This means that when combined, the energy corrections move both peaks in the spectrum by the same value.

By showing that the average b parameter moves very close to zero after application of the energy corrections, we have now validated the energy correction on both simulated and real data. We have also developed an algorithm, which allows use to include the corrections into the process of calibration. At this point, we have a complete framework including efficient data cuts, energy corrections and a method of calibration parameter extraction. Author's notes and some code created during the development process can be found on GitHub [52]. In the future, it will also be updated with new results. In the last chapter, we will use the created framework to calculate energy resolutions of individual OMs.

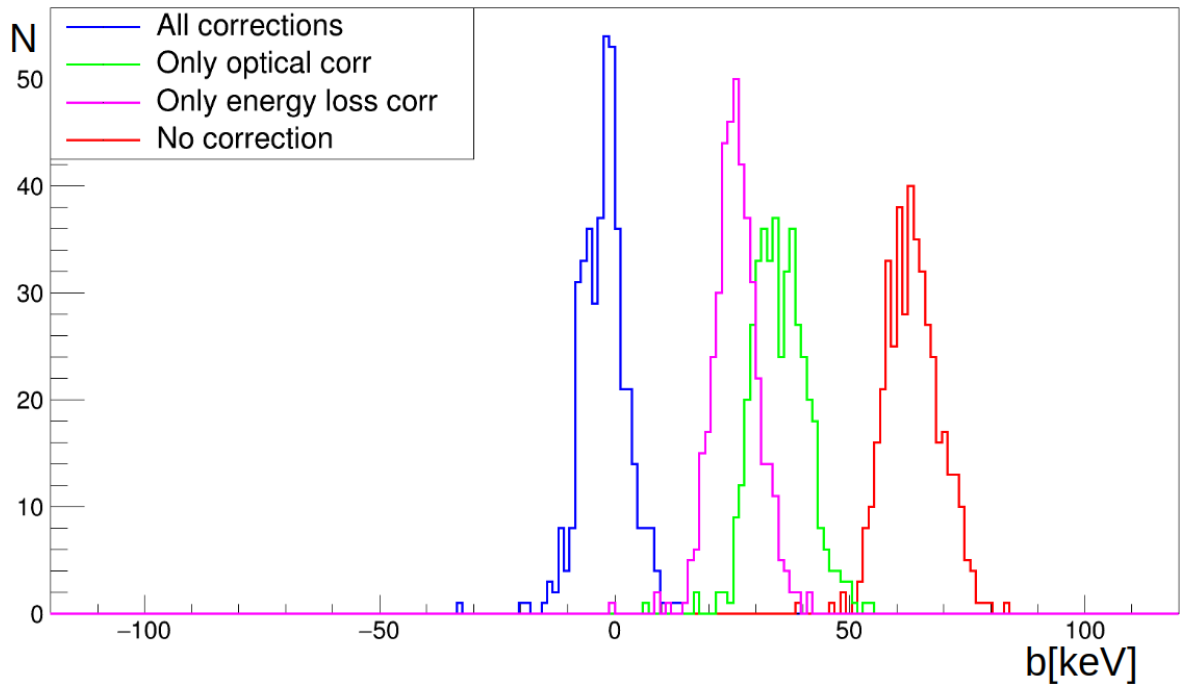


Figure 5.5: A comparison of distributions of the b_j parameter. The red values were obtained without application of any energy corrections, the green values were obtained with application of the optical corrections only, the purple values were obtained with application of energy loss corrections only and the blue values were obtained with application of both the optical corrections and the energy loss corrections. We can see that the energy corrections move the distribution much closer to zero. The means of the red, green, purple and blue distributions are 63.6 keV, 35.2 keV, 26 keV and -2.1 keV, respectively. We can see that in the first three cases the values are far from zero, but the combination of both corrections shifts the distribution very close to zero.

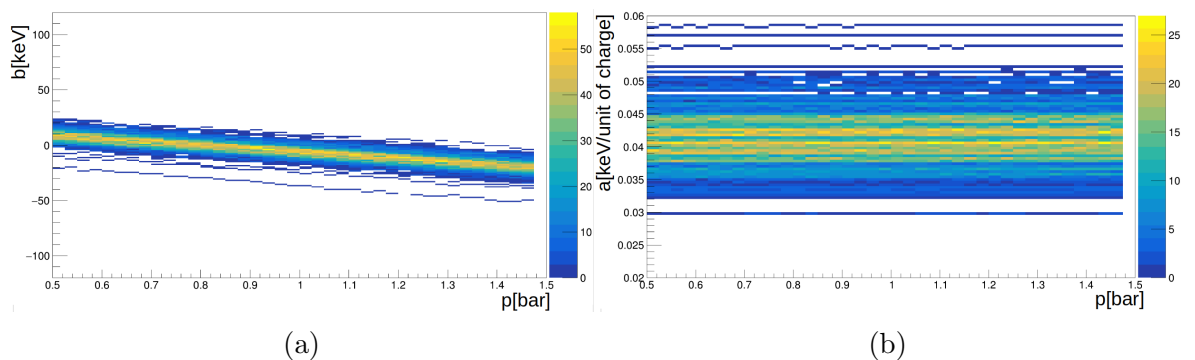


Figure 5.6: a) A relationship between distribution of the b parameter and the pressure p . We can see that with increasing p b linearly declines. An average b of 0 is reached for $p = 0.82$ bar. b) A relationship between distribution of the a parameter and the pressure p . We can see that the distribution of a does not depend on p .

Chapter 6

Estimation of SuperNEMO energy resolution

The main property of OMs is their energy resolution, as it influences sensitivity of the whole detector. Let us assume that we detect monoenergetic electrons with energy E . If we had a perfect detector, we would measure a spectrum composed of a single delta peak at E . A real detector, however, always measures with some uncertainty caused by different effects such as noise in electronics. This uncertainty smears the delta peak, and we observe a spectrum in a shape of Normal distribution instead. We define energy resolution of the detector as

$$R(E) = \frac{FWHM_E}{E} = 2.355 \cdot \frac{\sigma}{E}, \quad (6.1)$$

where $FWHM_E$ is full width at half maximum of the Normal distribution and σ is the standard deviation of the Normal distribution. $FWHM_E$ grows with \sqrt{E} . From that we get $R \sim \frac{1}{\sqrt{E}}$, so the resolution is better for higher energies. To compare resolutions, we need to choose an energy, for which it is calculated. In our case, we will rescale resolutions to 1 MeV regardless from which peak they were extracted. We can calculate it by rescaling $R(E)$

$$R_{1\text{MeV}}(E) = \sqrt{\frac{E}{1\text{ MeV}}} R(E), \quad (6.2)$$

where $R(E)$ is the resolution at arbitrary energy E . Combining (6.1) and (6.2) we get

$$R_{1\text{MeV}}(E) = 2.355 \cdot \sqrt{\frac{E}{1\text{ MeV}}} \frac{\sigma}{E}. \quad (6.3)$$

We will calculate the energy resolution from the Gaussian fit of the E_i spectrum. For each module, we first extract calibration parameters a_j and b_j using the algorithm described in the previous chapter. With this pair of parameters, we then calculate the E_i spectrum for a given module using formula (5.2). Finally, we fit the two peaks in the spectrum with the fitting function described in the chapter 4. From the fit, we obtain means and standard deviations μ_1 , μ_2 , σ_1 and σ_2 . Using formula (6.3) we calculate resolution at 1 MeV for each peak separately as

$$R_{1\text{MeV}}(\mu_1) = 2.355 \cdot \sqrt{\frac{\mu_1}{1\text{ MeV}}} \frac{\sigma}{\mu_1}, \quad R_{1\text{MeV}}(\mu_2) = 2.355 \cdot \sqrt{\frac{\mu_2}{1\text{ MeV}}} \frac{\sigma}{\mu_2}. \quad (6.4)$$

Because we fit the spectrum of E_i , the resolution we get tells us how precisely we are able to reconstruct the initial energy of electrons. In contrast to that, we could also fit the spectrum of E_f and extract resolution for the final energy of electrons. The strength of energy corrections is, however, in reconstruction of the initial energy which is why we focus on the former. We restrict ourselves to calculating resolutions of the main wall OMs (excluding the topmost and the bottommost row), as these receive most exposure and are the most important for the sensitivity of the detector. Because both $R_{1\text{MeV}}(\mu_1)$ and $R_{1\text{MeV}}(\mu_2)$ are rescaled to 1 MeV, we expect these values to be approximately equal.

6.1 Simulation

To obtain values with which we could compare energy resolutions extracted from the real data, we first extracted resolutions from the simulated ^{207}Bi data. In the simulation, the effect of energy resolution is applied artificially. The electron's initial energy E_i is first influenced by the effect of energy losses, as well by the non-uniformity and non-linearity of the OM. The resulting energy is then smeared by a Gaussian distribution. The standard deviation of the distribution is chosen as 8% of the energy, for all main wall OMs. This value is based on OM measurements which were performed before assembly of the SuperNEMO detector. In the figure 6.1 we can see a comparison of energy resolutions extracted with the use of energy corrections (blue) and without (red). In the figure 6.2 we can see the same comparison but for the resolutions extracted from the second peak. In these plots, we can notice two things. First, the resolutions calculated with the use of energy corrections are better than the ones calculated without them. This tells us that the corrections could improve the precision of energy reconstruction. We can also notice that the resolutions extracted from the first peak are less sensitive to the energy corrections, than the ones extracted from the second. In case of the second peak the improvement due to corrections is 1.1% while for the first peak it is only 0.5%. Second, the resolutions extracted from the first peak are better than the ones extracted from the second one. This discrepancy is strange, as we normalize both resolutions to 1 MeV, so we would expect to arrive to the same values. The reason behind this has not yet been resolved. A possible explanation could lie in inclusion of the additive parameter in the fitting function used for the first peak (see equation (4.18)). The influence of the parameter on the calculated resolutions should be further studied. Because of this issue, we will focus our attention more on the energy resolutions extracted from the second peak, as those are more reliable.

6.2 Real data

Energy resolutions extracted from the real data can be seen in the figure 6.3 for the first peak and in the figure 6.4 for the second peak. In the figure 6.5, we can also see a map depicting distribution of energy resolutions across both main walls. Again, the blue energy resolutions were calculated with energy corrections and the red ones were calculated without them. As in the simulated data, there is the discrepancy between the first and the second peak. The application of energy corrections again leads to better energy resolutions, but the improvement is not as significant as in the simulated data. In the map of energy resolutions (figure 6.5), we can see that we get better

Res. at 1 MeV (simulated data, first peak)

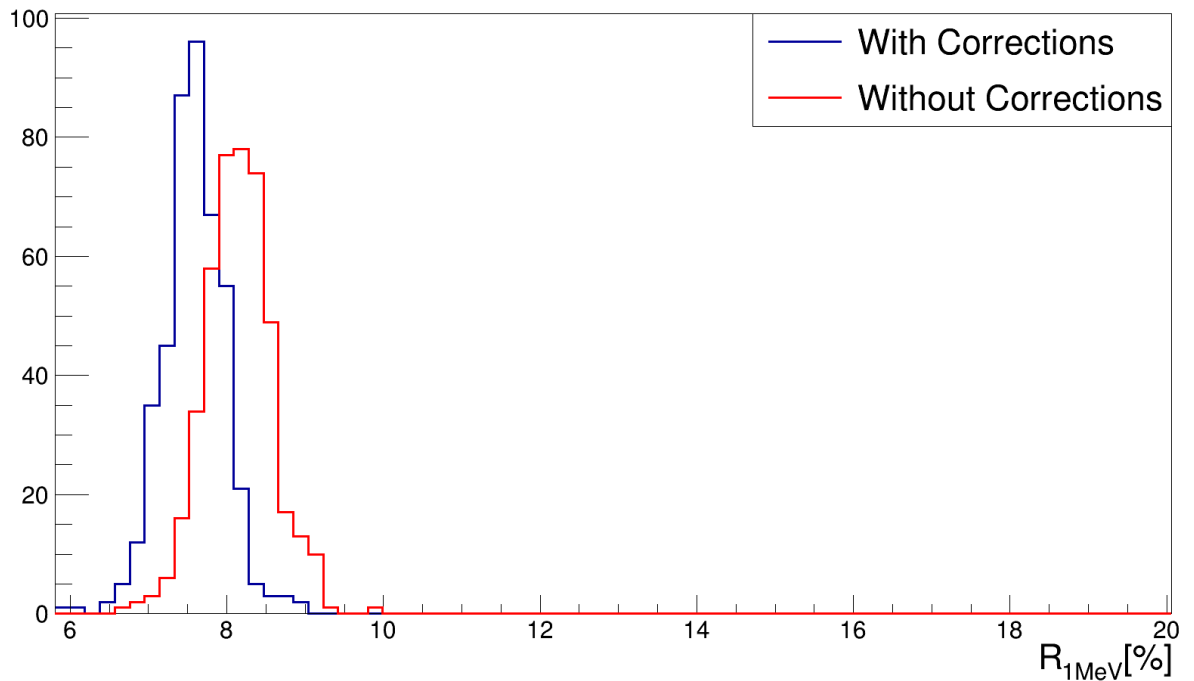


Figure 6.1: Energy resolutions extracted from the first peak from simulated data. The blue resolutions were extracted with the use of energy corrections, while the red resolutions were extracted without them. The mean resolution is 7.6% with corrections and 8.1% without.

Res. at 1 MeV (simulated data, second peak)

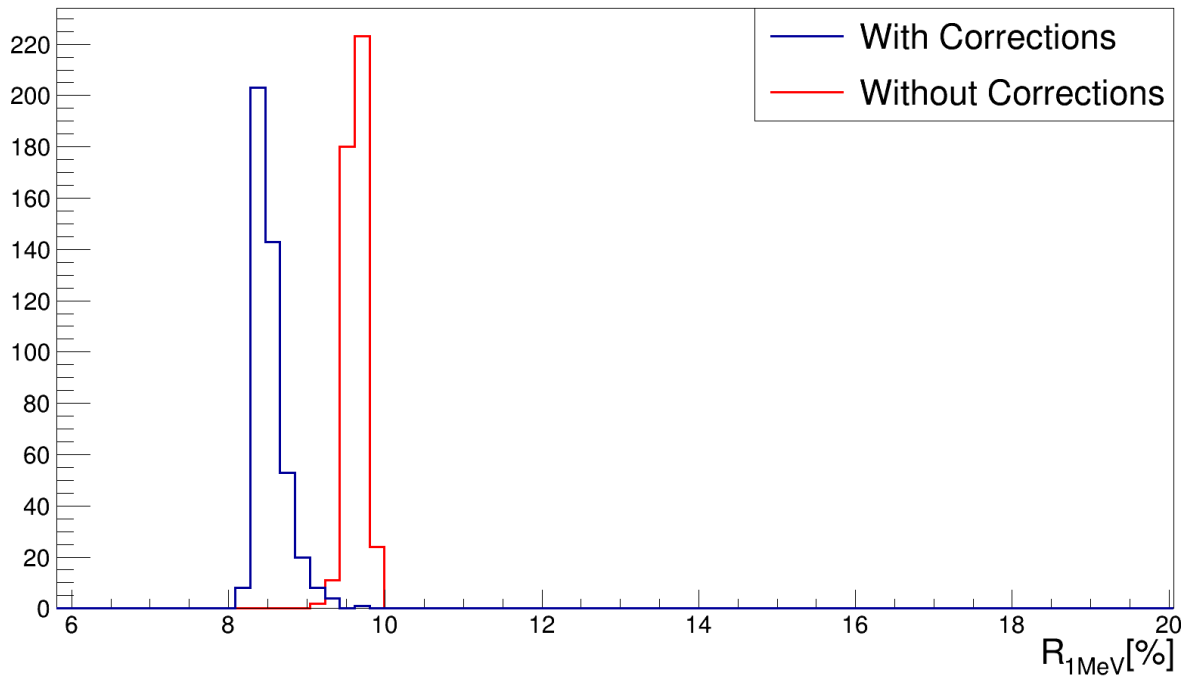


Figure 6.2: Energy resolutions extracted from the second peak from simulated data. The blue resolutions were extracted with the use of energy corrections, while the red resolutions were extracted without them. The mean resolution is 8.5% with corrections and 9.6% without.

energy resolutions for the Italian side than for the French side. This difference can be explained by the fact, that several scintillator compositions have been used for the main wall OMs. In the figure 6.6 we can see a map of different OM compositions. The purple modules use a scintillator with enhanced composition, which resulted in better energy resolution during testing. The Italian side contains far more of these OMs giving us better overall energy resolution.

Probably the most important is the comparison between energy resolutions extracted from the simulated and from the real data. We would expect the real resolutions to be close to the simulated ones, as the energy smearing applied in the simulation is based on initial testing of OMs. Based on distributions from figures 6.2 and 6.4, we get average energy resolution of 8.5 % for the simulated data and 12 % for the real data (second peak, with corrections). This degradation of energy resolution has not yet been resolved. One possibility is that OMs deteriorate with time. They were assembled and tested between 2014 and 2016, so it is possible that their properties have changed since then due to ageing effect. This hypothesis could potentially be tested by comparing calibration data from different timeframes, as the first calibration measurements have already been performed in 2021. Some work on this part has already been done. In the figure 6.7, we can see evolution of the energy resolution in a span of one and a half year. There seems to be increasing tendency, although, this result has been achieved using a less precise method and the problem should be studied in more detail.

There also certainly are possible improvements to the presented analysis. An example could be a better extraction of measured charge. Currently, charge measured by OMs is calculated by a firmware embedded in the electronics. The signal measured by OMs is sampled in discrete timestamps with a fixed frequency. The firmware then simply calculates the charge by summing amplitudes measured in timestamps across the whole signal waveform. This calculation might be negatively affected by the noise of electronics. It could be replaced by a more precise method, such as waveform fitting. We would fit the waveform measured by an OM using a suitable function and then calculate the charge based on the integral of this function. Another point of analysis will be the discrepancy between the energy resolutions extracted from the first and from the second peak. The influence of the additional C parameter on the first peak fit will be studied.

In conclusion, we have conducted the first energy resolution analysis which takes into account both the non-uniformity and non-linearity of OMs as well as the energy losses of electrons. We have shown that the application of energy corrections can improve the resolution. The resolutions extracted from the real data were compared to the ones from simulation. The difference between the average energy resolution extracted from the simulated and from the real data is 3.5%. This result can be caused by several factors and will be further studied in the future.

Res. at 1 MeV (real data, first peak)

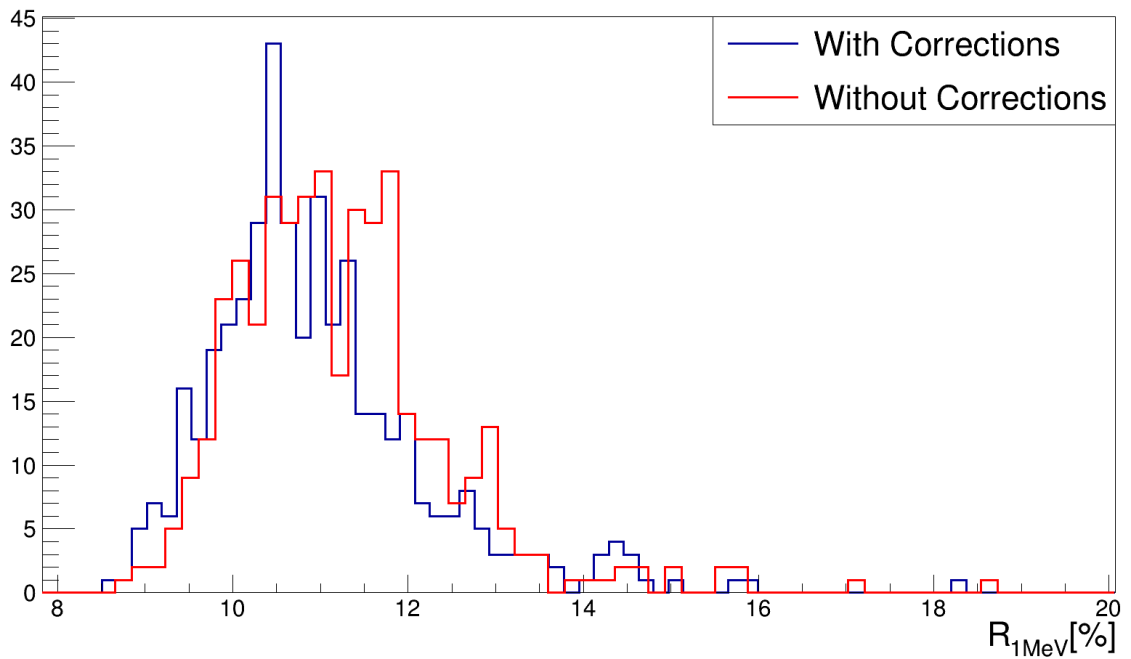


Figure 6.3: Energy resolutions extracted from the first peak from real data. The blue resolutions were extracted with the use of energy corrections, while the red resolutions were extracted without them. The mean resolution is 11% with corrections and 11.2% without.

Res. at 1 MeV (real data, second peak)

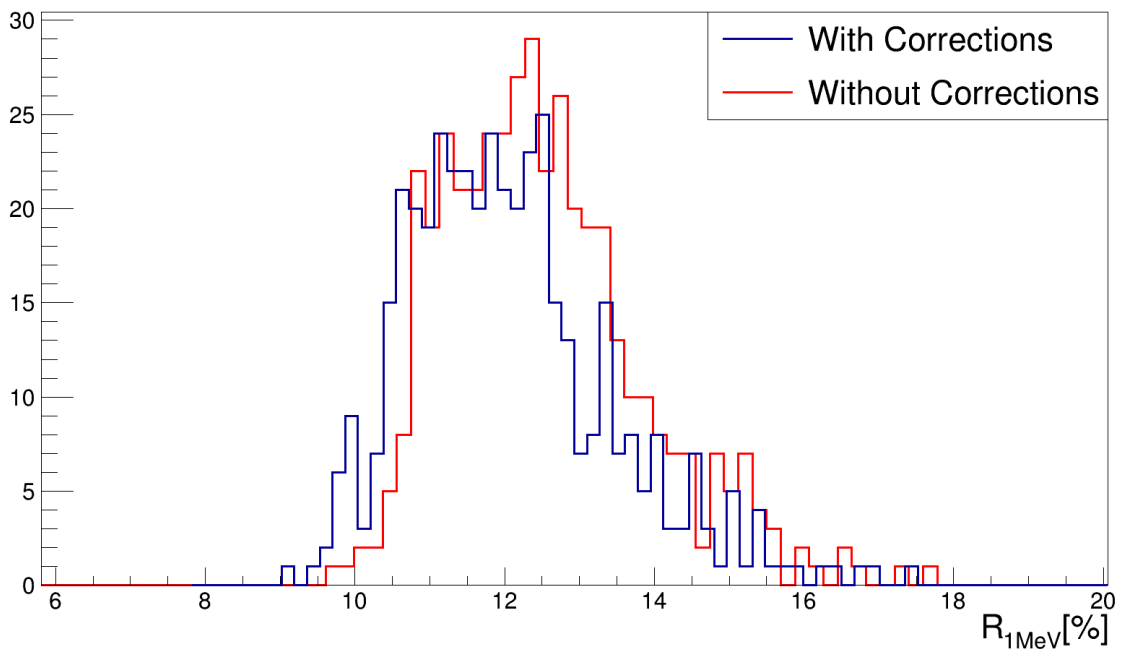


Figure 6.4: Energy resolutions extracted from the second peak from real data. The blue resolutions were extracted with the use of energy corrections, while the red resolutions were extracted without them. The mean resolution is 12% with corrections and 12.5% without.

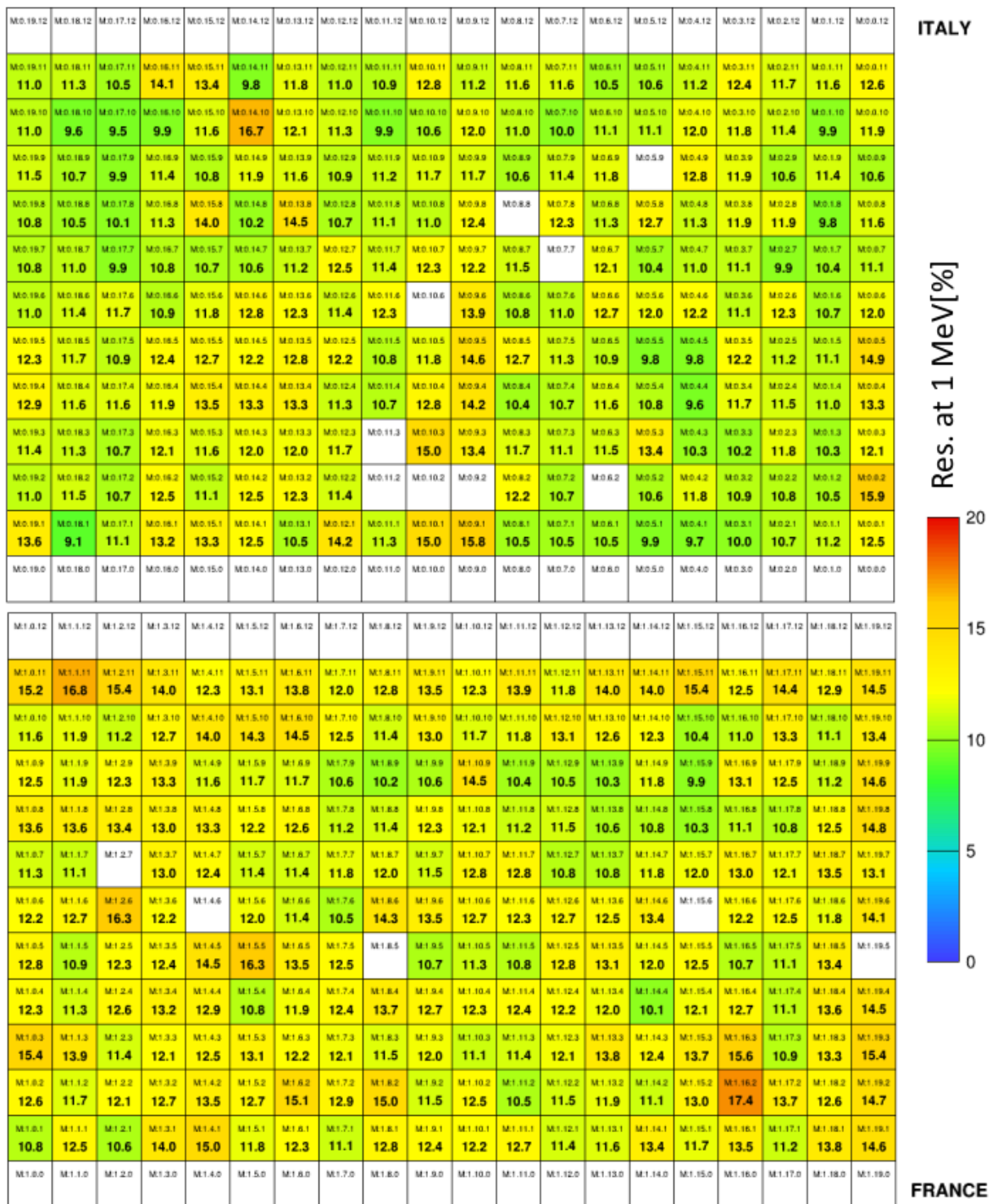


Figure 6.5: A map of energy resolutions extracted from the second peak for both main walls. The blank modules are either non-functional or were removed from the data due to a failed spectrum fit.

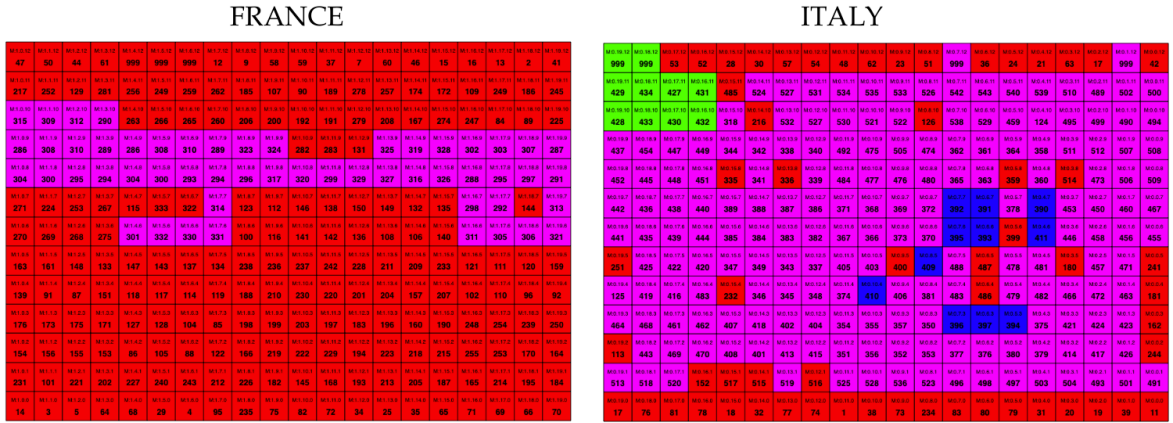


Figure 6.6: A map of OM compositions. Each colour represents different scintillator composition. During testing, the purple, and green OMs generally had better energy resolution than the red and blue ones. This explains the fact, that in the calibration data we observe better energy resolution on the Italian side.

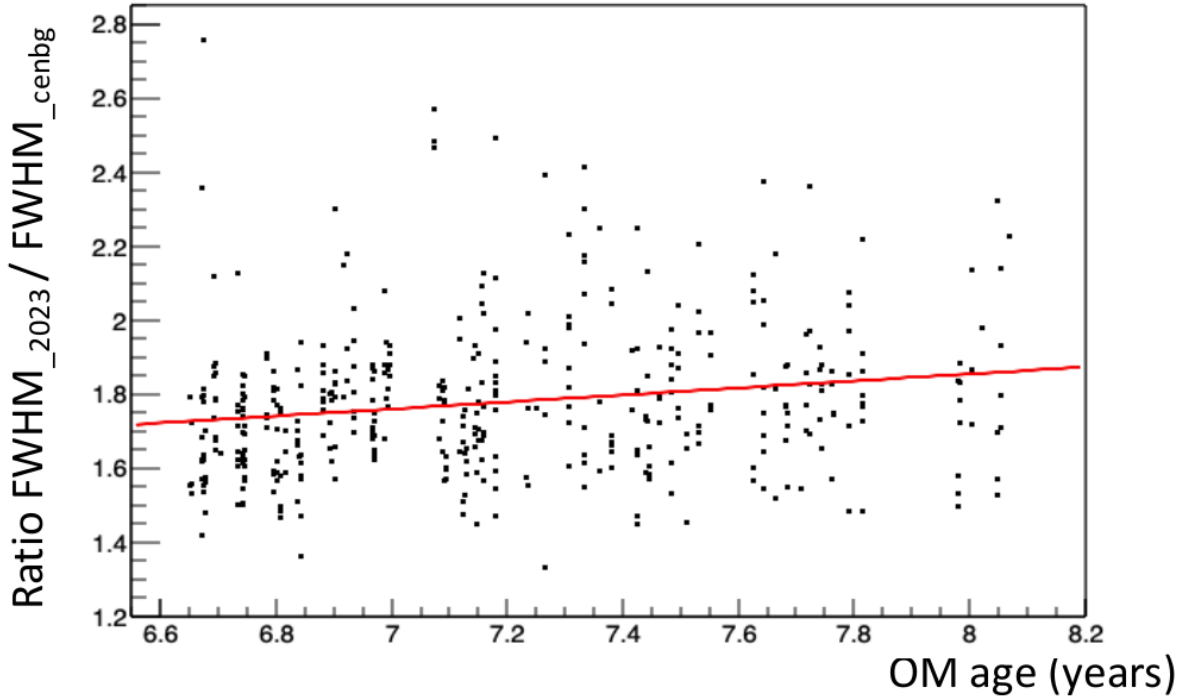


Figure 6.7: Evolution of OM energy resolution with time. The value on the y-axis represents the ratio between energy resolution measured in 2023 and energy resolution measured in ideal condition before assembly of the SuperNEMO detector. The energy resolutions used in this plot were extracted using a simpler method than the one described in this work. Courtesy of the SuperNEMO collaboration.

Conclusions

The goal of this work was to provide a complete algorithm for calibration of individual optical modules of the SuperNEMO detector. The first two chapters contain brief introduction into neutrino physics and summary of different experiments focusing on the $0\nu\beta\beta$ -decay followed by description of the SuperNEMO detector, its individual components and the calibration system. The following chapters focus on different parts of the calibration process including data cuts, energy corrections, algorithm for calibration parameter extraction and calculation of energy resolution.

The third chapter deals with calibration data. It first describes different data formats used within the SuperNEMO experiment, and then proposes a set of data cuts to select ^{207}Bi electron events from the calibration data. The data cuts mainly take advantage of the track reconstruction, which allows to precisely verify if the observed trajectory comes from a calibration source or not. It was shown that the set of data cuts very efficiently suppresses background, keeping only 0.56 background events at 901 signal events per OM per hour. The end of the chapter describes the problem of significant gain variation which can be observed in few OMs and shows a simple correction, which can be used to reduce the effect of the gain variation on the measured spectrum.

The fourth chapter focuses on different effects affecting the measured energy spectrum of ^{207}Bi electrons. First, it briefly describes the effects causing non-linearity and geometrical non-uniformity of OM response. It describes a group of so-called optical corrections, which are designed to model and correct these effects. Most of the chapter is dedicated to the model of ^{207}Bi electron energy losses in the detector. A phenomenological energy loss model, which was developed during previous work, is introduced. It is shown that this model has several flaws such as high number of fitting parameters as well their lack of physical interpretation. These flaws lead to a need for a physics-based model. A new model based on the Bethe-Bloch formula for electrons is proposed. The model uses only one free parameter: pressure of the gas in the tracker. This is a significant improvement when compared to the five parameters of the phenomenological model. The validity of the new model can also be easily verified, as the tracking gas pressure is a measured observable. At the end of the chapter, the new model is applied to the measured energy spectrum from simulation with the assumption that if the model is valid then the peaks in the corrected energy spectrum should be at the theoretical energies of 482, 976 and 1682 keV. This is achieved for the choice of $p = (0.921 \pm 0.006)$ bar. For comparison, the pressure used in the simulation is 0.89 bar. The small error of 0.03 bar shows that the model provides good description of the energy losses.

The fifth chapter combines the data cuts and energy corrections from the previous chapters into a complete algorithm for calibration parameter extraction. It is described that the energy corrections are applied to each electron individually, which complicates

the calibration process. These complications lead to a problem of numerical optimization, which is then solved using the Downhill simplex method. The calibration algorithm is then used to study the dependence of extracted calibration parameters on the choice of pressure for the energy loss correction. It is shown that the shift parameter b gets very close to zero, when both of the energy corrections are applied. This again proved the validity of the energy corrections.

The last chapter discusses energy resolution of the SuperNEMO detector. The OMs are calibrated using the developed algorithm and based on the calibrated energy spectra, the energy resolution of each OM is calculated. This calculation is done both with and without energy corrections and for both real and simulated data. It is shown that the application of energy corrections results in better energy resolution. The average energy resolution obtained with energy corrections is 8.5% at 1 MeV for the simulated data and 12% at 1 MeV for the real data. A possible reason for this difference could be ageing of the OMs. The causes of the worse energy resolution observed in the real data will be studied in more detail in the future work.

Author's notes and some code created during this work can be found on GitHub [52]. In the future, it will also be updated with newer results. The results of this work were presented at multiple meetings of the SuperNEMO collaboration, as well as at the poster session of TAUP 2023 conference.

Bibliography

1. BILENKY, S. M. Neutrino. History of a unique particle. *The European Physical Journal H*. 2013, vol. 38, no. 3, pp. 345–404. ISSN 2102-6467. Available from DOI: 10.1140/epjh/e2012-20068-9.
2. PAULI, W. *Pauli letter collection: letter to Lise Meitner*. [N.d.]. Available also from: <https://cds.cern.ch/record/83282>.
3. COWAN, C. L. et al. Detection of the Free Neutrino: a Confirmation. *Science*. 1956, vol. 124, no. 3212, pp. 103–104. Available from DOI: 10.1126/science.124.3212.103.
4. REINES, F.; COWAN, C. The Reines-Cowan experiments: Detecting the Poltergeist. *Los Alamos Sci*. 1997, vol. 25, pp. 4–27.
5. DANBY, G. et al. Observation of High-Energy Neutrino Reactions and the Existence of Two Kinds of Neutrinos. *Physical Review Letters*. 1962, vol. 9, pp. 36–44. Available from DOI: 10.1103/PhysRevLett.9.36.
6. PERL, M. L. et al. Evidence for Anomalous Lepton Production in $e^+ - e^-$ Annihilation. *Physical Review Letters*. 1975, vol. 35, pp. 1489–1492. Available from DOI: 10.1103/PhysRevLett.35.1489.
7. KODAMA, K. et al. Observation of tau neutrino interactions. *Physics Letters B*. 2001, vol. 504, no. 3, pp. 218–224. ISSN 0370-2693. Available from DOI: [https://doi.org/10.1016/S0370-2693\(01\)00307-0](https://doi.org/10.1016/S0370-2693(01)00307-0).
8. CLEVELAND, B. T. et al. Measurement of the Solar Electron Neutrino Flux with the Homestake Chlorine Detector. *The Astrophysical Journal*. 1998, vol. 496, no. 1, p. 505. Available from DOI: 10.1086/305343.
9. GRIBOV, V.; PONTECORVO, B. Neutrino astronomy and lepton charge. *Physics Letters B*. 1969, vol. 28, no. 7, pp. 493–496. ISSN 0370-2693. Available from DOI: [https://doi.org/10.1016/0370-2693\(69\)90525-5](https://doi.org/10.1016/0370-2693(69)90525-5).
10. FUKUDA, Y. et al. Evidence for Oscillation of Atmospheric Neutrinos. *Physical Review Letters*. 1998, vol. 81, pp. 1562–1567. Available from DOI: 10.1103/PhysRevLett.81.1562.
11. AHMAD, Q. R. et al. Measurement of the Rate of $\nu_e + d \rightarrow p + p + e^-$ Interactions Produced by ^8B Solar Neutrinos at the Sudbury Neutrino Observatory. *Physical Review Letters*. 2001, vol. 87, p. 071301. Available from DOI: 10.1103/PhysRevLett.87.071301.
12. SALAS, P. F. de et al. Neutrino Mass Ordering from Oscillations and Beyond: 2018 Status and Future Prospects. *Frontiers in Astronomy and Space Sciences*. 2018, vol. 5. ISSN 2296-987X. Available from DOI: 10.3389/fspas.2018.00036.

13. CAHN, R. N. et al. *White Paper: Measuring the Neutrino Mass Hierarchy*. 2013. Available from arXiv: 1307.5487 [hep-ex].
14. AKER, M. et al. Direct neutrino-mass measurement with sub-electronvolt sensitivity. *Nature Physics*. 2022, vol. 18, no. 2, pp. 160–166. ISSN 1745-2481. Available from DOI: 10.1038/s41567-021-01463-1.
15. PLANCK COLLABORATION et al. Planck 2018 results - VI. Cosmological parameters. *AA*. 2020, vol. 641, A6. Available from DOI: 10.1051/0004-6361/201833910.
16. GOEPPERT-MAYER, M. Double Beta-Disintegration. *Physical Review*. 1935, vol. 48, pp. 512–516. Available from DOI: 10.1103/PhysRev.48.512.
17. VOLKMER, J. *Prospects of the Investigation of EC/Beta+ Decays With the COBRA Experiment*. 2018. MA thesis.
18. FURRY, W. H. On Transition Probabilities in Double Beta-Disintegration. *Physical Review*. 1939, vol. 56, pp. 1184–1193. Available from DOI: 10.1103/PhysRev.56.1184.
19. GÓMEZ-CADENAS, J. J. et al. The search for neutrinoless double-beta decay. *La Rivista del Nuovo Cimento*. 2023, vol. 46, no. 10, pp. 619–692. ISSN 1826-9850. Available from DOI: 10.1007/s40766-023-00049-2.
20. ACKERMANN, K.-H. et al. The Gerda experiment for the search of $0\nu\beta\beta$ decay in ^{76}Ge . *The European Physical Journal C*. 2013, vol. 73, no. 3. Available from DOI: 10.1140/epjc/s10052-013-2330-0.
21. GUISEPPE, V.E. et al. The MAJORANA neutrinoless double-beta decay experiment. In: 2008, pp. 1793–1798. Available from DOI: 10.1109/NSSMIC.2008.4774740.
22. AGOSTINI, M. et al. Final Results of GERDA on the Search for Neutrinoless Double- β Decay. *Physical Review Letters*. 2020, vol. 125, p. 252502. Available from DOI: 10.1103/PhysRevLett.125.252502.
23. ARNQUIST, I. J. et al. Final Result of the Majorana Demonstrator’s Search for Neutrinoless Double- β Decay in ^{76}Ge . *Physical Review Letters*. 2023, vol. 130, p. 062501. Available from DOI: 10.1103/PhysRevLett.130.062501.
24. ABGRALL, N.; ABRAMOV, A.; ABROSIMOV, N., et al. The large enriched germanium experiment for neutrinoless double beta decay (LEGEND). *AIP Conference Proceedings*. 2017, vol. 1894, no. 1, p. 020027. ISSN 0094-243X. Available from DOI: 10.1063/1.5007652.
25. FUJIKAWA, B.; LIGI, C. Search for Majorana neutrinos exploiting millikelvin cryogenics with CUORE. *Nature*. 2022, vol. 604, pp. 53–58. Available from DOI: 10.1038/s41586-022-04497-4.
26. ALFONSO, K. et al. CUPID: The Next-Generation Neutrinoless Double Beta Decay Experiment. *Journal of Low Temperature Physics*. 2023, vol. 211, no. 5-6, pp. 375–383. Available from DOI: 10.1007/s10909-022-02909-3.
27. KIM, H. B. et al. Status and Performance of the AMoRE-I Experiment on Neutrinoless Double Beta Decay. *Journal of Low Temperature Physics*. 2022, vol. 209, no. 5, pp. 962–970. ISSN 1573-7357. Available from DOI: 10.1007/s10909-022-02880-z.

28. ALBERT, J. B. et al. Search for Neutrinoless Double-Beta Decay with the Upgraded EXO-200 Detector. *Physical Review Letters*. 2018, vol. 120, p. 072701. Available from DOI: [10.1103/PhysRevLett.120.072701](https://doi.org/10.1103/PhysRevLett.120.072701).
29. P., Andrea; COLLABORATION, on behalf of the nEXO. The nEXO detector: design overview. *Journal of Physics: Conference Series*. 2020, vol. 1468, no. 1, p. 012131. Available from DOI: [10.1088/1742-6596/1468/1/012131](https://doi.org/10.1088/1742-6596/1468/1/012131).
30. ARNOLD, R. et al. Technical design and performance of the NEMO 3 detector. *Nuclear Instruments and Methods in Physics Research Section A: Accelerators, Spectrometers, Detectors and Associated Equipment*. 2005, vol. 536, no. 1, pp. 79–122. ISSN 0168-9002. Available from DOI: <https://doi.org/10.1016/j.nima.2004.07.194>.
31. ARNOLD, R. et al. Probing new physics models of neutrinoless double beta decay with SuperNEMO. *The European Physical Journal C*. 2010, vol. 70, no. 4, pp. 927–943. ISSN 1434-6052. Available from DOI: [10.1140/epjc/s10052-010-1481-5](https://doi.org/10.1140/epjc/s10052-010-1481-5).
32. BARABASH, A.S. et al. Calorimeter development for the SuperNEMO double beta decay experiment. *Nuclear Instruments and Methods in Physics Research Section A: Accelerators, Spectrometers, Detectors and Associated Equipment*. 2017, vol. 868, pp. 98–108. ISSN 0168-9002. Available from DOI: <https://doi.org/10.1016/j.nima.2017.06.044>.
33. MACKO, M. *SuperNEMO Experiment : Study of Systematic Uncertainties of Track Reconstruction and Energy Calibration. Evaluation of Sensitivity to 0nbb with Emission of Majoron for Se-82*. 2018. Available also from: <https://tel.archives-ouvertes.fr/tel-02122290>. Theses. Université de Bordeaux ; Univerzita Komenského (Bratislava). Faculté de mathématiques, physique et informatique.
34. ARNOLD, R. et al. Measurement of the distribution of ^{207}Bi depositions on calibration sources for SuperNEMO. *Journal of Instrumentation*. 2021, vol. 16, no. 07, T07012. Available from DOI: [10.1088/1748-0221/16/07/t07012](https://doi.org/10.1088/1748-0221/16/07/t07012).
35. QUINN, W. *The sensitivity of the NEMO technique to neutrinoless double beta decay and the commissioning of the SuperNEMO demonstrator module*. 2023. PhD thesis. University Coll. London, University Coll. London.
36. HODÁK, R. et al. Improvement of the energy resolution of the scintillating detectors for the low background measurement. *AIP Conference Proceedings*. 2015, vol. 1672, no. 1, p. 130003. Available from DOI: [10.1063/1.4928013](https://doi.org/10.1063/1.4928013).
37. AGUERRE, X. *Recherche de la décroissance double bêta sans émission de neutrino du ^{82}Se avec l'expérience SuperNEMO : reconstruction de l'énergie mesurée avec le calorimètre et analyse des premières données du démonstrateur*. 2023. Available also from: <https://theses.hal.science/tel-04428968>. Theses. Université de Bordeaux.
38. PALUŠOVÁ, V. *Monte Carlo simulations of detectors background and analysis of background characteristics of the SuperNEMO experiment in the Modane underground laboratory*. 2021. PhD thesis. Bordeaux U., Comenius U.

39. PALUŠOVÁ, V. et al. Natural radionuclides as background sources in the Modane underground laboratory. *Journal of Environmental Radioactivity*. 2020, vol. 216, p. 106185. ISSN 0265-931X. Available from DOI: <https://doi.org/10.1016/j.jenvrad.2020.106185>.
40. COLLABORATION, SuperNEMO. *Falaise documentation* [online] [visited on 2022-04-21]. Available from: <https://supernemo.org/Falaise/index.html>.
41. CERN. *GEANT4: A simulation toolkit* [online] [visited on 2022-05-01]. Available from: <https://geant4.web.cern.ch/>.
42. KŘIŽÁK, T. *Development of an algorithm for linear particle track reconstruction in SuperNEMO detector*. 2023. Available also from: <http://hdl.handle.net/10467/111453>. Theses. FNSPE CTU in Prague.
43. OLEKSANDROVYCH YANKOVSKYI, V. *Refinement of the SuperNEMO demonstrator geometry based on ^{207}Bi decay measurements*. 2023. Theses. Taras Shevchenko National University of Kyiv, Faculty of Physics.
44. PIN, A. *Recherche de la nature du neutrino via la décroissance double bêta sans émission de neutrinos : Caractérisation et optimisation du calorimètre SuperNEMO et impact sur la recherche de la décroissance du ^{82}Se : Développement du premier prototype LiquidO*. 2020. Available also from: <https://theses.hal.science/tel-03149593>. Theses. Université de Bordeaux.
45. HUBER, A. *Recherche de la nature du neutrino avec le détecteur SuperNEMO : simulations optiques pour l'optimisation du calorimètre et performances attendues pour le ^{82}Se* . 2017. Available also from: <http://www.theses.fr/2017BORD0682/document>. PhD thesis. 2017BORD0682.
46. BIRKS, J B. Scintillations from Organic Crystals: Specific Fluorescence and Relative Response to Different Radiations. *Proceedings of the Physical Society. Section A*. 1951, vol. 64, no. 10, p. 874. Available from DOI: 10.1088/0370-1298/64/10/303.
47. PRESS, William H. et al. *Numerical Recipes 3rd Edition: The Art of Scientific Computing*. 3rd ed. Cambridge University Press, 2007. ISBN 0521880688. Available also from: http://www.amazon.com/Numerical-Recipes-3rd-Scientific-Computing/dp/0521880688/ref=sr_1_1?ie=UTF8&s=books&qid=1280322496&sr=8-1.
48. KOŇAŘÍK, F. *Vývoj softwaru pro energetickou kalibraci pro SuperNEMO detektor*. 2022. Available also from: <http://hdl.handle.net/10467/104011>. Theses. FNSPE CTU in Prague.
49. BETHE, H.; ASHKIN, J. Passage of Radiations through Matter. *Experimental Nuclear Physics*. 1953, p. 253. Available also from: <https://hdl.handle.net/2027/mdp.39015003445122>.
50. BERGER, M.J. et al. *ESTAR, PSTAR, and ASTAR: Computer Programs for Calculating Stopping-Power and Range Tables for Electrons, Protons, and Helium Ions (version 2.0.1)*. Gaithersburg, MD, 2017. Tech. rep. National Institute of Standards and Technology. Available from DOI: <https://dx.doi.org/10.18434/T4NC7P>.

51. WIKIPEDIA CONTRIBUTORS. *Nelder–Mead method* — *Wikipedia, The Free Encyclopedia*. 2024. Available also from: https://en.wikipedia.org/w/index.php?title=Nelder%E2%80%93Mead_method&oldid=1219187831. [Online; accessed 7-May-2024].
52. KONARIK, F. *CalibrationScript* [online] [visited on 2024-05-09]. Available from: <https://github.com/konarfil/CalibrationScript.git>.